Julius-Maximilians-
UNIVERSITÄT
WÜRZBURG

UNIVERSITÄT WÜRZBURG
PHYSIKALISCHES INSTITUT
epVI

Investigation of defect states in organic semiconductors: Towards long term stable materials for organic photovoltaics

Dissertation zur Erlangung des
naturwissenschaftlichen Doktorgrades
der Julius-Maximilians-Universität Würzburg

vorgelegt von

Julia Schafferhans

aus Tirschenreuth

Würzburg 2011

Eingereicht am 31.03.2011
bei der Fakultät für Physik und Astronomie

1. Gutachter: Prof. Dr. Vladimir Dyakonov
2. Gutachter: Prof. Dr. Jean Geurts
3. Gutachter:
der Dissertation.

1. Prüfer: Prof. Dr. Vladimir Dyakonov
2. Prüfer: Prof. Dr. Jean Geurts
3. Prüfer: Prof. Dr. Wolfgang Kinzel
im Promotionskolloquium.

Tag des Promotionskolloquiums: 22.06.2011

Doktorurkunde ausgehändigt am:

Contents

1. Introduction

In the age of the climate change the search for new and the further development of existing technologies for the use of renewable energies are indispensable.

Thereby, beside biomass, wind and water, photovoltaics play an important role. Up to now, the standard technology in photovoltaics are silicon based solar cells, achieving efficiencies of up to 20 % for multicrystalline and even up to 25 % for monocrystalline silicon [41]. However, the silicon based technology yields high production costs and thus it is not economically competitive with e.g. fossil fuels, so far. Despite this, the amount of installed photovoltaics increased strongly the last years. For example, the installed photovoltaic capacity in Germany at the end of 2010 was $\sim$17,000 MWp which corresponds to about 12,000 GWh power generation, i.e. 2 % of Germanys gross consumption of electricity. Thereof, 7,000 MWp were newly installed alone in 2010 [18]. Yet, the positive trend might be further enhanced by cheaper and thus more cost-efficient technologies.

A promising complement and alternative to silicon solar cells are those based on organic semiconductors. One of the advantages of organic semiconductors is their high absorption yield and therefore the need of only a small material quantity, since layer thicknesses in the order of 100 nm are sufficient. The thin layers in combination with the processibility without the need of high temperature steps allow for the fabrication on flexible substrates, such as foil. This enables roll-to-roll production, yielding a high throughput and low processing costs [16].

Within the organic solar cells it can be distinguished between solar cells deposited from the gas phase (based on small molecules) and solution processed solar cells, mainly polymer/fullerene based. The latter were investigated in this thesis. In general organic solar cells consist of an electron donating and an electron accepting organic semiconductor. The two materials are either arranged coplanar on top of each other, a so called bilayer solar cell, or mixed within one layer, called bulk heterojunction solar cell. For solution processed solar cells, the latter is the favorite and more effective device geometry.

The great benefit of these solution processed organic solar cells is that they can be produced by standard printing or coating techniques, further reducing the costs and enhancing the throughput. For example, standard printing machines like a sheet-fed offset printing press or a web offset printing press, typically print 1-3 m/s and 15 m/s, respectively [16]. For comparison, a typical silicon wafer production plant has a maximum area output of about 88,000 m^2 per year [16]. In contrast, to produce the same area with printing techniques takes only a few hours. It is supposed, that in the future costs of less than 1 USD/Wp can be achieved with printed organic solar cells [16].

Beside costs, efficiency and lifetime of the solar cells are the key issues towards commercialization. However, the particular requirements depend on the applications. For consumer electronics efficiencies of 3-5 % and lifetimes of 3-5 years are assumed to be sufficient [15]. Indeed, the first products can already be purchased [52, 53]. In contrast, for wide-spread applications efficiencies of 10 % are regarded as the milestone towards commercialization and

lifetimes of about 10 years are desired [15].

The main focus in the research on organic solar cells in the last years was in enhancing the efficiency. Recently, efficiencies of 8.3 % have been achieved under laboratory conditions [41] and it is assumed that 10 % will be attained in the near future [15]. Thus, the remaining critical issue is the lifetime of these devices.

Although, the lifetime of organic solar cells recently became more and more in focus in scientific research, the different degradation pathways are still not completely understood. However, a detailed understanding of the degradation mechanism in these devices is the prerequisite for lifetime enhancement.

With respect to the operation stability of organic solar cells the presence of trap states in these devices might also be decisive, as they affect the charge carrier mobility, the internal field distribution as well as the recombination dynamics of charge carriers and thus influence the solar cell performance.

In this work, the trap states in commonly used organic semiconductors for organic solar cells, namely poly(3-hexylthiophene) and methanofullerenes are investigated. With respect to the stability of organic bulk heterojunction solar cells, the influence of oxygen on the trap states in poly(3-hexylthiophene) as well as on the solar cell performance is addressed.

The thesis is organized as follows: First of all the working principle of organic bulk heterojunction solar cells, the materials investigated in this work and the charge transport in disordered organic semiconductors are introduced (Chapter 2). Chapter 3 focuses on trap states in organic semiconductors and the fundamentals of the experimental methods used to investigate the trap states: thermally stimulated current and deep level transient spectroscopy. In Chapter 4 the sample preparation and the experimental setups are described. Afterwards, the experimental results and their discussion are presented. Chapter 5 treats the trap distribution in poly(3-hexylthiophene) and the influence of oxygen on the trap states. In Chapter 6 the trap states in three methanofullerenes, commonly used as acceptor in organic solar cells, are investigated. Chapter 7 and Chapter 8 address blends of poly(3-hexylthiophene) and the fullerene derivative $PC_{61}BM$. The focus in Chapter 7 is on the trap distribution in the blends compared to the single materials and the influence of the morphology on the trap states. In Chapter 8 the influence of oxygen on the blends is investigated. In Chapter 9 and Chapter 10 (German), the main results of this thesis are summarized. A list of the used abbreviations and symbols can be found in A and B, respectively.

2. Bulk Heterojunction Solar Cells

2.1. Operating Principles

Bulk heterojunction (BHJ) solar cells are based on a simple geometry, where the blend of donor and acceptor material is sandwiched between two electrodes, with one electrode being transparent. A scheme of a BHJ solar cell is shown in Figure 2.1. To convert the incident light into photocurrent, five fundamental processes have to take place, i.e. (1) photon absorption accompanied with exciton generation, (2) exciton diffusion and dissociation, (3) charge carrier pair dissociation, (4) charge carrier transport, and at last charge carrier extraction (5). These five steps are shown in Figure 2.1 from a kinetic, as well as an energetic perspective and will now be described briefly. A more detailed discussion can for example be found in [27].

(1) Photon absorption and exciton generation

The first step is the absorption of the incident light within the active layer of the solar cell. This is usually mostly done by the donor material, a conjugated polymer (see Figure 2.1 (1)). Due to the high absorption coefficient ($> 10^7$ m^{-1}), layer thicknesses of only about 100–300 nm are sufficient for a good absorption yield. The disadvantage of commonly used conjugated polymers, however, is the narrow absorption band width covering only the visible optical spectrum of the sun light [50, 82, 87]. Approaches to overcome this limitation and thus enhancing light harvesting are for example applying low bandgap polymers as donors [13, 98, 113, 114] and the usage of acceptors with improved contribution to the absorption [147].

By absorbing the light, excitons are generated in the organic semiconductor. Since the dielectric constant in organic semiconductors is quite low (typically between 3 and 4) the exciton binding energy is quite high. Assuming a distance of the electron–hole pairs of 1 nm and a dielectric constant of 3, the coulomb binding energy yields 0.5 eV. This is significantly higher than the thermal energy at room temperature and thus it is not sufficient to efficiently separate the strongly bound Frenkel excitons [48]. If the excitons can not be separated within their lifetime (around 1 ns for singlet excitons in organic semiconductors), they recombine radiatively and thus get lost for the photocurrent generation. For an effective dissociation of the Frenkel excitons a second organic semiconductor is used as electron acceptor.

(2) Exciton diffusion and dissociation

The prerequisite of a good electron acceptor is a sufficiently higher electron affinity than that of the donating polymer. So far, the best working acceptors in BHJ solar cells are derivatives of the fullerenes C_{60} and C_{70}, e.g. [6,6]-phenyl C61 butyric acid methyl ester ($PC_{61}BM$). Although research was done to replace the fullerene derivatives as acceptors by polymers [44, 55, 91] or non–fullerene small molecules [151], so far these approaches exhibit less efficient photocurrent generation than the fullerene based solar cells.

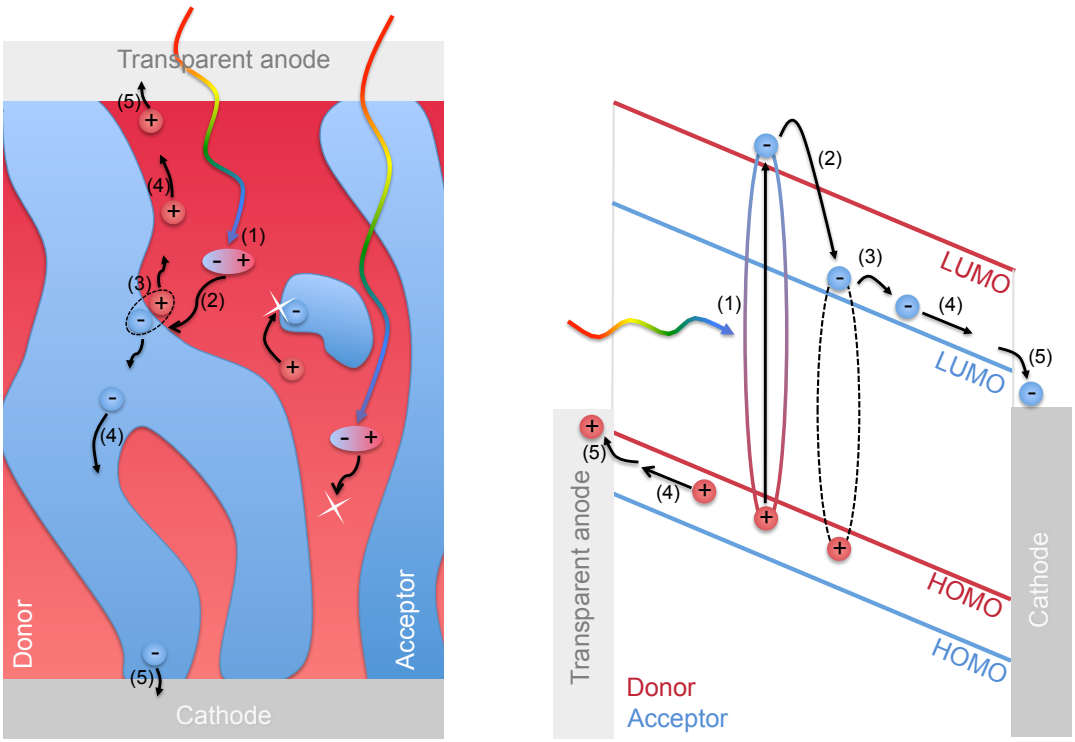

(a) (b)

Figure 2.1.: The fundamental steps towards photocurrent in an organic BHJ solar cell: from a kinetic point of view (a) and the corresponding simplified energy diagram (binding energies for excitons and polaron pairs are not shown) (b). (1) Photon absorption in the polymer and exciton generation, (2) exciton diffusion to the acceptor interface and exciton dissociation by electron transfer from the donor to the acceptor, (3) polaron pair dissociation, (4) charge transport of the holes in the donor and the electrons in the acceptor phase via hopping between localized states, (5) extraction of the charges at the respective electrodes. After [27].

Before the electron transfer from the donor to the acceptor can take place, the exciton has to diffuse to the donor–acceptor interface within its lifetime [10, 23] (Figure 2.1 (2)). The exciton diffusion length in conjugated polymers is in the order of 10 nm. For example for poly(3-hexylthiophene) (P3HT), an exciton diffusion length of about 8 nm is reported [126], whereas for poly(p-phenylenevinylene) (PPV) a value of 12 nm can be found in literature [133]. This is the reason, why the concept of BHJ solar cells is favorable, due to the intermixing of donor and acceptor within the whole active layer, resulting in a lot of interfaces.

Once the exciton reaches the interface, the electron can be transferred to the acceptor, as shown in Figure 2.1. Therefore, the energy gain of the charge transfer has to be larger than the exciton binding energy. For a rough estimation of the energy gain the difference in energy of the lowest unoccupied molecular orbital (LUMO) of the donor and the LUMO of the acceptor can be used. But this has to be treated with care, since the LUMO only describes an uncharged orbital and neither a charged one nor an optical transition [28]. If the charge transfer takes place, the transfer itself is very fast and happens on a timescale in the order of

tens of femtoseconds [14, 56, 121]. As a result, there is a hole remaining on the donor and an electron on the acceptor. This charge carrier pair (also called charge transfer state (CTS) or polaron pair) [110, 140] is still Coulomb bound [21]—but less than an exciton—and has to be dissociated further.

(3) Charge carrier pair dissociation

The polaron pair dissociation is shown in Figure 2.1 (3). The most commonly used model to describe polaron pair dissociation is the Braun–Onsager model [17]. This model is an extension of the one introduced by Onsager [111] to calculate the separation probability of Coulomb-bound ion pairs of opposite charges yielding an initial distance. Thereby, the separation is assisted by an electric field. The extension of Braun accounts for the finite lifetime of the initial bound state and applying it to the dissociation of CTSs in donor-acceptor systems. In this model three transition rates are used: the recombination rate of polaron pairs to the ground state k_f, given by the inverse lifetime of the polaron pairs τ_{pp}, the dissociation rate of the polaron pairs to free charges k_d and the recombination rate of free charges to polaron pairs k_r. In this description, free charges can never recombine directly to the ground state, but first have to form a polaron pair. The field dependent polaron pair dissociation probability $P(F)$ after Onsager–Braun is [111]:

$$P(F) = \frac{k_d(F)}{k_d(F) + k_f} \quad . \tag{2.1}$$

Beside the electric field F, the dissociation rate k_d depends on the sum of electron and hole mobility, the initial polaron pair radius, its Coulomb binding energy and the thermal energy. Further details are given in [17, 27].

Although the Onsager–Braun model is often used to describe polaron pair dissociation in organic solar cells [19, 30, 71, 93], it is a simplified one and therefore does not account for all phenomena in these devices, for example the energetic disorder or high local charge carrier mobilities e.g. due to delocalization of the holes along polymer chains. These influences on the polaron pair dissociation yield were recently considered in Monte Carlo simulations [29], showing an increasing dissociation yield with increasing conjugation length of the polymers for electric fields in the range where organic solar cells are operated. A higher local mobility can be also due to nanocrystalline regions in the donor or acceptor phase. Thus, larger phases of the donor and acceptor material positively influence the polaron pair dissociation which is in contrast to the "as mixed as possible" approach if one only considers the exciton dissociation.

Another interesting topic, addressed in literature, is wether or not excess energy after the exciton dissociation enhances the polaron pair dissociation yield. Ohkita et al. [110] investigated these influences by transient absorption measurements of different polythiophenes blended with $PC_{61}BM$. The result was an exponential dependence of the polaron density—thus dissociated polaron pairs—on the difference between the singlet exciton energy and the energy of the resulting polaron pair.

Polaron pairs, which are not dissociated can recombine geminately and thus are lost for photocurrent. Another possible loss mechanism is an electron back transfer from the acceptor to a triplet exciton in the donor, if this is an energetically favorable state for the electron [140]. Furthermore, a charge carrier can be extracted at the wrong electrode as the polaron pair moves along together. But so far, this process has only been predicted theoretically by Monte Carlo

simulations [132].

(4) Charge carrier transport

After the polaron pair was successfully dissociated, the charge carriers have to be transported to the respective electrodes (Figure 2.1 (4)). The charge transport in disordered organic semiconductors occurs via hopping from localized state to localized state. A more detailed theoretical description is given in Section 2.4. Thereby, in organic solar cells the hole is usually transported in the donor material and the electron in the acceptor. For an effective transport of the charge carriers to the electrodes, percolation paths are necessary. Isolated islands of either the donor or acceptor phase (as shown in Figure 2.1) will hinder the respective charges to arrive at the electrode. Instead, a charge carrier located on the isolated island will most likely recombine with a charge carrier of opposite sign coming past along his way to the electrode, and therefore both of them get lost. The perfect morphology in BHJ solar cells is therefore a trade of between strongly intermixed donor–acceptor phases for efficient exciton dissociation and extended phases for a high polaron pair dissociation yield and good transport of the charge carriers. In the case of P3HT based BHJ solar cells, applying an annealing step to the samples results in a higher crystallinity of P3HT and larger phases of donor and acceptor, thus improving the solar cell performance [32, 112, 122, 139]. Another method for improving the morphology with respect to the solar cell efficiency, which works for a couple of donor polymers, is the usage of additives, such as octanedithiol, within the solution [75, 114].

The parameter describing the transport characteristics of a material is the charge carrier mobility μ, which is the proportionality constant between the drift velocity v_d and the electric field F:

$$\mu = \frac{v_d}{F} \quad . \tag{2.2}$$

In organic solar cells, a balanced mobility of electrons and holes is desirable, to avoid space charges to form up [95], which makes accordant demands on the acceptor and donor materials. Indeed, in good organic BHJ solar cells, as for example blends of P3HT and $PC_{61}BM$, the charge carrier mobilities for electrons and holes are (almost) balanced [80]. As already mentioned above, the polaron pair dissociation yield increases with increasing mobility. Therefore, one could assume, that the higher the mobility the better the solar cell performance. However, recently it was shown by macroscopic simulations, that for mobilities of 10^{-8} m^2/Vs, which corresponds to the mobilities of good P3HT:$PC_{61}BM$ solar cells, the polaron pair dissociation is already quite efficient [30]. Too low mobilities, however, lead to a charge build up due to the inefficient current extraction, limiting the solar cell performance.

It should be noted that the mobility is strongly affected by trap states present in the organic semiconductors. Since trapped charge carriers first have to be released to further contribute to the current flow, the mobility is lowered in the presence of trap states influencing the performance of solar cells. Furthermore the existence of deep traps or a huge amount of traps in only one of both materials can lead to imbalanced mobilities in the solar cells. Details about trap states are given in Section 3.1.

The loss mechanism during this stage of photocurrent generation is the recombination of charge carriers. In contrast to the geminate recombination during polaron pair dissociation, this recombination is called nongeminate, since the contributing electrons and holes do not have a common precursor state. Thereby, the recombination of a mobile charge carrier (e.g. an

electron) with a trapped counterpart is considered to be a first order process, if the density of trapped charges clearly exceeds the number of mobile ones. The recombination thus depends on the density of mobile charges (mobile electron density n in the sample) and their lifetime τ and the recombination rate R is proportional to $\propto n/\tau$. In contrast, if two mobile and independent charges are involved in the recombination process, the recombination is described by a bimolecular recombination rate. The recombination rate thus depends on the product of the densities of mobile electrons n and holes p (second order process) and is usually given by Langevin's theory [73, 115]:

$$R = \gamma_L(np - n_i^2) \quad , \tag{2.3}$$

with the intrinsic carrier concentration n_i and the Langevin recombination prefactor γ_L. It is assumed, that the rate limiting step for this recombination is to find a recombination partner and thus the prefactor depends on the sum of electron and hole mobilities (μ_e and μ_h):

$$\gamma_L = \frac{q}{\varepsilon_r \varepsilon_0}(\mu_e + \mu_h) \quad , \tag{2.4}$$

with the elementary charge q and the effective dielectric constant of the ambipolar semiconductor $\varepsilon_r\varepsilon_0$. However, in organic BHJ solar cells a recombination order higher than two for mobile charges has been reported several times [30, 60, 129], with an increasing recombination order with decreasing temperature [36] and depending on the processing conditions [129].

A similar behavior was reported for dye solar cells, where a recombination order of 1.4 instead of the expected monomolecular recombination was observed [150]. This variation was attributed to a delayed recombination due to trapping of charges within an exponential trap distribution. The delayed recombination due to traps also yields a consistent explanation for the observed recombination behavior in organic BHJ solar cells [22, 33, 36].

(5) Charge carrier extraction

The last step in a working solar cell is the successful extraction of the charges at their respective electrodes. Therefore, holes have to be extracted at the anode, electrons at the cathode. Charge carriers leaving the device at the wrong electrode are lost for photocurrent. To overcome this problem, hole transport layers (HTL) and electron transport layers (ETL) are often used as interlayers between the active material and the electrodes [43, 74, 134, 144]. The charge extraction process itself strongly depends on device architecture, determining the steady–state charge carrier density. If the extraction rate of the charges from the device is too low, the charges will pill up and form a space charge region at the respective electrode, leading to a so-called s-shaped current–voltage characteristic, which limits the efficiency of solar cells [143]. These s-shaped current–voltage characteristics can be modeled by a reduced surface recombination [99, 143].

2.2. Solar Cell Parameters

The task of a solar cell is to convert the radiant power of the incident light (P_L) into electrical power. The efficiency η of this process is given by:

$$\eta = \frac{P_{mpp}}{P_L} \quad , \tag{2.5}$$

with the maximum power P_{mpp} achieved by the solar cell. This can be calculated by the characteristic parameters of the solar cells, namely short-circuit current (J_{sc}), open-circuit voltage (V_{oc}) and fill factor (FF), which can be obtained by measuring the current–voltage (IV) characteristics of the solar cells under illumination. An exemplary IV-characteristic of an organic BHJ solar cell is shown in Figure 2.2, with the solar cell parameters highlighted. The fill factor is

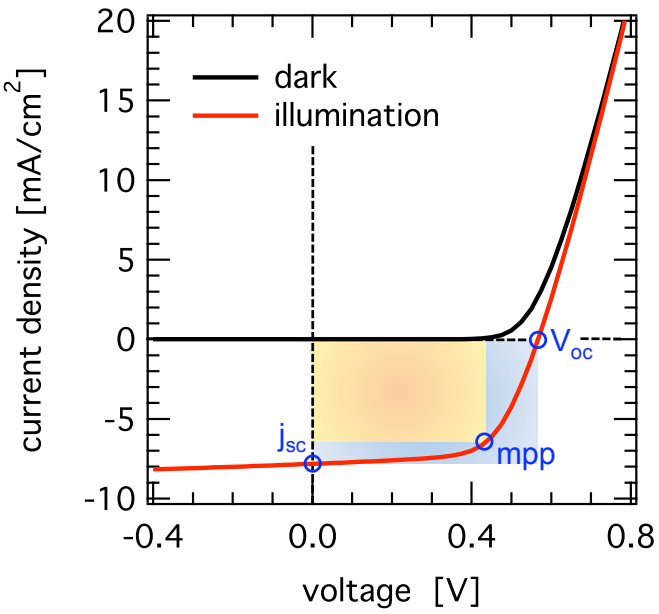

Figure 2.2.: Current–voltage characteristics of an organic bulk heterojunction solar cell with the solar cell parameters short-circuit current density j_{sc} and open-circuit voltage V_{oc}. The point of maximum power (mpp) is also shown. The fill factor is given by the ratio of maximum power (orange rectangle) and the product of j_{sc} and V_{oc} (blue rectangle).

defined by the ratio of maximum power and the product of open-circuit voltage and short-circuit current. Thus, Equation 2.5 can be written as:

$$\eta = \frac{V_{oc} J_{sc} FF}{P_L} \quad . \tag{2.6}$$

Typically for the estimation of the efficiency the short-circuit current density j_{sc} and the radiant power density Φ_L is used, yielding following equation for the efficiency:

$$\eta = \frac{V_{oc} j_{sc} FF}{\Phi_L} \quad . \tag{2.7}$$

For a comparable efficiency determination a standard for the test conditions is necessary. This standard is given by a radiant power density of 100 mW/cm^2 of an AM1.5G sun spectrum and a measurement temperature of 25 °C. Details about how to measure accurately the IV–characteristics of organic solar cells can be found in [127].

2.3. Materials

The main constituent of an organic semiconductor is carbon, with alternating single and double bonds between the carbon atoms, which is called conjugation. Carbon exhibits four valence electrons, the electron configuration in the ground state is $1s^2 2s^2 2p^2$. In organic semiconductors the one $2s$ and two of the three $2p$ orbitals ($p_x p_y$) are hybridized to three sp^2 orbitals. These are arranged coplanar at an angle of 120 ° to each other forming σ-bonds, resulting in a strongly localized electron density in the plane of the molecule. The last remaining valence electron of the carbon atom resides in the p_z orbital, perpendicular to the plane of the molecule. The p_z orbitals of neighboring carbon atoms overlap, forming π-bonds, and cause a delocalized electron density above and below the plane of the molecule. These overlapping π-electron wave functions along the conjugation path of the molecule are the origin of the conductivity in these material systems.

The p_z orbitals are split into bonding π-orbitals and antibonding π*-orbitals separated by an energy gap. The bonding orbitals are called the highest occupied molecular orbital (HOMO) and the antibonding orbitals are called the lowest unoccupied molecular orbital (LUMO) and represent the analogy of the valence and conduction band of inorganic semiconductors. The energy gap between the HOMO and LUMO is in the range of 1 eV to 3 eV and is responsible for the semiconducting properties.

Organic semiconductors can be divided into two classes: small molecules (e.g. anthracene) and conjugated polymers (e.g. poly(3-hexylthiophene)). The former are mostly processed by evaporation forming well ordered films, whereas the latter can be processed from solution, but may result in less ordered films.

As already mentioned before, for the BHJ solar cells investigated in this thesis, conjugated polymers are used as donors, whereas fullerene derivatives are used as acceptors. Both material systems, in particular the investigated materials, will be addressed in the following in more detail.

2.3.1. Conjugated Polymers

Polymers consist of long chains of repeating molecule units, so called monomers. The simplest conjugated polymer is polyacetylene which consists of carbon atoms with alternating single and double bonds between them and each carbon atom is bonded with one hydrogen atom (Figure 2.3).

The delocalized π-electron system along a polymer chain is given by the conjugation length. Perfectly conjugated segments are interrupted by chemical defects, e.g. sp^3 hybridized carbon atoms, or by structural defects such as twisted or kinked polymer chains. These defects limit the conjugation length and therefore the delocalization typically to a length scale of about 20 monomer units. For example for poly(p-phenylenevinylene) this corresponds to a length of about 9–12 nm [115]. The polymer chains among each other are only weakly bound by van

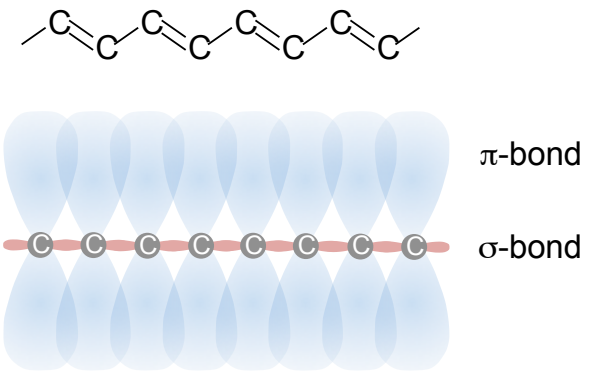

Figure 2.3.: Molecular structure of polyacetylene with the alternating single and double bonds (top). The overlapping p_z orbitals form π-bonds resulting in a delocalized electron density along the polymer chain (bottom).

der Waals forces. Hence, the charge carriers are localized within segments of the polymer chains. Furthermore, the distribution in the conjugation length results in an energetic disorder. Therefore, the HOMO and LUMO levels yield a distribution in energy. Electrostatic interactions and polarization effects with neighboring molecules or polymer segments can further enhance the energetic disorder.

The conjugated polymer investigated in this work is poly(3-hexylthiophene) (P3HT). The monomer unit of P3HT (shown in Figure 2.4) is a thiophene ring with a hexyl side chain attached on the third position. P3HT can be classified by its regioregularity. Thereby, the classification is done by the linkage of the monomer units. P3HT is called regioregular when it features a periodic head–to–tail configuration—the side of the thiophene ring with the attached sidechain is called head and tail the opposite one. Regiorandom P3HT, however, yields a random configuration.

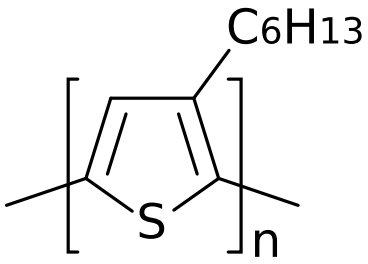

Figure 2.4.: Monomer unit of P3HT.

The regioregularity strongly influences the orientation of the polymer chains to one another. Via X-ray diffraction studies [116] it was shown that regioregular P3HT polymer chains exhibit an ordered orientation in the (100)-axis as well as in the (010)-axis ($\pi-\pi$–interchain stacking) (see Figure 2.4). Thereby, the distance along the (100)-axis is about 1.68 nm and the distance of the $\pi-\pi$–stacking 0.38 nm [116]. The charge transport can take place along the (100)-axis as well as the direction of the $\pi-\pi$–stacking, with the latter being the more efficient one [131]. Due to this highly ordered structure, regioregular P3HT features a high crystallinity.

However, regiorandom P3HT is significantly less ordered because of the random head–to–tail configuration and thus also yields lower mobilities.

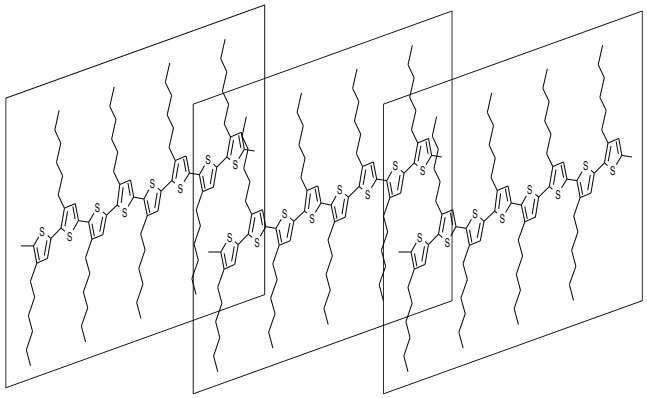

Figure 2.5.: $\pi - \pi$–interchain stacking of P3HT.

P3HT investigated in this work was purchased from Rieke Metals, Inc. Two different batches were used: 4002E (regioregularity 90-94 %) and Sepiolid P200 (regioregularity $\approx$ 98 %).

2.3.2. Fullerene Derivatives

As already mentioned in Section 2.1, so far fullerene based materials are the best working acceptors in organic solar cells. Due to the poor solubility of the fullerene itself, for solution processed BHJ solar cells fullerene derivatives with an attached butyric acid methyl ester side chain (to enhance the solubility) are used. The reason of their success is based on several beneficial properties: fullerenes have a high electron affinity with respect to most conjugated polymers used as donors and exhibit an ultrafast forward photoinduced electron transfer from these [14, 56, 121]. Furthermore, the fullerene derivatives are isotropic (C_{60} derivatives) or relatively isotropic (C_{70} derivatives) which has a positive implication on the charge transfer and charge carrier mobility [14]. For example, electron mobilities in $PC_{61}BM$ based diodes of 2×10^{-3} cm^2/Vs are reported [94]. Besides the mentioned advantages of fullerenes and their derivatives, there are some drawbacks for the use as acceptors in organic solar cells. One of these is the relatively low optical absorption in the solar spectral range, especially of C_{60} and $PC_{61}BM$ [14]. Also the electron affinity is too high in combination with most donors, resulting in a loss of V_{oc}. A further disadvantage arises with the use of multiple adduct fullerene derivatives such as bis$PC_{61}BM$ or fullerene derivatives higher than C_{60}, for example $PC_{71}BM$. These derivatives are formed as isomeric mixtures resulting in a variety of HOMO and LUMO energies introducing a higher energetic disorder compared to fullerene derivatives consisting of only one isomer [14, 38].

In this work, three different fullerene derivatives are investigated, namely $PC_{61}BM$ ([6,6]-phenyl C61 butyric acid methyl ester), bis$PC_{61}BM$ (bis[6,6]-phenyl C61 butyric acid methyl ester) and $PC_{71}BM$ ([6,6]-phenyl C71 butyric acid methyl ester). The chemical structures are shown in Figure 2.6. The materials were purchased from Solenne.

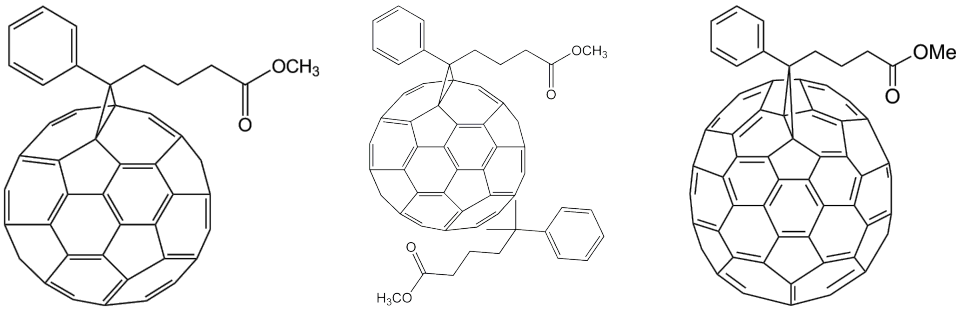

(a) $PC_{61}BM$ (b) bis$PC_{61}BM$ (c) $PC_{71}BM$

Figure 2.6.: Chemical structure of the investigated fullerene derivatives. From [54].

2.4. Charge Transport

Due to the missing long range order in disordered organic semiconductors, they do not exhibit extended bands, like crystalline inorganic semiconductors. Instead the charge carriers are localized on single molecules, polymer segments or crystalline phases within the organic semiconductor, as already mentioned in Section 2.3. The charge transport among this localized states is described by a hopping process. Already in 1960 Miller and Abrahams introduced a model for this hopping transport [96]. Their investigations were focused on slightly doped inorganic semiconductors at low temperatures, with energetically shallow impurity centers, acting as localized states. This as variable range hopping (VRH) known model was later adopted for disordered organic semiconductors. Thereby, the hopping transport is a thermally activated (i.e. phonon assisted) tunneling between the localized states. To get from one localized state to another the charge carrier has to overcome the spatial distance as well as the energetic difference between initial and target state. The former is overcome via tunneling and the latter has to be compensated by the absorption or emission of a phonon (conservation of energy). The hopping rate ν_{ij} between an initially occupied localized state i (energy E_i) and an unoccupied localized target state j (energy E_j) is given by the approximated Miller–Abrahams equation:

$$\nu_{ij} = \nu_0 \exp(-2\gamma R_{ij}) \begin{cases} \exp\left(-\dfrac{E_j - E_i}{k_B T}\right) & E_j > E_i \quad \text{(uphop)} \\ 1 & E_j \leq E_i \quad \text{(downhop)} \ . \end{cases} \tag{2.8}$$

ν_0 is the maximum hopping rate, called the attempt-to-escape frequency, the rate with which a charge carrier tries to escape from his localized state and in organic semiconductors it is assumed to be in the range of 10^{11}–10^{13} s^{-1}. γ is the inverse localization radius, a quantity for the wavefunction overlap and R_{ij} is the spatial distance between initial and target state. The first term in Equation 2.8 corresponds to the tunneling, the second to the thermal activation. For uphops the Boltzmann term is used (a phonon from the thermal bath is provided) (k_B is the

Boltzmann constant and T the temperature), whereas for downhops it is approximately assumed that the emission of a corresponding phonon is always possible (probability=1). Thus, an uphop is always harder than a downhop.

In 1993 Bässler [11] extended the VRH model by using a Gaussian distribution of localized states $g(E)$, which is called Gaussian disorder model (GDM):

$$g(E) = \frac{N}{\sigma\sqrt{2\pi}} \exp\left(-\frac{E^2}{2\sigma^2}\right) \quad , \tag{2.9}$$

with N the density of localized states and the energy E measured relative to the center of the density of states (DOS) distribution. σ is the width of the distribution, a quantity of the disorder in the organic semiconductor – the less ordered, the higher is σ. For organic semiconductors σ is in the range of 50–100 meV in most cases [24]. The assumption of a Gaussian distributed density of states is founded in the fluctuation of the lattice polarization energies and the distribution in conjugation length in conjugated polymers [11] and supported by absorption spectra of organic semiconductors often yielding a Gaussian profile. A scheme of the hopping transport within a Gaussian distribution of localized states is shown in Figure 2.7.

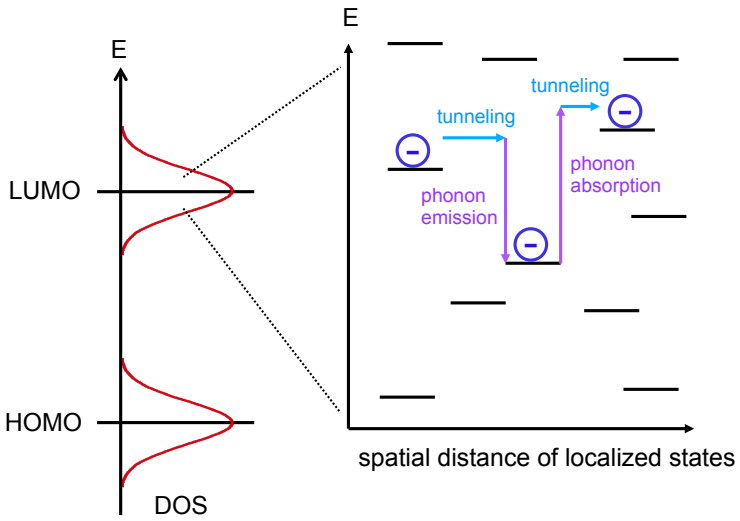

Figure 2.7.: Hopping transport in a Gaussian density of localized states. The spatial distance is overcome by tunneling, the energetic difference of initial and target state is compensated by emission or absorption of a phonon.

Bässler used the hopping–rate equation (Equation 2.8) to perform Monte Carlo simulations and investigated thus the charge transport in organic semiconductors. The received mobility values from the simulations were fitted parametrically resulting in following expression for the temperature and electric field (F) dependence of the mobility [11]:

$$\mu_{GDM}(E) = \mu_\infty \exp\left[-\left(\frac{2\sigma}{3k_BT}\right)^2\right] \begin{cases} \exp\left\{C\left[\left(\frac{\sigma}{k_BT}\right)^2 - \Sigma^2\right]\sqrt{F}\right\}, & \Sigma \geq 1.5 \\ \exp\left\{C\left[\left(\frac{\sigma}{k_BT}\right)^2 - 2.25\right]\sqrt{F}\right\}, & \Sigma < 1.5 \quad . \end{cases} \tag{2.10}$$

Σ, corresponding to the spatial disorder, C and 2/3 are scaling factors from the parametric fit. The resulting dependencies of the mobility of $\ln\mu \propto \sqrt{F}$ and $\ln\mu \propto T^{-2}$ are in good agreement with recent findings [97, 138]. A few years later, another model, called correlated disorder model (CDM), was proposed by Novikov et al. [109]. In the CDM the spatial and energetic disorder depend on each other, accounting for the fact that a changing environment for a given molecule will also influence its energetic position.

Another important result of Bässlers Monte Carlo simulations is that the charge transport in organic semiconductors can be divided into two different regimes: thermalization and charge transport in quasi–equilibrium. Charge carriers which are injected from electrodes into the organic semiconductor or which are photogenerated first of all mainly perform a series of downhops until they reach quasi-equilibrium. This is called energy relaxation or thermalization. In quasi-equilibrium the density of occupied states (DOOS) for a given temperature is located about $\frac{\sigma^2}{k_B T}$ below the center of the Gaussian density of states [11]. In steady-state conditions, however, the charge carriers perform uphops as well as downhops. On average these hops are located around a certain energy (independent of the energy of the initial state), called transport energy E_{tr}. Later on, the relaxation (in the case of low temperatures) [4] as well as the transport energy [5, 35, 105] were also calculated analytically. Thereby, the expression for the transport energies differ a bit within the different approaches. The common ground, however, is that the transport energy yields a temperature dependence: the higher the temperature, the higher the transport energy. Arkhipovs energy of most probable jumps, which is often used as transport energy [7, 8, 65], for example, is given by the following transcendental equation [5]:

$$\int_{-\infty}^{E_{tr}} dE_j g(E_j)(E_{tr} - E_j)^3 = \frac{6}{\pi}(\gamma k_B T)^3 \quad , \tag{2.11}$$

with the inverse localization radius γ and the target states energy E_j. The thermalization as well as the steady–state hopping process for photogenerated electrons within a Gaussian distribution of localized states is shown schematically in Figure 2.8. With the aid of the transport energy the charge transport in organic semiconductors can be simplified described by the multiple trapping and release (MTR) model [46]. This model was originally introduced to describe the charge transport in amorphous inorganic semiconductors (e.g. amorphous silicon) [86, 106, 107]. Within the MTR a quasi band transport is assumed. Electrons which are located above the so-called mobility edge can move quasi-free within the semiconductor (in analogy to the conduction band). States below the mobility edge are treated as trap states for the electrons. Trapped charge carriers have a certain residence time in the traps and have to be thermally activated above the mobility edge to again participate in the charge transport. Thus, the charge transport can be interpreted by a multiple trapping and thermal release of charge carriers. Transport among the trap states is thereby forbidden [106]. Applying this model to organic semiconductors the transport energy is the analogy to the mobility edge, with electrons above the transport energy being mobile and those below the transport energy being trapped and immobile. The justification for using the MTR model is that the charge carriers located below the transport energy will also perform hops around this, but the hopping rate for upward hops is lower than for downward hops or those to target states with similar energy as the initial state (see Equation 2.8) and thus are the transport limiting ones. It has to be noted that this approach is only valid for the steady-state transport, not for the relaxation process. Furthermore, in contrast to the mobility edge, the transport energy in organic semiconductors is temperature dependent.

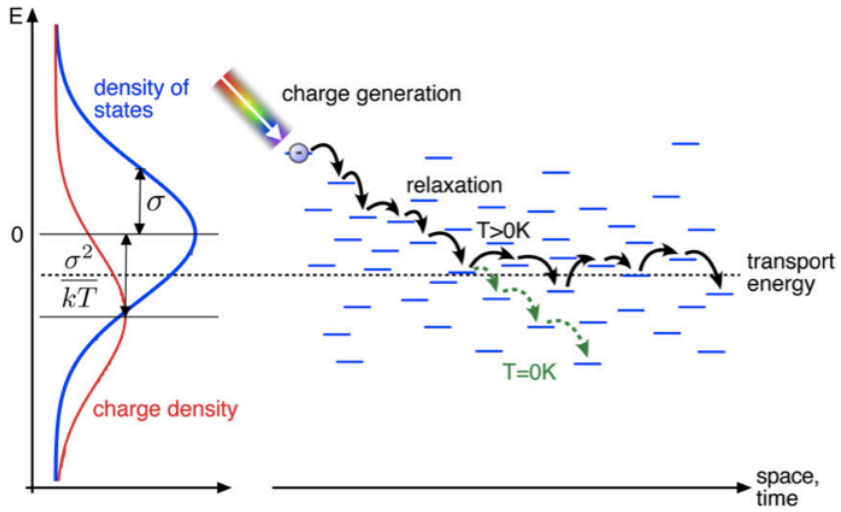

Figure 2.8.: The charge transport between localized states of a Gaussian energy distribution is given by two different mechanism: thermalization and charge transport in quasi–equilibrium. Photogenerated (or injected) charge carriers perform a number of downhops until they reach quasi–equilibrium. In quasi–equilibrium the density of occupied states distribution is approximately located at $\frac{\sigma^2}{k_B T}$ below the center of the density of states. In steady–state the charge transport takes place via hops around the transport energy. In the limit of $T = 0$ K, the charge carriers relax to the deepest states where they remain trapped. From [27].

3. Trap States and Trap Spectroscopy

Trap states can have a significant influence on the performance of organic solar cells, as they can act as recombination centers, lower the mobility, disturb the internal field distribution and reduce the energy conversion efficiency. Furthermore, trap states introduced by oxygen exposure can have a high impact on the long term stability of organic photovoltaic devices. Therefore, detailed information about the trap states in the active materials used for solar cells, their densities and energetic levels as well as their origins are an important prerequisite for enhancing power conversion efficiency and operating stability of organic photovoltaic devices.

First of all a definition of traps in organic semiconductors will be given as well as considerations concerning the origin of trap states (Section 3.1). Afterwards, the two spectroscopic methods used in this work will be introduced, namely thermally stimulated current (Section 3.2) and deep level transient spectroscopy (Section 3.3).

3.1. Trap States

With the aid of the transport energy, as introduced in Section 2.4, a definition of trap states in organic semiconductors can be given, despite the fact that all states are localized: states below the transport energy act as traps [124]. As already described before, the density of states in an organic semiconductor yields a Gaussian distribution, due to the fluctuations in conjugation length in the case of polymers and fluctuations of the lattice polarization energies. Thus the tail states of the intrinsic density of states are trap states. In addition to the trap states formed by the regular DOS distribution there can exist further traps, as shown in Figure 3.1. Origin for those additional traps can be impurities, if the energetic levels of the impurities are within the bandgap of the HOMO/LUMO levels of the organic semiconductor. Furthermore, structural defects, which occur with an enhanced probability might not only contribute to the broadening of the regular DOS, but also form deeper states within the bandgap [124]. Examples therefore are grain boundaries within polycrystalline layers or grains between amorphous and crystalline phases. In the case of BHJ solar cells, which consist of a blend of two materials, both materials will also influence each other in a close vicinity due to electronic polarization and interface dipoles. Furthermore, as mentioned above, the morphology is strongly affected. Both of these can again result in the formation of additional and deeper traps. As already noted in Section 2.3.2 multiple adduct fullerene derivatives such as bis$PC_{61}BM$ consist of different isomers, yielding a variation of the LUMO levels. Thereby, the lower ones can act as electron traps. Due to the potential fluctuations within the organic semiconductors, the additional trap states will also yield a certain distribution in energy, rather than monoenergetic trap levels.

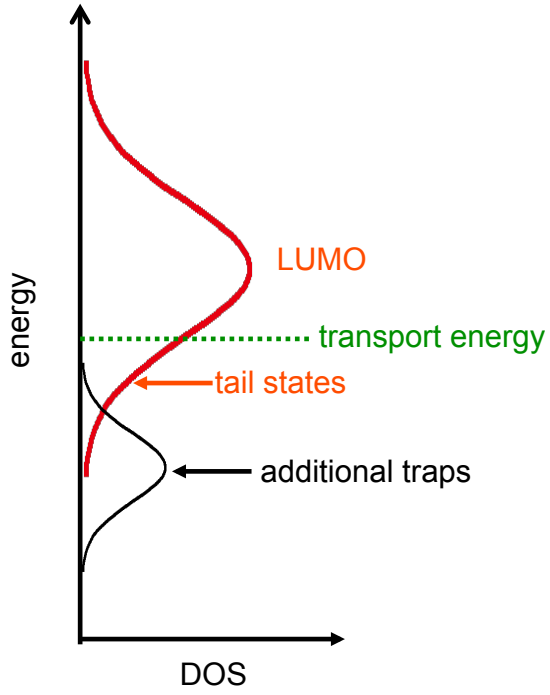

Figure 3.1.: LUMO level of an organic semiconductor with transport energy. Beside the tail states of the LUMO level, acting as electron traps, there can be additional trap states.

3.2. Thermally Stimulated Current

Thermally stimulated techniques are well established methods to investigate trap states. Introduced for inorganic semiconductors they are already successfully adopted for organics. The underlying principle, the methods are based on, is quite simple. First of all, the traps are filled at sufficient low temperatures compared to the trap activation energy. Afterwards the temperature is linearly increased resulting in a successive release of the trapped charge carriers to the transport level due to the rise in thermal energy. The detrapping of the charge carriers can either be detected by recording the luminescence (*thermally stimulated luminescence, TSL*) or the current (*thermally stimulated current, TSC*). The former calls for charge carriers of both signs are trapped in the sample and the detrapped charge carriers recombine radiatively. The latter, in contrast, allows also to record unipolar traps but electrodes and an electric field are needed to extract the charges. The method used in this work is the thermally stimulated current technique. Therefore, although TSC and TSL are quite similar methods, the further considerations will focus on thermally stimulated current.

Trap filling can be achieved by illumination of the sample, thus generating excitons which have to be separated via an electric field in the device or assisted by traps (optical trap filling). Alternatively, charge carriers can be injected via the electrodes into the sample by applying a voltage (electrical trap filling). Thereby, with a proper choice of the electrode materials electrons or holes can be selectively injected, thus allowing to distinguish between electron or hole traps [142], whereas in the case of optical trap filling this distinction is not directly possible.

Afterwards, the sample is kept for a certain time at the same temperature (thermalization time), giving the charge carriers the chance to thermalize and filling up the deep states via forming the density of occupied states (DOOS). Subsequently to the thermalization time, the sample is heated with a constant heating rate. The charge carriers are activated from the trap states to the transport level and can be extracted from the sample via an electric field. The resulting current is recorded over temperature, resulting in a characteristic TSC signal for each sample, called TSC spectrum. An exemplary TSC spectrum with the corresponding characteristics of the temperature is shown in Figure 3.2. The spectra contain information about the energy, the concentration and distribution of the traps.

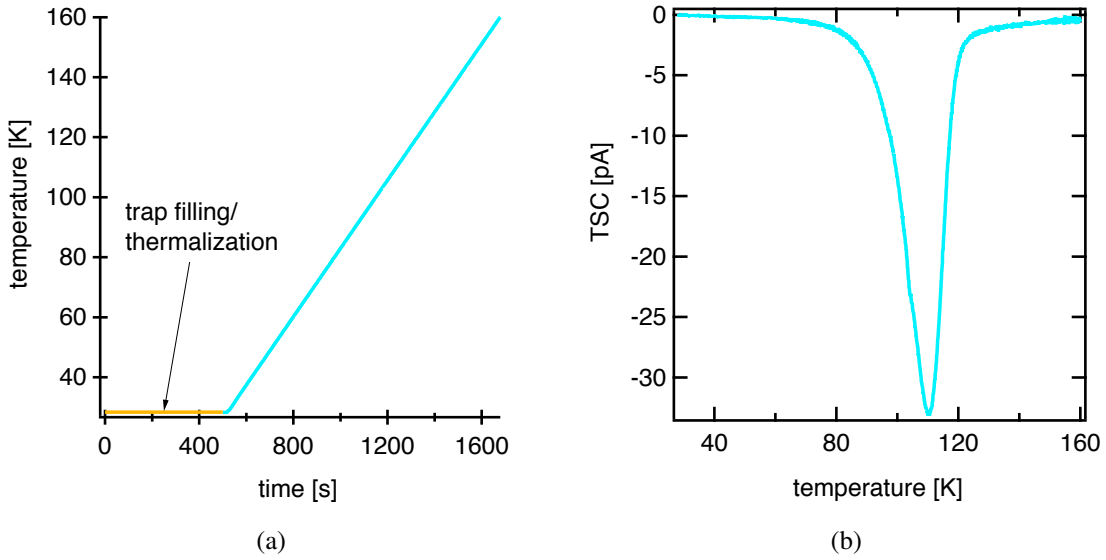

Figure 3.2.: Exemplary TSC spectrum (b) and the corresponding temperature (a).

A lower limit of trap density n_t can be obtained by integrating the TSC spectrum over time, according to the inequality [63]:

$$\int_{peak} I_{TSC} dt \leq q n_t V \quad , \tag{3.1}$$

with the elementary charge q and the sample volume V. The inequality is caused by the fact that the estimated trap density is only a lower limit of the actual one. This is caused by two reasons:

- incomplete trap filling

  Not every trap state has to be filled at the beginning of the measurement. In the case of optical trap filling, the incident light not only generates new electron–hole pairs but also can release already trapped charges from the traps, resulting in a specific equilibrium concentration of occupied traps. This equilibrium concentration can be lower than the trap density [63]. On the other hand, in the case of electrical trap filling, the trap induced electric field can annihilate the externally applied electric field. In this case further trap filling is not possible [63]. Furthermore, if the temperature at which trap filling is performed

is too high, shallow traps will not be filled or partially emptied during the thermalization time.

- recombination

  If charge carriers of both signs are present in the sample, they may recombine after they got detrapped. In the case of radiative recombination this results in TSL, as mentioned above. The recombined charge carriers do not contribute to the current. Thus, TSC and TSL rely on competing mechanisms.

Therefore, one has to bear in mind, that the measured trap density is only the lower bound of the actual one.

The analysis of the TSC spectrum concerning the activation energy and the distribution of the traps is more complicated, especially if there are not distinct monoenergetic traps present in the sample, but several trap levels each of them possessing an energetic distribution, as in the case of organic semiconductors. Despite this, in the following first of all the simplest model with one monoenergetic trap level is assumed, allowing to clarify many relations of the TSC signal with the different parameters, such as the trap activation energy.

3.2.1. Monoenergetic Trap Level

Already in 1960 Hearing and Adams [42] provided a theory to describe TSC spectra in inorganic semiconductors, by adapting existing models for thermally stimulated luminescence (in old publication also called *glow curves*) [39, 117]. Thereby, a simple model with a monoenergetic trap level (for simplicity electron traps are assumed, but the same considerations can be done for holes) with trap density N_t, capture cross section S and energy E_t relative to the conduction band (density of states N_c) was assumed, as shown in Figure 3.3. Thus, for the concentration of trapped electrons n_t the following rate equation can be given [42]:

$$\frac{dn_t}{dt} = -n_t N_c S \nu_{th} \exp\left(-\frac{E_t}{k_B T}\right) + n_c \left(N_t - n_t\right) S \nu_{th} \quad . \tag{3.2}$$

ν_{th} is the thermal velocity of the electrons in the conduction band, k_B the Boltzmann constant and T the temperature. The term $N_c S \nu_{th}$ has the unit s^{-1} and can be summarized to ν_0, called the attempt-to-escape frequency [25, 103], which is also used in the Miller-Abrahams equation (Equation 2.8). The first term in Equation 3.2 describes the release of electrons from the traps due to the thermal energy and the second term represents retrapping of electrons. For the change of the electron density in the conduction band n_c Hearing and Adams [42] derived:

$$\frac{dn_c}{dt} = -\frac{n_c}{\tau} - \frac{dn_t}{dt} \quad . \tag{3.3}$$

The first term in Equation 3.3 describes the loss of electrons in the conduction band due to recombination with holes in the valence band with the lifetime of the electrons in the conduction band τ and the second term represents the change of the electron density in the conduction band due to the change of the electron concentration in traps.

Choosing a constant heating rate b of the sample, the correlation between temperature T and time t is given by $T = T_0 + bt$, with the temperature before the beginning of the heating T_0. Thus, the time dependence of Equations 3.2 and 3.3 can be rewritten in a temperature

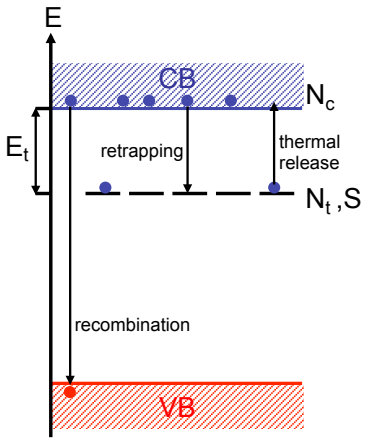

Figure 3.3.: Energetic scheme of a crystalline inorganic semiconductor with valence band (VB), conduction band (CB) and a monoenergetic trap level for electrons with energy E_t relative to the conduction band. N_c is the density of states of the conduction band, N_t the trap density and S the capture cross section of the traps. In addition, the possible transitions, Equations 3.2 and 3.3 are based on, are shown: thermal release of trapped electrons, retrapping of detrapped electrons and recombination between detrapped electrons in the conduction band and holes in the valence band.

dependence. The thermally stimulated current $I_{TSC}(T)$ is proportional to the electron density in the valence band [78]:

$$I_{TSC}(T) = A\,F\,q\,\mu\,n_c(T) \quad . \tag{3.4}$$

A is the active area of the sample, F the electric field, q the elementary charge and μ the mobility of the electrons in the conduction band.

To solve the differential equation system of Equations 3.2 and 3.3 analytically, further assumptions have to be made. Assuming that retrapping of electrons can be neglected, i.e. the reciprocal lifetime of the electrons in the conduction band is large compared to the retrapping possibility (first order kinetics), Hearing and Adams obtained the following equation for the TSC spectrum:

$$I_{TSC}(T) = AFq\mu n_{t0}\tau\nu_0 \exp\left(\frac{-E_t}{k_BT} - \frac{\nu_0}{b}\int_{T_0}^{T}\exp\left(\frac{-E_t}{k_BT'}\right)dT'\right) \quad . \tag{3.5}$$

n_{t0} is the density of initially occupied traps. The temperature dependencies of the mobility μ, the lifetime τ and the attempt-to-escape frequency ν_0 are thereby neglected.

In the other case, if retrapping is not neglected, Garlick and Gibson [39] derived the following second order equation:

$$I_{TSC}(T) = \frac{AFq\mu n_{t0}^2\tau\nu_0\exp\left(\frac{-E_t}{k_BT}\right)}{N_t\left[1+\frac{n_{t0}\nu_0}{N_t b}\int_{T_0}^{T}\exp\left(\frac{-E_t}{k_BT'}\right)dT'\right]^2} \quad . \tag{3.6}$$

Again, here the temperature dependencies of the mobility, the lifetime and the attempt-to-escape frequency are neglected. Note that in the case of second order kinetics, the shape of the TSC

spectrum depends on the ratio of initially occupied and total amount of traps $\frac{n_{t0}}{N_t}$, whereas in the case of first order kinetics the density of initially occupied traps only influences the amplitude of the TSC. In the literature a couple of further equations for the TSC in the presence of retrapping for different retrapping possibilities can be found [42, 78].

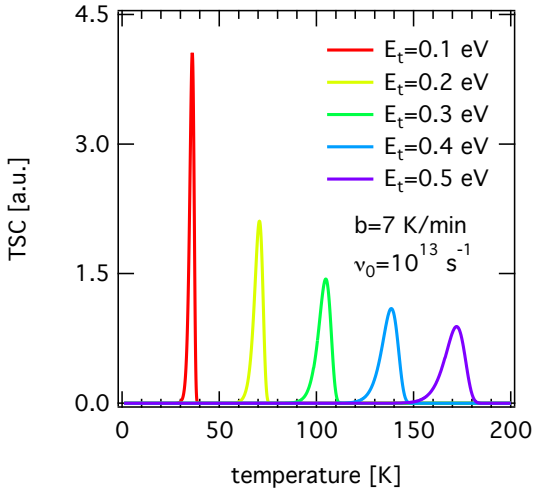

(a) variation of the trap activation energy E_t

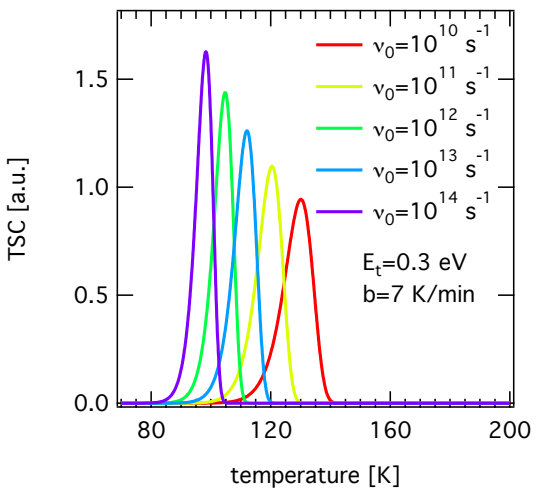

(b) variation of the attempt-to-escape frequency ν_0

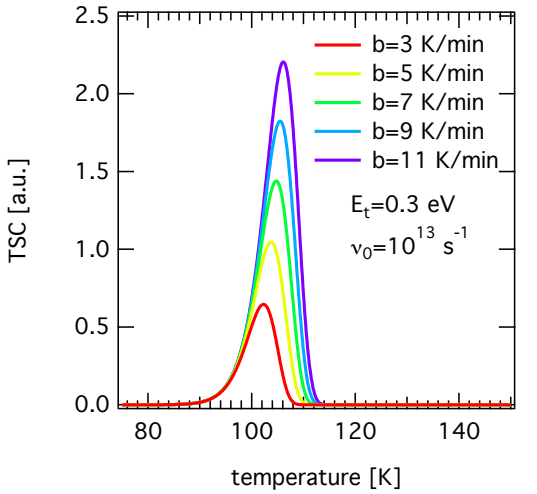

(c) variation of the heating rate b

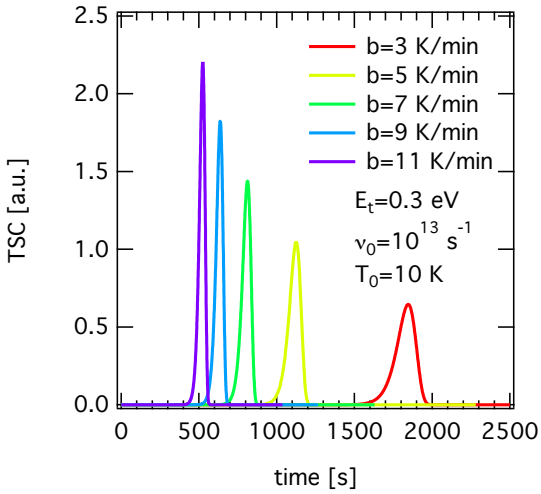

(d) variation of the heating rate b, the TSC is plotted over time

Figure 3.4.: Computed TSC spectra according to Equation 3.5 for varied parameters.

From Equations 3.5 and 3.6 it can be seen, that the TSC spectrum not only strongly depends on E_t but also on b and ν_0. In Figure 3.4 computed TSC spectra according to Equation 3.5 are shown, for different values of E_t, ν_0 and b. Since the thermal activation of the trapped electrons into the conduction band is a statistic process, the TSC spectrum is not a singular peak, but yields a temperature distribution even for a monoenergetic trap level (Figure 3.4). The width of the TSC spectrum depends on the activation energy of the traps, the heating rate and the attempt-to-escape frequency. The deeper the trap states, the faster the heating and the lower the attempt-

to-escape frequency, the broader the spectrum. Thereby, the TSC exhibits an initial exponential increase, which is determined by the first term in the exponent in Equation 3.5. With increasing emptying of the traps, the TSC reaches a maximum and then decreases continuously, as the second term in the exponent of Equation 3.5 gets more dominant. The TSC spectrum shifts to higher temperatures with increasing trap activation energy, since a higher thermal energy is necessary to release the trapped charge carriers (Figure 3.4a). Furthermore, a lower attempt-to-escape frequency and higher heating rate result in a shift of the TSC to higher temperatures (Figure 3.4b,c). This is again originated by statistic reasons. The less frequently the charge carriers attempt to escape from the traps (lower ν_0), the later they get detrapped. If the heating rate is the same, a later time means a higher temperature. As one can see from Figure 3.4c, a higher heating rate causes a higher TSC. The reason therefore is the difference in time. Plotting the current over time (Figure 3.4d) it gets obvious that the area under the TSC spectrum stays the same, independent of the heating rate, and thus the amount of extracted charges.

Although the influence of the different parameters on the TSC was shown in the case of first order kinetics (Equation 3.5) it is similar in the case of second order kinetics, corresponding to Equation 3.6. A comparison of a first order kinetic and a second order kinetic TSC spectrum is shown in Figure 3.5. Due to the retrapping events, the second order TSC spectrum exhibits a higher current at the high temperature side of the TSC. Both spectra are normalized to give the same maximum, for better comparison.

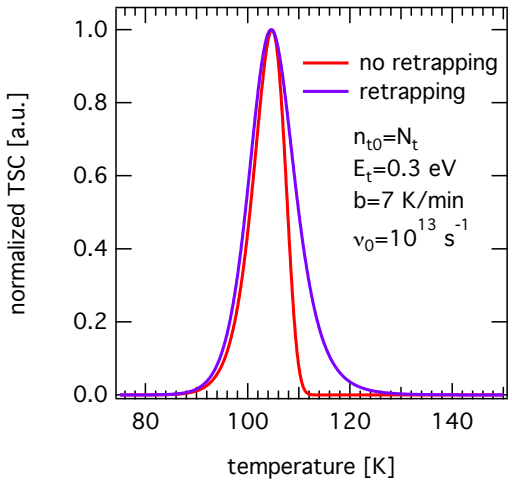

Figure 3.5.: Comparison of a first order kinetic TSC (Equation 3.5) (red line) and a second order kinetic TSC (Equation 3.6) (blue line). The spectra are normalized to give the same maximum. In the case of second order kinetics it was assumed that all traps are filled at the beginning of the measurement ($n_{t0} = N_t$).

In general Equations 3.5 and 3.6 can be used to fit the measured TSC spectra, with using E_t and ν_0 as fitting parameters and in the case of second order kinetics also the ratio of n_{t0} and N_t. Since in general the mobility, the lifetime and the attempt-to-escape frequency are temperature dependent this introduces even more fitting parameters and further complicates the fitting. In the literature several other methods to derive the activation energy of the traps are presented, based on the TSC equations, but these methods in most cases require the knowledge of the kinetics [90, 103]. One example to estimate the trap depth in the case of first order kinetics is

the method introduced by Hoogenstraaten [49] where the TSC is recorded for different heating rates. As already shown in Figure 3.4c, the maximum of the TSC shifts to higher temperatures with increasing b. This is the basic principle of this method. Differentiating Equation 3.5 with respect to T and setting equal to zero to find the condition for the TSC maximum yields:

$$\exp\left(\frac{E_t}{k_B T_{max}}\right) = \frac{\nu_0 k_B T_{max}^2}{b E_t} \quad . \tag{3.7}$$

Hereby, T_{max} is the temperature of the TSC maximum. Plotting $\ln \frac{T_{max}^2}{b}$ against $\frac{1}{T_{max}}$ for different heating rates yields a straight line with slope $\frac{E_t}{k_B}$ from which E_t can be calculated.

Another often used method to derive the activation energy of the traps is the *initial rise* method introduced by Garlick and Gibson [39]. The method is based on the fact that when the traps begin to empty by increasing the temperature, the integrals of Equations 3.5 and 3.6 are negligibly small and therefore the TSC is

$$I_{TSC} \propto \exp\left(-\frac{E_t}{k_B T}\right) \quad , \tag{3.8}$$

at the beginning of the TSC peak. Plotting the logarithm of the TSC against $\frac{1}{T}$ (*Arrhenius plot*) yields a straight line in the beginning of the TSC, from which the activation energy of the traps can be estimated. This method is independent of the TSC kinetics. Another advantage of the *initial rise* method is that only a small temperature range in the beginning of the TSC peak is needed to obtain E_t and therefore the temperature dependencies of the different parameters (e.g. the mobility) can be neglected.

To distinguish whether the measured TSC is of first order kinetics or second order kinetics, Halperin and Brander [45] used a method based on analyzing the symmetry of the TSC peak. However, this method is only suitable in the case of distinct trap levels, since overlapping TSC peaks influences the shape of the TSC and the method fails in the case of continuous trap distributions.

3.2.2. Continuous Trap Distribution

If the trap states within the semiconductor are not monoenergetic, but yield – as in the case of organic semiconductors – an energetic distribution, Equations 3.5 and 3.6 have to be adapted by additionally integrating over the energy distribution of the traps. In the case of no retrapping (Equation 3.5) the TSC becomes:

$$I_{TSC}(T) \propto \nu_0 \int_{-\infty}^{\infty} dE \rho_0(E) \exp\left(\frac{-E}{k_B T} - \frac{\nu_0}{b}\int_{T_0}^{T} \exp\left(\frac{-E}{k_B T'}\right) dT'\right) \quad . \tag{3.9}$$

$\rho_0(E)$ is the density of occupied states (DOOS) after the trap filling and is given by the relaxation of the charges and E is the energetic difference of the traps to the transport level. An equation for second order kinetic trap distributions can be found in the same manner.

In Figure 3.6 computed TSC spectra according to Equation 3.9 are shown. Thereby, a Gaussian distributed DOOS (Equation 3.10) with the center of distribution at E_t=0.3 eV below the

transport level was assumed:

$$\rho_0(E) = \frac{N_t}{\sigma\sqrt{2\pi}} \exp\left(\frac{-(E-E_t)^2}{2\sigma^2}\right) \quad . \tag{3.10}$$

σ is the width of the Gaussian distribution. For comparison the TSC of a monoenergetic trap ($\sigma = 0$ meV) is also given in Figure 3.6. With increasing σ the TSC spectrum gets broader.

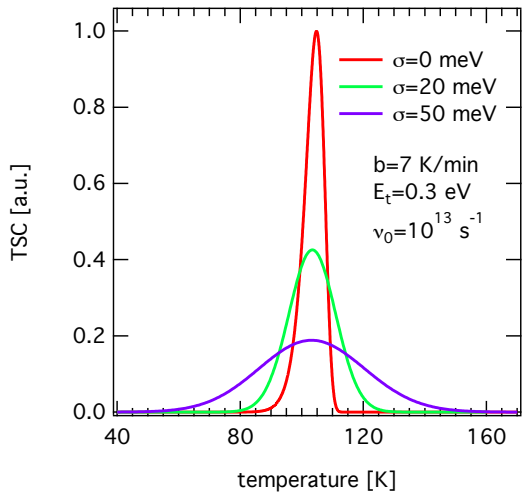

Figure 3.6.: Computed TSC spectra according to Equation 3.9 and a Gaussian distributed DOOS (Equation 3.10) for different values of σ. The case of σ=0 meV corresponds to a monoenergetic trap level (Equation 3.5).

As already mentioned in Section 2.4, the transport level in organic semiconductors is not a constant value, but changes with temperature. Therefore, Equation 3.9 becomes [6, 7, 65]:

$$I_{TSC}(T) \propto \nu_0 \int_{-\infty}^{\infty} dE \rho_0(E) \exp\left(\frac{-(E_{tr}(T)-E)}{k_B T} - \frac{\nu_0}{b}\int_{T_0}^{T} \exp\left(\frac{-(E_{tr}(T')-E)}{k_B T'}\right) dT'\right) \quad , \tag{3.11}$$

with the transport energy E_{tr}.

As the fitting of measured TSC spectra in the case of monoenergetic trap states is not trivial to handle, due to the several unknown parameters, it is in the case of organic semiconductors –with trap distributions and a temperature dependent transport energy– almost impossible. Hence, a often used method to get information about the trap activation energy and the trap distribution is the fractional TSC measurement, which will be introduced in the next section.

3.2.3. Fractional TSC

The method of fractional TSC measurements is based on an extension of the above introduced *initial rise* method for monoenergetic traps (Equation 3.8). In the case of a trap distribution, the initial rise is mainly determined by the shallowest occupied traps. If not the complete TSC spectrum is recorded, as in the standard TSC measurement, but instead the sample is only heated

to a certain temperature T_{Stop} (*prerelease*), with successively cooling the sample down to the initial temperature T_{Start}, only the shallow traps get emptied. Heating the sample again with a constant heating rate over the complete temperature range of the TSC spectrum (*main run*), without new trap filling, again an exponential increase in the initial rise of the TSC can be observed. This time, the initial rise is once again dominated by the shallowest occupied traps and thus by deeper states than in the prerelease. This can be used to determine the distribution of activation energies by several measurement cycles with increasing T_{Stop}. This kind of a fractional TSC is called T_{Start}–T_{Stop} method [124, 142]. In Figure 3.7 one cycle of the T_{Start}–T_{Stop} method is shown for illustration.

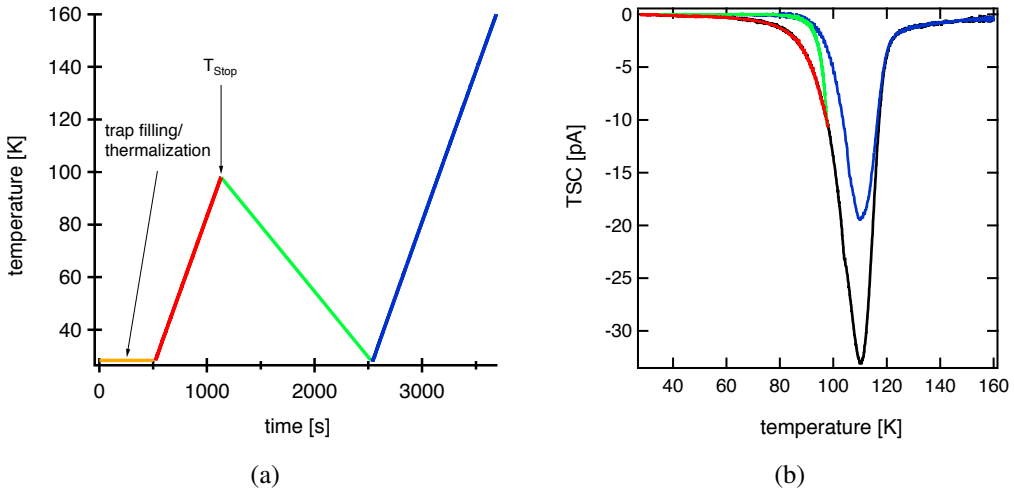

Figure 3.7.: TSC signal of a single measurement cycle of the T_{Start}–T_{Stop} method (b) and the corresponding temperature characteristic (a): prerelease (red), cool down (green) and main run (blue). For comparison the TSC spectrum of the standard TSC measurement is also shown (black).

According to Equation 3.1 the lower limit of the released charge carrier density for every main run can be estimated. Subtracting the charge carrier density of two successive main runs yields the released charge carrier density per T_{Stop} interval. Via the Arrhenius plot of the initial rise of the TSC for each main run, one gets the activation energy for each T_{Stop}. Altogether, for each activation energy a trap density can be assigned, yielding a reconstruction of the DOOS [124] relative to the transport level.

Information about the kind of the trap states, in matters of their energy distribution (i.e. whether the traps are monoenergetic, a distribution of monoenergetic trap levels or a continuous trap distribution) can also be obtained by plotting the temperature of the TSC maximum (T_{max}) of each main run against the corresponding T_{Stop} [89, 90]. An illustration of this correlation is shown in Figure 3.8 for a single monoenergetic trap level (a), several monoenergetic trap levels, resulting in still distinct TSC peaks (b) and a quasi–continuous trap distribution (c), according to McKeever [89, 90].

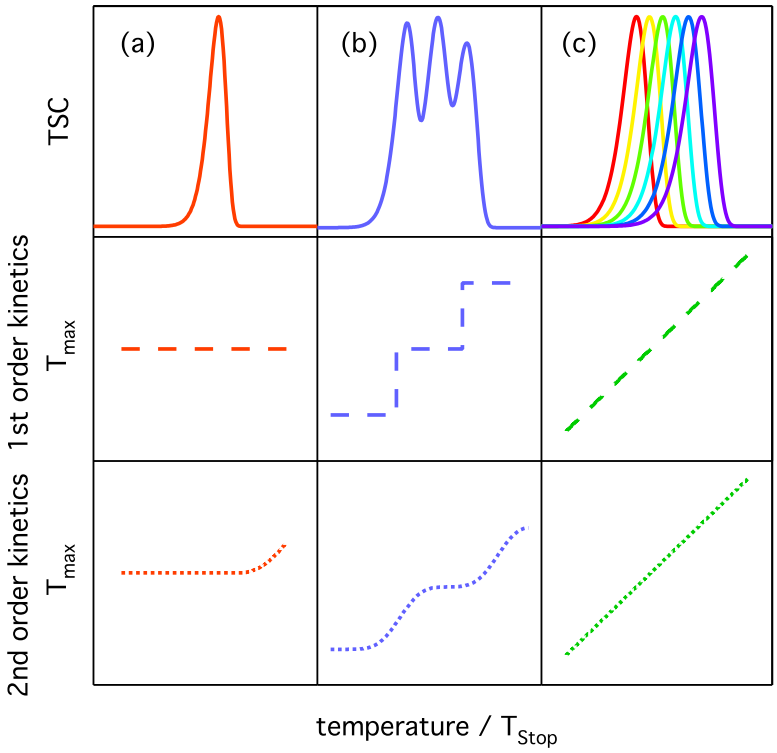

Figure 3.8.: Schematic TSC spectra of a single monoenergetic trap level (a), several monoenergetic trap levels, resulting in still distinct TSC peaks (b) and a quasi–continuous trap distribution (c) with the according temperatures of the TSC maxima (T_{max}) of each main run of a fractional TSC measurement plotted against the corresponding T_{Stop} for first order kinetics (dashed lines) and second order kinetics (dotted lines). After McKeever [89, 90].

A single monoenergetic trap level results in the case of first order kinetics in a constant maximum temperature independent of T_{Stop}, since only the number of trapped charges changes with T_{Stop} but not the activation energy; therefore the TSC peak remains on the same position. A monoenergetic trap and a second order kinetic first results in a constant T_{max} (if T_{Stop} is appreciably less than T_{max}) and increases at first slowly and then more rapidly with increasing T_{Stop}. This is caused by the fact that the position and shape of a second order TSC is dependent on the ratio of filled traps (see Equation 3.6) with a shift of the TSC maximum to higher temperatures for less filled trap states. This is in contrast to the first order kinetic, where the number of filled traps only influences the height but not shape and position of the TSC (see Equation 3.5). For a TSC spectrum with several separated first–order TSC peaks the T_{max}–T_{Stop} plot reveals a staircase with a flat region for each individual peak. The closer are the trap levels and the more the TSC peaks overlap, the smoother the staircase becomes, resulting in a straight line of slope ~ 1 in the case of a quasi–continuous or a continuous trap distribution [89, 90]. In the case of several separated second–order TSC peaks the T_{max}–T_{Stop} plot also reveals a staircase, but this one is much smoother than that of first order kinetics, for the same reason T_{max} increases with T_{Stop} for a single monoenergetic second–order TSC. But again, each flat region corresponds to a trap

level. In the case of closely overlapping TSC peaks the T_{max}–T_{Stop} plot for second order kinetics also becomes a straight line of slope ~ 1.

Rudlof et al. [120] simulated glow curves and the resulting distribution obtained by the fractional technique for a first order Gaussian distribution of traps. Thereby, they revealed that the distribution obtained by the fractional method yields a steeper rise than the input distribution. This can be explained by the fact that traps within a range of approximately $2.45k_BT$ contribute to the detrapping rate at a temperature T. Since a Gaussian distribution exhibits less traps with low activation energies compared to the center of distribution, the initial rise is already influenced by deeper traps. This also results in a slight shift of the distribution maximum obtained by the fractional technique to higher energies compared to the input distribution. The drop of the measured distribution, however, is somewhat faster than that of the input function. But altogether the fractional measurements yield an adequate image of the real trap distribution.

So far, the fractional TSC is probably the best method to obtain information on the activation energies and distribution of trap states in organic semiconductors.

3.3. Deep Level Transient Spectroscopy

Deep level transient spectroscopy (DLTS) was introduced by Lang [72] in 1974 to investigate trap states at p–n junctions or Schottky contacts. The basic principle can be summarized as follows: A p–n junction or Schottky contact is perturbed by a voltage or a light pulse, resulting in the filling of trap states. After the filling pulse, trapped charge carriers relax back to the steady-state condition. The relaxation time is given by the emission rate of the charge carriers from the trap states to the transport level. Thereby, the emission process can be observed either as a capacitance (C-DLTS) or a current (Q-DLTS) transient. The transient yields information about the trap concentration and the activation energy of the traps. In the case of C-DLTS also the polarity of the detrapped charge carriers (i.e holes or electrons) can be determined. In the case of Q-DLTS this can only be done indirectly by using a voltage pulse in forward direction for trap filling and selective electrodes.

In this work, only the Q-DLTS method was used and therefore the further detailed considerations are restricted to the current transients.

3.3.1. Q-DLTS Model

The principle of a Q-DLTS measurement is shown in Figure 3.9. The sample, which is in thermal equilibrium at the beginning of the measurement, is perturbed by a positive voltage pulse, rising the Fermi level. The injected charge carriers relax into the trap states. Switching the external voltage off, the sample relaxes back to steady-state condition by thermal release of the trapped charge carriers to the transport level, resulting in a current transient.

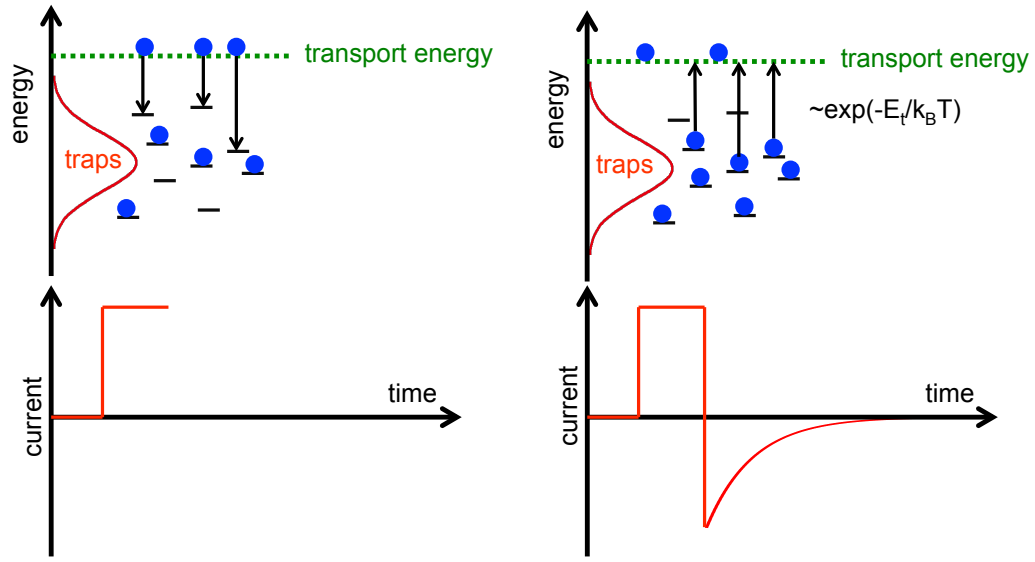

Figure 3.9.: Scheme of a Q-DLTS measurement with positive voltage pulse for trap filling. Filling and emptying of the trap states (top) and resulting current (bottom).

Starting point of the theoretical considerations of the current transient is again a single monoenergetic trap level for electrons, as introduced in Section 3.2.1 (see Figure 3.3) and the cor-

responding rate equation for the concentration of trapped electrons (Equation 3.2). Neglecting retrapping, the time dependence of trapped electrons can be written as:

$$n_t(t) = n_{t0}\exp(-e_t t) \tag{3.12}$$

with n_{t0} the density of trapped electrons after the filling pulse and e_t the emission rate from the traps, given by:

$$e_t = N_c S \nu_{th} \exp\left(\frac{-E_t}{k_B T}\right) \tag{3.13}$$

The prefactor $N_c S \nu_{th}$ is again the attempt-to-escape frequency ν_0. Assuming that recombination of free charge carriers can be neglected and after the filling pulse no more charge carriers are generated within the sample (i.e the current is only caused by detrapped electrons), the current transient is proportional to the change of trapped electrons $\frac{dn_t(t)}{dt}$ and yields:

$$I(t) = -dAq\frac{dn_t(t)}{dt} = dAqn_{t0}e_t \exp(-e_t t) \tag{3.14}$$

d is the sample thickness, A the active area of the sample and q the elementary charge. Although Equation 3.14 was deduced for electrons due to simplicity, it is also valid for holes.

In an organic semiconductor the trap levels are not monoenergetic, but distributed in energy, thus, the emission rates also yield a distribution $g(e)$, as the emission rate depends on the trap activation energy (Equation 3.13). Hence, the current transient is given by integrating over the emission rates e:

$$I(t) = dAq\int_0^\infty g(e)\, e \exp(-et)\, de \tag{3.15}$$

Since every emission rate can be assigned to an activation energy, by recording the current transient and determining the emission rate distribution $g(e)$, information about the distribution of initially occupied states (DOOS) $\rho_0(E)$ can be obtained.

3.3.2. Evaluation

The challenge of analyzing the measured current transients is in obtaining the emission rates of the traps. In the following two possible methods for analyzing exponential transients are introduced, namely the Boxcar analysis and the Tikhonov regularization.

- Boxcar method

  The classical method to analyze exponential transients is the Boxcar method introduced by Lang for DLTS and up to now it is still the mainly used method in this context. This method was developed, when it was not possible to record fast exponential transients with a sufficient high time resolution due to limitations of the experimental setup. In this cases the Boxcar method offered the opportunity to determine the time constant of an exponential decay by repeatedly measuring the amplitude of the transient at two successive times, which are in a fixed correlation. Assuming a monoexponential decay with emission rate e_t the Boxcar signal by measuring the amplitude at time t_1 and t_2 is:

  $$\Delta I(t_1, t_2) \propto [\exp(-e_t t_1) - \exp(-e_t t_2)] \tag{3.16}$$

Writing t_1 and t_2 as $\tau_{set} = \frac{t_2 - t_1}{\ln(t_2/t_1)}$ with a fixed ratio $\frac{t_2}{t_1}$ it can be shown that the Boxcar signal (Equation 3.16) has a maximum, when the time window τ_{set} equals the time constant of the exponential decay $\tau = e_t^{-1}$ [72]. This relation is valid in the case of C-DLTS.

For current based DLTS (Equation 3.14), however, the Boxcar signal for a monoexponential decay is:

$$\Delta I(t_1, t_2) \propto e_t \left[\exp(-e_t t_1) - \exp(-e_t t_2)\right] \tag{3.17}$$

In this case, the time window τ_{set} has to be defined by $\frac{t_2 - t_1}{\tau_{set}} = \ln\left(\frac{1 - t_2/\tau_{set}}{1 - t_1/\tau_{set}}\right)$ to get the Boxcar maximum when τ_{set}=τ [12].

Rerunning the measurements with varying the time window, or varying the time constant of the decay (by varying the temperature) with constant τ_{set} (Figure 3.10), the emission rate can be determined. If it is possible to record the whole transient with sufficient time resolution within one run, the Boxcar method is numerically applied to the data points.

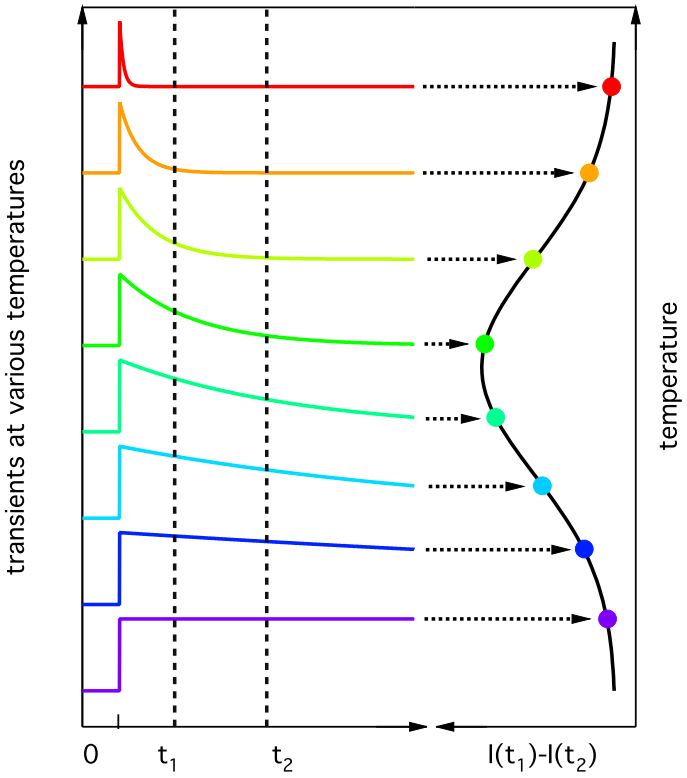

Figure 3.10.: Scheme of the Boxcar method. The left–hand side shows an exponential transient at various temperatures. On the right–hand side the corresponding DLTS signal resulting from the Boxcar method is shown, which is given by the difference of the transients at time t_1 and t_2 as a function of temperature. The Boxcar signal is maximum when the time window τ_{set} (the definition is given in the text) equals the time constant τ of the exponential decay. Thus, the emission rate $e_t = \tau^{-1}$ of the traps at the corresponding temperature can be obtained. After Lang [72].

- Tikhonov regularization method

  The current transient in the case of a continuous distribution of emission rates was already given above (Equation 3.15). Rewriting Equation 3.15 with $dAqg(e)e = f(e)$ yields:

$$I(t) = \int_0^\infty f(e) \exp(-et)\, de \tag{3.18}$$

  Thus the current transient $I(t)$ is the Laplace transform of $f(e)$. In principle, $f(e)$ can be obtained analytically, by taking the inverse Laplace transform of the transient $I(t)$ [57]:

$$f(e) = \int_{c-i\infty}^{c+i\infty} I(t) \exp(et)\, dt \quad , \tag{3.19}$$

  where c is a real constant. However, for the inverse Laplace transform the integration in the complex plane is required, which can not be simplified on the real axis in the case of exponentials [57]. Yet, from the measurement data, only values of $I(t)$ along the real axis are known. Thus, $g(e)$ can only be found by solving the Laplace transform (Equation 3.18), which belongs to a more general class of Fredholm integral equations of the first kind, which are known as ill posed [57]. To solve them, approximative regularization methods were developed.

  With the Tikhonov regularization method an approximative solution of the Fredholm integral equation can be obtained. Therefore, a functional from the difference of the Fredholm integral equation and the measurement data $I(t)$ is formed, which is minimized by variation of the wanted approximation $f(e)$ [57]:

$$M_\alpha[f(e)] = \left|\left| \int_a^b K(t,e) f(e) de - I(t) \right|\right| + \alpha\Omega[f(e)] \tag{3.20}$$

  The kernel $K(t,e)$ is here the temporal exponential decay: $K(t,e) = \exp(-et)$. The regularization is given by the last term of Equation 3.20. $\Omega[f(e)]$ is the regularization functional and α the regularization parameter, which determines the balance between the exact and a smoothed solution of Equation 3.18. $\Omega[f(e)]$ is either the identity of $f(e)$ or the second derivative [145]. The regularization on the one hand causes smoothing of the measurement data, thus noise is not misinterpreted as an exponential decay, therewith the solution gets stable, i.e. it changes continuously with continuously changing input data. On the other hand if α is large, the solution will be smooth and stable, but a significant part of the physical information contained in $I(t)$ will be lost [57].

  For the numerical realization of the Tikhonov regularization method the FORTRAN program FTIKREG [145] is used in this work. For a reasonable analysis of the measurement data, the method for determining the optimal regularization parameter α, integrated in the program, is important. FTIKREG uses a linear Tikhonov regularization, which requires an adequate smoothness of the wanted spectral distribution. Since in the case of organic semiconductors Gaussian or exponential distributions are expected, this is feasibly. To analyze measurement data with sharp peaks in the spectra, the more general nonlinear regularization, as implemented in the program NLREG [146], has to be used.

  For the analyzation of the emission rate spectra, the time window in which a solution of the Fredholm integral equation is expected, has to be committed to FTIKREG as a

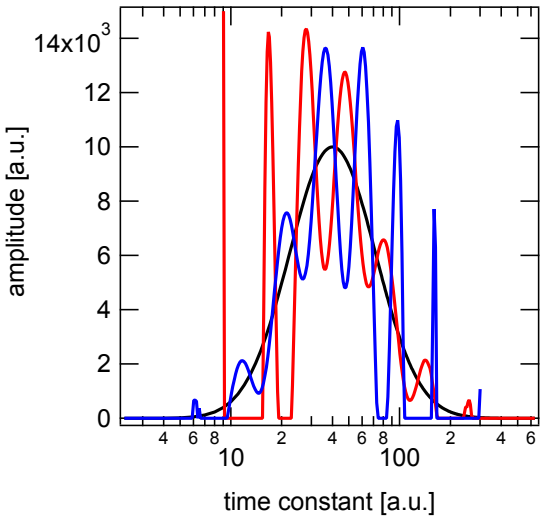

Figure 3.11.: Artifacts occurring if the time window for the Tikhonov regularization is restricted at low time constants (red) or high time constants (blue) to the time constant distribution (black). After [101].

parameter. If the time window is set too low (not containing the whole time constant distribution of the measured transient) , this results in artifacts distorting the real time constant distribution, as shown in Figure 3.11.

The main feature for the analysis of multiexponential decays is the resolution, i.e. the smallest ratio of two emission rates which can be distinguished. Thereby, the limitations are the signal–to–noise ratio (SNR), the stability of the environmental conditions during the measurement, the time resolution of the measurement and the recording time of the transient. After Istratov [57], the Tikhonov regularization method yields for a given SNR the best resolution of all compared methods.

A comparison between the Boxcar method and the Tikhonov regularization method for a given emission rate distribution (consisting of three logarithmic Gaussian emission rate distributions with width 1.07, 1.07 and 1.2, distribution centers 30, 50, 300 and amplitudes 10000, 10000, 3000 in arbitrary units) is shown in Figure 3.12.

The resulting transient yields two inflection points (Figure 3.12b) due to the three emission rate distributions the transient consists of. The analysis of the transient with the Tikhonov regularization method exhibits a good agreement with the input data both in amplitude and resolved time constants (Figure 3.12c). The Boxcar method (Figure 3.12d), however, only resolves emission rates which differ in more than one order of magnitude. Also the amplitude is not reproduced correctly, due to the continuous emission rate distributions instead of monoenergetic ones. Therefore, the Tikhonov regularization was the method of choice in this work to analyze the current transients of the organic semiconductors. The implementation of the FTIKREG program into the data analyzing process was done by Stefan Neugebauer [101].

From the Arrhenius plot of the obtained emission rates the trap activation energies can be received (see Equation 3.13). Thereby, in the case of organic semiconductors, either e_t/T^2 [40, 102] or e_t [58] is plotted over $1/T$. The former is in analogy to the analysis of inorganic semiconductors, which show temperature dependencies of the effective density of states

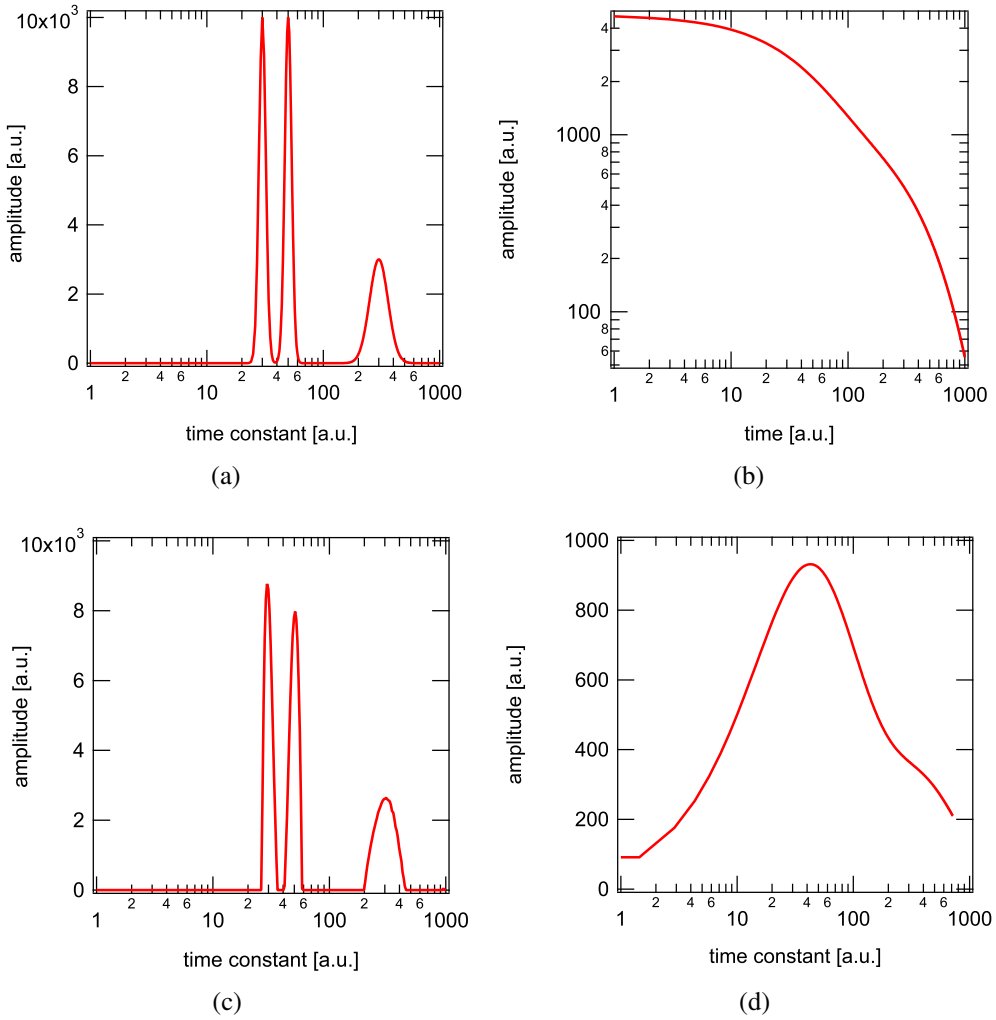

Figure 3.12.: Calculated transients (b) for a given logarithmic Gaussian emission rate distribution (a) and the resulting emission rate spectra obtained by using Tikhonov regularization method (c) and Boxcar method (d). After [101].

$N_c \propto T^{3/2}$ and the thermal velocity $v_{th} \propto T^{1/2}$ and neglects a possible temperature dependence of the capture cross section. In the latter, the temperature dependence of the attempt-to-escape frequency is completely neglected, in analogy to the Miller–Abrahams equation (Equation 2.8). According to this simplification, the temperature dependence of ν_0 is also neglected in this work.

4. Experimental Methods

In this chapter a short description of the sample preparation (Section 4.1) and the details of the experimental setups (Section 4.2), mainly used in this work, will be given.

4.1. Sample Preparation

A scheme of the device configuration is shown in Figure 4.1. As substrates indium tin oxide

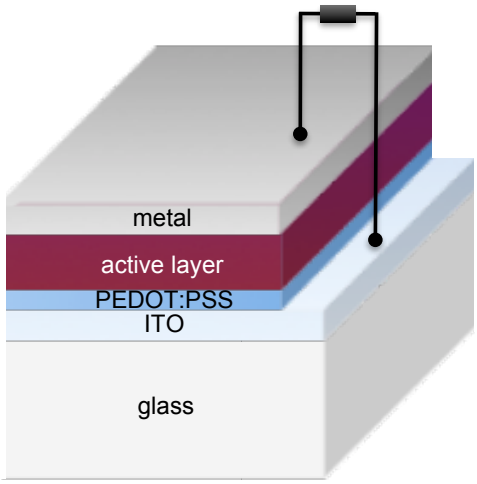

Figure 4.1.: Structure of the investigated samples.

(ITO) (100-200 nm) covered glass (1.1 mm) with a 25 nm SiO_2 passivation layer between glass and ITO was used for all of the investigated samples. The ITO, acting as anode, had a sheet resistance of about 15 $\Omega/\square$. The substrates were purchased from Visiontek Systems Ltd. First of all, the substrates were structured by optical lithography performed as follows:

- cleaning of the substrates
  - mechanical pre-cleaning with deionized soap water
  - ultrasonic bath for 10 min in deionized soap water
  - rinse with deionized water
  - ultrasonic bath for 10 min in acetone
  - ultrasonic bath for 10 min in isopropanol
- optical lithography of the substrates
  - heating step of 120 °C for 10 min

  - spin-coating of the photoresist (AZ 1518, MicroChemicals): 3000 rpm, acceleration 1 s, 60 s
  - heating step of 100 °C for 50 s
  - UV light exposure for 59 s using a shadow mask
  - development of the photoresist: developer (AZ 351B, MicroChemicals):H_2O 1:3, 2×30 s
  - neutralization with deionized water
  - heating step of 120 °C for 1 min

- etching of the substrates
  - H_2O:HCL:HNO_3 12:12:1, 11 min in ultrasonic bath
  - neutralization with deionized water
  - removing of the photoresist with acetone

Before sample fabrication, the substrates were cleaned once more, as described above. Afterwards, poly(3,4-ethylenedioxythiophene):(polystyrenesulfonate) (PEDOT:PSS) (purchased from H. C. Starck (*CLEVIOS P VP AI 4083*)) was spin coated on the substrates acting as hole transport layer (thickness about 40 nm). After transferring the samples into a nitrogen filled glovebox a heating step of 130 °C for 10 min was applied to remove residual water and to enhance the conductivity of the PEDOT:PSS layer.

Afterwards the active layer was spin coated from solution (solvent: chlorobenzene or chloroform). In the case of P3HT:PC_{61}BM blends a further annealing step of 10 min at 130 °C was applied to improve the morphology of the blends. Top contacts (Al, Ca/Al or LiF/Al) were evaporated thermally with a base pressure during evaporation of $< 1 \times 10^{-6}$ mbar in an evaporation chamber directly attached to the glovebox system. The effective areas of the investigated samples were about 9 mm^2.
All layer thicknesses were measured with a profilometer (*Dektak 150, Veeco*).
Further sample specific details will be given in the corresponding chapters.

4.2. Experimental Setups

In this section the experimental equipment for TSC, Q-DLTS and IV measurements will be briefly presented, as well as the standard measurement parameters. If not otherwise stated, these parameters were used for the measurements presented in this work.

4.2.1. TSC Setup

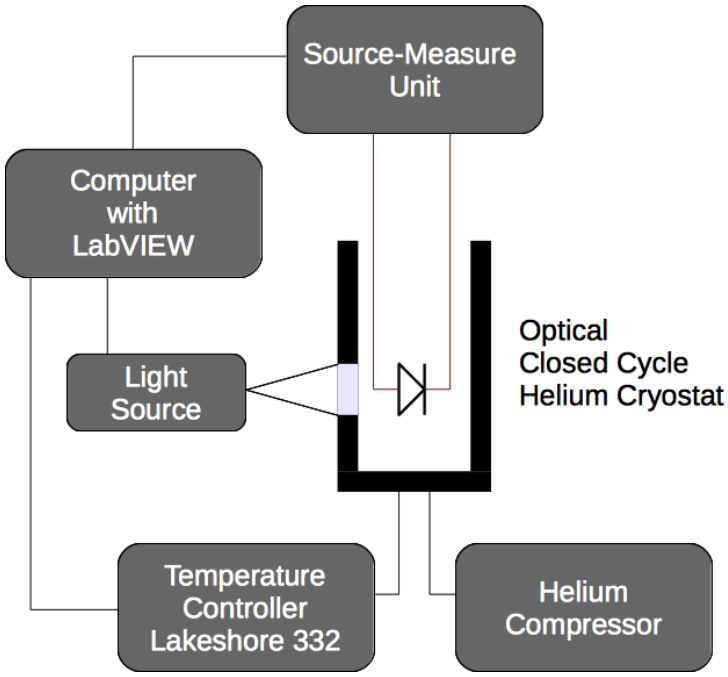

Figure 4.2.: The experimental setup used for thermally stimulated current (TSC) measurements.

The setup for thermally stimulated current measurements is shown schematically in Figure 4.2. TSC measurements were performed in a closed cycle Helium cryostat with Helium as contact gas. Two cryostat systems were used: A *Janis CCS 550* and a *CryoVac* cryostat. The latter had the advantage of an integrated sample lock, allowing the samples to be transferred from the glovebox to the cryostat without exposure to air. Both systems were equipped with two temperature sensors and two heaters. One sensor–heater pair was located near the cold head, the other one at the sample holder, slightly above the sample. The two sensors and heaters were necessary to avoid a large temperature gradient within the sample chamber of the cryostat and to perform linear temperature ramps. The heating was performed against the active cooling of the compressor. The heaters and sensors were controlled and read out by a *Lakeshore 332* temperature controller. The available temperatures of the cryostats ranged from about 20 K to 320 K. The standard heating rate for the TSC measurements was 7 K/min.

In the case of the Janis cryostat, the samples were contacted to the wires by small pieces of Indium, whereas in the CryoVac system the samples were contacted via pins. Both cryostats were equipped with BNC cables. Thermally stimulated current was detected by either a *Keithley 237* Source Measure Unit or a *Keithley 6430* Sub-Femtoamp Remote Source Meter. If desired

they also served as voltage source. However, in most of the cases the TSC signals were detected without applying an external field, implying that the detrapped charge carriers were extracted from the samples only due to the built–in voltage, given by the workfunction difference of the electrodes. In some cases applying a small voltage of a few μV was necessary to suppress leakage currents.

Trap filling was achieved by illumination of the samples through the optical window of the cryostat at about 20 K for five minutes using either a 10 W high power white light emitting diode (*Seoul*) or a 150 W halogen lamp. Before linearly increasing the temperature, a dwell time of five minutes after illumination was used allowing the charge carriers to reach thermal equilibrium.

4.2.2. Q-DLTS Setup

Current based deep level transient spectroscopy measurements were performed in the CryoVac cryostat system described above. The challenges in performing Q-DLTS were in measuring the current transients with an appropriate time resolution and high signal–to–noise ratio. However, a low noise level is only possible by limiting the time resolution. During the transient measurements the current changed about 9 orders of magnitude and the time at least 5 orders of magnitude. Therefore, the setup had to enable a dynamic adjustment of the measurement range as well as the time resolution, permitting an appropriate time resolution at the beginning of the transients and also recording the low currents at the end of the transients still with a good signal–to–noise ratio. This was achieved by using an A/D converter system (*ADwin Gold*), which handled the measurement data via an integrated processor in real time and controlled the setup accordingly. To apply the injection pulse for trap filling to the sample a D/A converter channel of the ADwin Gold with variable voltages between -10 V and 10 V and a maximum current of 10 mA was used. The transients themselves were measured without applying an external field, implying that the detrapped charge carriers were extracted only due to the built–in voltage, in analogy to the TSC measurements. To uncouple the output channel of the ADwin Gold from the measurement signal after the voltage pulse and thus avoiding the noise of the output channel to couple into the transients, a relay with a bounce time of about 3 ms was used. The current measurements were carried out by using a transimpedance amplifier (*FEMTO-DLPCA-200*). The amplifier stages, ranging from 10^3 V/A to 10^9 V/A, could be set via a parallel interface. Furthermore, the amplifier featured a manual offset compensation, allowing to adjust the offset current of the sample in this way that it is in the range of -10^{-12} A to -10^{-13} A for all investigated temperatures. Thereby, it could be ensured that there is no zero crossing during transient recording, which would have resulted in a deformation of the transients and thus complicated the analysis. The Q-DLTS setup is illustrated schematically in Figure 4.3.

During the voltage pulse for trap filling, the amplifier was kept in the least sensitive measurement range to enable high currents and was switched to the 10^7 V/A range at the beginning of the transients. A consequence thereof was a short-term overload and an unavoidable dead time of a few ms. A further switch of the amplifier to the 10^9 V/A level was performed as soon as the transients dropped below 10 nA. At the beginning of the transients, the current values were recorded with a time resolution of 100 μs. Then, the resolution was stepwise decreased up to 100 ms at the end of the measurement, to improve the signal–to-noise ratio. The standard transient record time was 80 s.

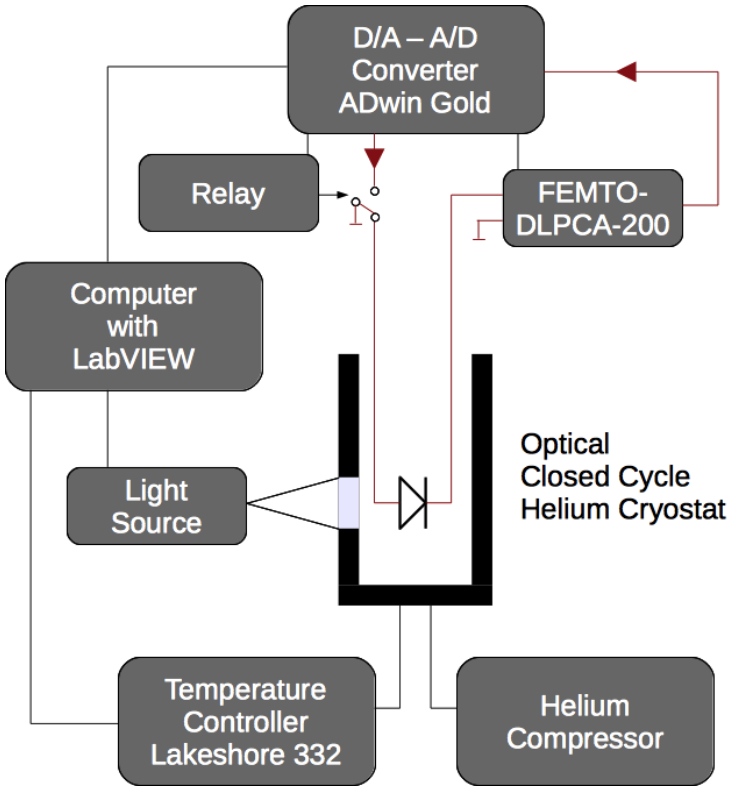

Figure 4.3.: The experimental setup used for current based deep level transient spectroscopy (Q-DLTS).

The transients were recorded in the temperature range between 62 K and 306 K in steps of 2 K, starting with the lowest temperature. During the measurements, the compressor of the cryostat was turned off to avoid vibrations and thus noise in the transients. Despite the inactive cooling by the compressor, the heat capacity of the cryostat was sufficient to keep the temperature at a constant value during recording the transient. The standard voltage pulses for the investigated samples were 3 V for 6 s, since for these parameters a saturation of the transients amplitude was observed and an increase of the pulse level or time did not result in further changes in the transients.

4.2.3. Current-Voltage Characterization

To pre-characterize the samples, initial current-voltage measurements were performed in the nitrogen glovebox, using a *Keithley 237* Source Measure Unit. In the case of solar cells also illuminated IV–curves were recorded to investigate the solar cell parameters, namely short-circuit current, open-circuit voltage, fill factor and power conversion efficiency. Therefore, the solar cells were illuminated using an Oriel 81160 AM1.5G solar simulator. The light intensity of the solar simulator was 100 mW/cm^2 corrected by mismatch [127].

In the cryostats IV–curves were recorded by either the *Keithley 237* Source Measure Unit or the *Keithley 6430* Sub-Femtoamp Remote Source Meter. For illumination the 10 W high power white light emitting diode (*Seoul*) was used, with the light intensities adjusted to match the short-circuit current of the cells, obtained under the solar simulator in the glovebox.

5. Trap States in Poly(3-Hexylthiophene) and the Influence of Oxygen [1]

5.1. Introduction

Conjugated polymers are of growing interest for application in organic electronic devices such as organic light emitting diodes (OLEDs), field effect transistors (OFETs) and solar cells, due to their low cost processibility from solution. The presence of traps can be critical to the performance of these devices since they reduce the charge carrier mobility, affect the driving voltage, disturb the internal field distribution and reduce the operation stability as well as the electroluminescence efficiency [66]. Concerning the lifetime of the devices, the influence of oxygen-related defect states on the charge transport might be decisive with respect to the long term stability.

In the following the trap distribution in poly(3-hexylthiophene) (P3HT) is investigated by fractional thermally stimulated current technique. Furthermore, TSC and DLTS measurements are performed to examine the influence of oxygen on the trap states. Additionally, the impact of oxygen induced defects on the charge carrier mobility is studied using photo generated charge extraction by linearly increasing voltage (photo-CELIV) measurements.

5.2. Experimental Details

Diodes with the sandwich structure ITO/PEDOT:PSS/P3HT/(Ca)/Al were fabricated in nitrogen atmosphere. P3HT was spincoated on PEDOT:PSS covered ITO glass substrates from chlorobenzene solution. Two batches of P3HT from Rieke Metals, Inc. were investigated: P3HT 4002E and Sepiolid P200. The active areas of the samples were about 9 mm^2 for TSC and 3 mm^2 for DLTS and CELIV measurements. The Al electrode thicknesses were about 100 nm, in cases where Ca interlayers were used the thicknesses of these were about 2 nm.

TSC, DLTS and photo-CELIV [59, 61] measurements were performed in a closed cycle cryostat with Helium as contact gas. The details of the TSC and DLTS measurements are described in Section 4.2. Photo-CELIV measurements were performed at 300 K. A N_2 laser with dye unit (λ = 500 nm) was used to generate charge carriers, which were then extracted by a linearly increasing reverse bias pulse. The delay time between the laser flash and the triangular bias pulse was 30 μs and 80 μs. The peak voltage in reverse direction was V_a=2 V applied on the Al electrode, with varied offset bias V_{off} in forward direction. Pulse widths of t_p=100 μs and t_p=500 μs were chosen.

Degradation of the samples was always performed at 300 K in the dark.

[1] Parts of this Chapter are published in J. Schafferhans et al., *Trap distribution and the impact of oxygen-induced traps on the charge transport in poly(3-hexylthiophene)*, Applied Physics Letters, 93 (2008), 093303.

5.3. Results and Discussion

5.3.1. Experimental Results

TSC measurements

The TSC spectrum of a P3HT 4002E diode is shown in Figure 5.1a (black curve). A TSC peak between about 25 K and 130 K was detected in good agreement with the TSC measurements by Nikitenko et al. [104], but unlike their results no additional TSC peak was observed up to room temperature. Due to the quite broad TSC peak, a distribution of trap states instead of a discrete trap level can be anticipated. To gain information on the trap distribution TSC $T_{Start} - T_{Stop}$ measurements were applied, as described in Section 3.2.3, with T_{Stop} varied between 40 K and 105 K in steps of 5 K. The main runs for the different T_{Stop} are shown in Figure 5.1a. The sample exhibited a good stability without any aging effects during fractional TSC measurements, as is revealed by the fact that the main runs for the different T_{Stop} finally merge perfectly into the conventional TSC spectrum measured before the fractional TSC (Figure 5.1a, black curve). Additionally, a second conventional TSC measurement was performed after the fractional TSC,

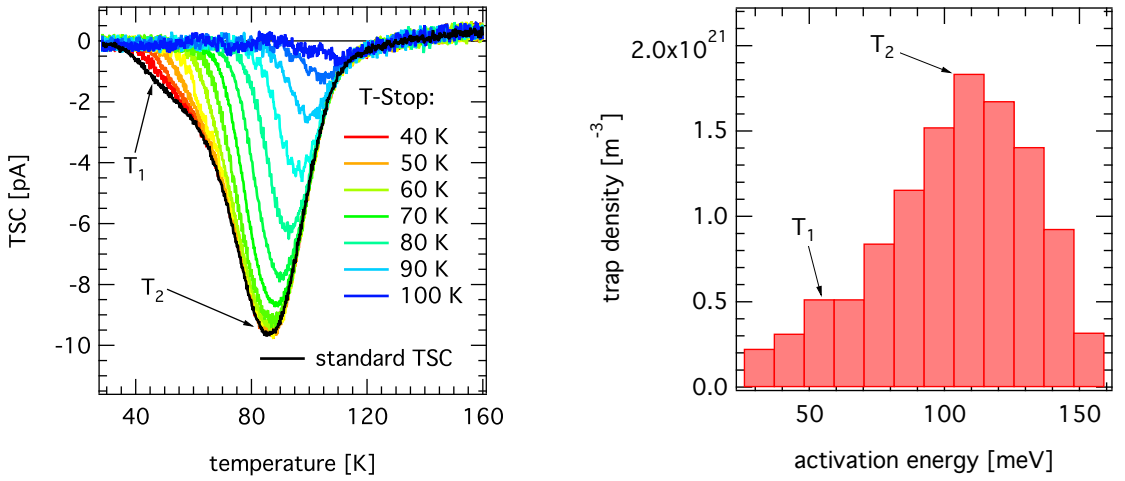

Figure 5.1.: Main runs of the different T_{Start}- T_{Stop} cycles, as well as the conventional TSC spectrum of P3HT 4002E (sample thickness about 220 nm) , revealing two trap states T_1 and T_2 (a) and the resulting DOOS distribution (b).

almost identical to the first run. The standard TSC exhibits a main TSC peak at about 85 K (T_2) as well as a shoulder at about 50 K (T_1), indicating two different trap distributions. In the fractional TSC spectrum the shoulder decreases for increasing T_{Stop} due to the emptying of the shallower traps during the prerelease; it disappears for T_{Stop} larger than 60 K. According to Equation 3.8 the activation energies E_t of the traps can be estimated for each T_{Stop} interval from the initial rise of the respective main run. Hence, the activation energies for the T_{Stop} intervals from 40 K to 95 K were determined from the Arrhenius plot in the initial rise, whereas the signal-to-noise ratio was too low for the cycles with T_{Stop} above 95 K. Thereby, a linear increase of the activation energy with temperature was revealed, which has already been reported for

fractional thermally stimulated luminescence measurements on different polymers [62–64, 66, 67]. This continuous increase of the activation energies with temperature without any plateaus indicates a continuous trap distribution instead of discrete trap levels [142], as it was already expected on the basis of the broad TSC spectrum. The lower limit of the total (T_1+T_2) trap density is $n_t = (1.0-1.2) \times 10^{22}$ m^{-3} for the investigated samples. Applying Equation 3.1 to the fractional TSC measurements, the trap densities for each T_{Stop} interval can be estimated. These can be related to the activation energies extracted from the initial rise of the fractional TSC, as shown in Figure 5.1b, yielding a reconstruction of the density of occupied states (DOOS) [124]. The histogram displays a quasi-continuous trap distribution with activation energies between about 25 meV and 160 meV and two maxima at about 50 meV and 105 meV, indicating two different traps (T_1, T_2) with approximately Gaussian energy distributions. This is in accordance with the observed shape of the TSC signal. Due to the low activation energy of a few 10 meV, the trap distribution T_1 can be attributed to the tail states of the regular density of states (DOS). The second deeper trap T_2, however, might result from structural defects, for example amorphous phases or grain boundaries between crystalline phases in the P3HT layer.

To investigate the influence of oxygen and moisture on the trap states, P3HT (4002E) diodes were exposed to ambient air (Figure 5.2a) and dry oxygen (Figure 5.2b).

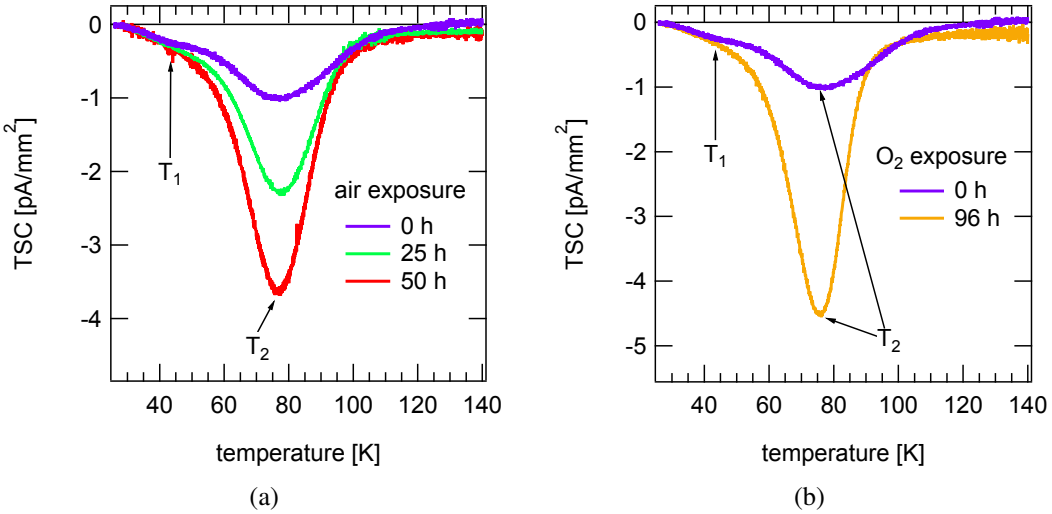

Figure 5.2.: TSC spectra for different exposure times of the P3HT 4002E diodes (sample thicknesses about 220 nm) to ambient air (a) and dry oxygen (b), showing an increase of the trap density of T_2 due to oxygen.

With increasing exposure time, the TSC peak T_2 strongly increases (see Figure 5.2a), signifying a raise of the trap density of the deeper trap. In contrast, the shoulder T_1 in the TSC spectrum of the pristine sample, attributed to the tail states of the intrinsic DOS, is unaffected by the exposure to air. For increasing exposure times, the shoulder seems to vanish as an effect of the overlap with the strongly increasing trap T_2. To distinguish whether the enhanced trap density is due to oxygen or moisture, a sample was exposed to dry oxygen, resulting in the same effect as for the exposure to air (Figure 5.2b). Therefore, the increase of T_2 can be attributed to oxygen instead of moisture. It has to be mentioned that the exposure to air and oxygen did not result in any additional TSC peaks up to room temperature. The lower limits of the total trap

densities for different exposure times are summarized in Table 5.1. After an exposure of 50 h to air, the trap density yields $n_t = 2.6 \times 10^{22}$ m^{-3}, which is more than a factor of two higher as in the pristine samples.

Sample	Trap density [m^{-3}]
Pristine	1.0×10^{22}
25 h exposed to air	1.7×10^{22}
50 h exposed to air	2.6×10^{22}
96 h exposed to O_2	2.8×10^{22}

Table 5.1.: Lower limit of the total trap densities obtained from the TSC measurements for different exposure times of the P3HT 4002E samples to air and dry oxygen.

The TSC spectrum of a pristine P3HT Sepiolid P200 sample is shown in Figure 5.3a (red line). Despite the slightly higher regioregularity, the sample exhibits the same two trap distributions T_1 and T_2 as in the case of P3HT 4002E. Also for this batch, the lower limit of the trap density is in the range of $n_t = (1.0 - 1.2) \times 10^{22}$ m^{-3} for the investigated samples. Exposure of the samples to synthetic air (80 % N_2, 20 % O_2, < 1 ppm H_2O) results in an increase of the deeper traps density due to oxygen (Figure 5.3a), in the same manner as for P3HT 4002E.

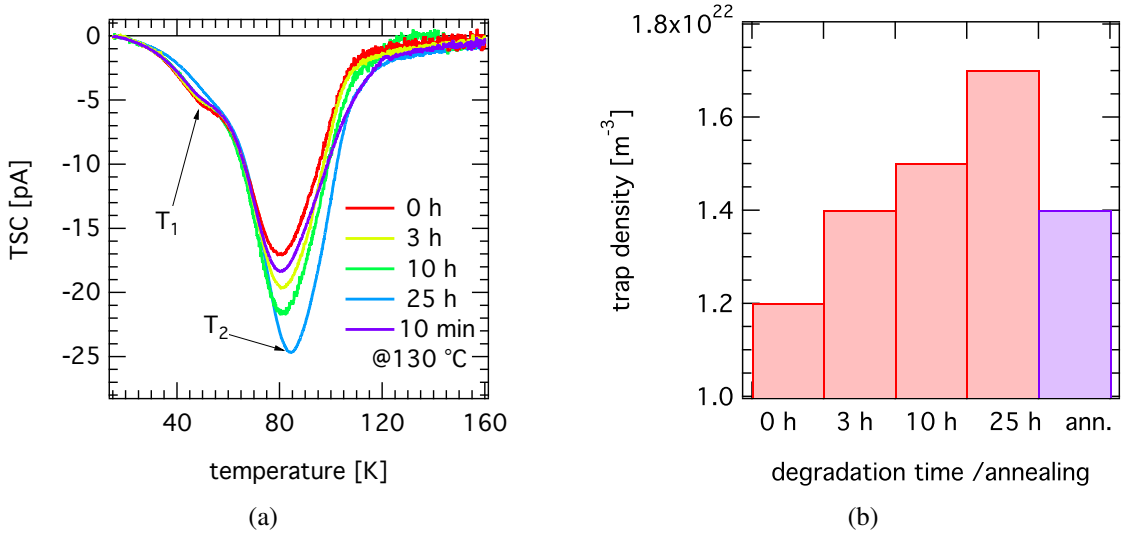

Figure 5.3.: TSC spectra for different exposure times of a P3HT Sepiolid P200 diode (sample thickness about 330 nm) to synthetic air and after annealing of the sample for 10 min at 130 °C in nitrogen atmosphere (a) and the corresponding lower limits of the trap density (b). The increase of the trap density of T_2 due to oxygen is partially reversible by applying a thermal treatment to the sample.

Applying a thermal treatment to the sample (10 min at 130 °C in nitrogen atmosphere) decreases the concentration of T_2, exhibiting a partial reversibility of the oxygen induced defects. The corresponding lower limits of the trap densities (T_1+T_2) are summarized in Figure 5.3b. A

reversibility of the oxygen induced defects could also be achieved by storing the sample in vacuum for several hours (data not shown). However, the reversibility was considerably enhanced and accelerated by the thermal treatment. Furthermore, it should be noted that the observed degradation was independent of the used top electrode materials, i.e. Ca/Al or Al.

DLTS measurements

Q-DLTS measurements on a P3HT (Sepiolid P200) diode (sample thickness about 190 nm) were performed using the standard parameters described in Section 4.2.2. The current transients were analyzed with the Tikhonov regularization method using FTIKREG. The resulting emission rate distributions for different degradation times of the sample in synthetic air (0 h, 1 h, 3 h, 10 h and 30 h) are shown in Figure 5.4 as Arrhenius plots. The colors of the contour plots represent the logarithmic density of the traps contributing to the respective emission rate intervals. The plots exhibit several emission rate bands, each of them with an emission rate distribution due to an energetic distribution of the corresponding traps. The maximal amplitudes of the emission rate distributions (i.e. the corresponding trap densities) are in the range of 10^{21}-10^{22} m^{-3}. To obtain the activation energies of the trap states, the maxima of the emission rate bands were plotted logarithmically over 1/T and fitted linearly (Figure 5.4 (right hand side)).

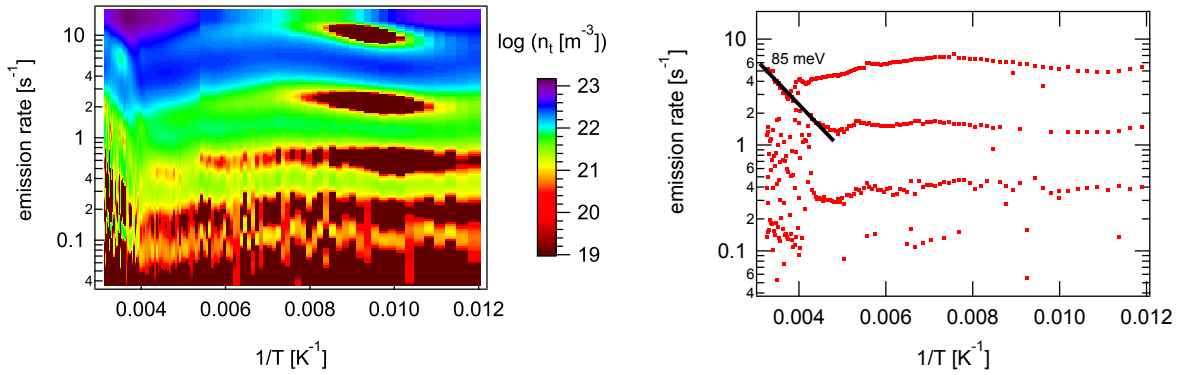

(a) Exposure time to synthetic air: 0 h

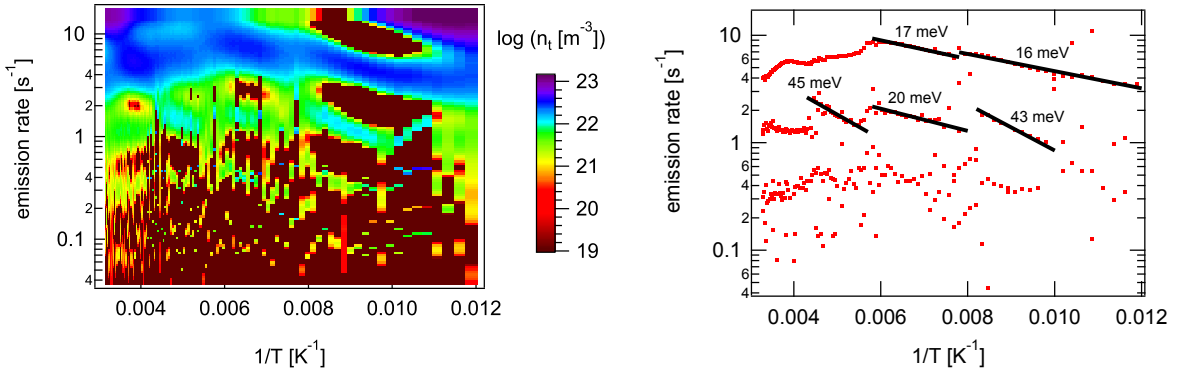

(b) Exposure time to synthetic air: 1 h

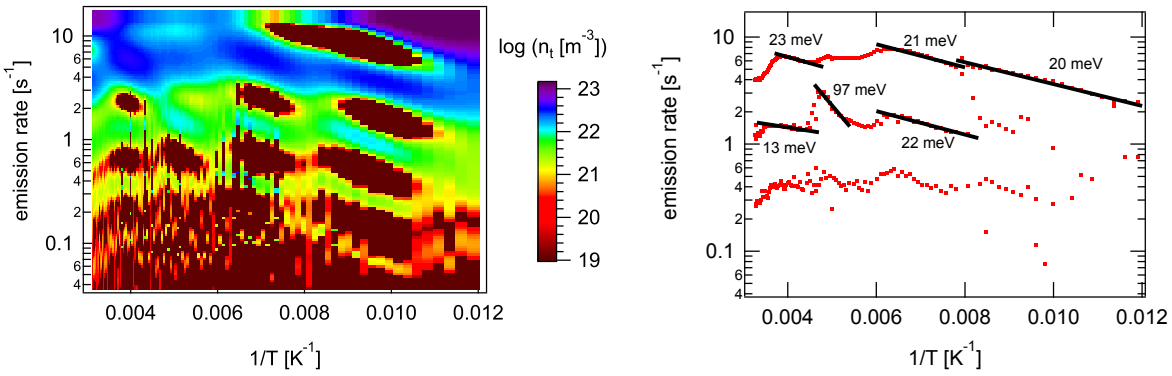

(c) Exposure time to synthetic air: 3 h

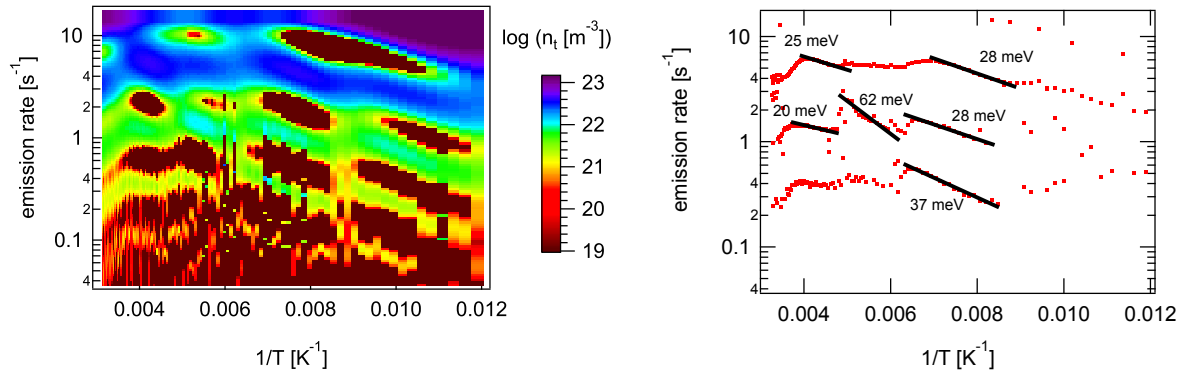

(d) Exposure time to synthetic air: 10 h

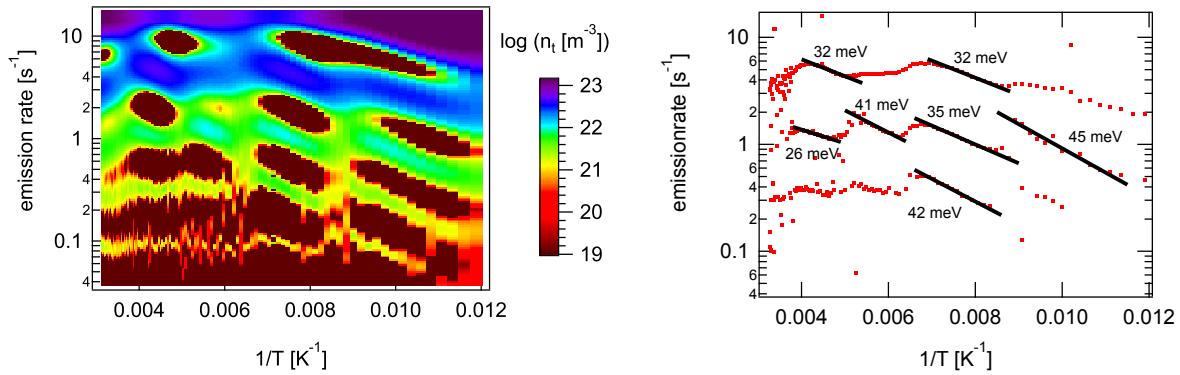

(e) Exposure time to synthetic air: 30 h

Figure 5.4.: Arrhenius plot of the emission rate spectra of a P3HT (Sepiolid P200) diode for different degradation times in synthetic air obtained by analyzing the current transients of the DLTS measurements with FTIKREG (left hand side). The colors represent the logarithmic density of traps contributing to the respective emission rate intervals. Right hand side: The maxima of the emission rate bands which were fitted linearly to obtain the activation energies.

In the case of the non degraded sample, the emission rates are almost temperature independent in a large temperature range. Only at high temperatures of about 220 K–306 K an activation energy of 85 meV can be obtained. With increasing degradation time the emission

rate bands get more pronounced and temperature dependent and several activation energies between about 13 meV and 97 meV can be identified in the temperature range of 80 K–306 K. The activation energies and the corresponding normalized trap densities (i.e. the amplitude maxima of the respective emission rates divided by the maximal occurring amplitude) for the different degradation times are summarized in Figure 5.5.

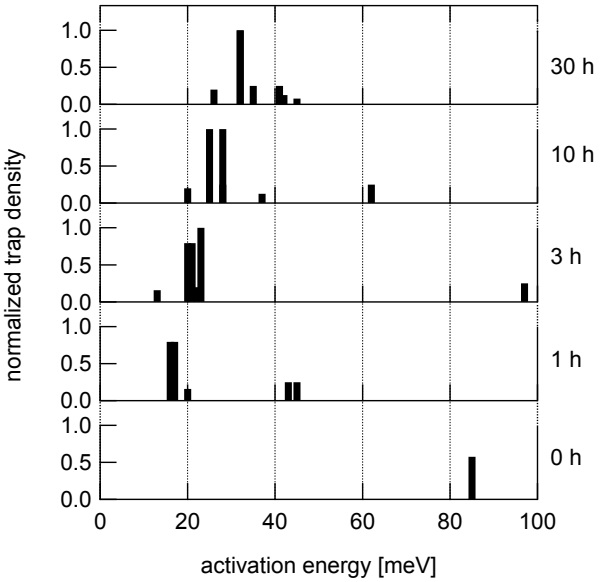

Figure 5.5.: Summary of the obtained activation energies of the P3HT diode for different degradation times in synthetic air by DLTS measurements. The height of the bars represent the relative maximum amplitude of the corresponding emission rate distribution.

For 1 h exposure to synthetic air, the dominant emission rates yield activation energies of about 20 meV. With increasing degradation time the activation energies and the densities of the dominant traps rise due to oxygen, in qualitative good agreement with the increase of the deeper traps density revealed by TSC measurements. However, the activation energies obtained by DLTS are lower than those from TSC. The difference might result from the neglected temperature dependences of the attempt-to-escape frequency and the transport energy. In the case of fractional TSC measurements, only a small temperature range in the initial rise of each TSC cycle is used to obtain the activation energy and neglecting the temperature dependences of the attempt-to-escape frequency and the transport energy is thus uncritical. Instead, in the case of DLTS measurements, the activation energies are obtained from a much larger temperature range and thus the results are more affected by neglecting the these temperature dependences.

Photo-CELIV measurements

To investigate the impact of the oxygen induced traps on the charge carrier mobility, photo-CELIV measurements were performed. Therefore, the samples were also exposed to synthetic air for several hours as in the TSC and DLTS measurements. In Figure 5.6 exemplary photo-CELIV measurements on a P3HT sample for different exposure times are shown. The mobility

was calculated from the position of the CELIV peak maximum according to [59].

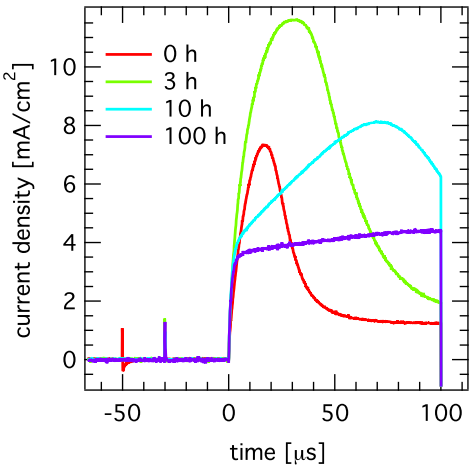

Figure 5.6.: Exemplary photo-CELIV measurements ($V_{off} = -1.4\ V$, $t_p = 100\ \mu s$), showing the shift of the CELIV peak maximum to longer times with increasing exposure time of the sample to synthetic air due to a decrease of the charge carrier mobility.

From Figure 5.6 it can be seen that with increasing exposure time, the CELIV peak shifts to longer times due to a lower charge carrier mobility. The measured mobilities for the different exposure times of the sample to synthetic air are summarized in Table 5.2. After 100 h in air, the mobility decreased about two orders of magnitude compared to the pristine sample. This effect can be correlated to the strong increase of the trap density revealed by the TSC and DLTS measurements.

Sample	Mobility [cm^2/Vs] V_{off}= -1.4 V [a]	Mobility [cm^2/Vs] V_{off}= -0.4 V
Pristine	2.5×10^{-6}	1.2×10^{-4}
3 h exposed to air	5.2×10^{-7}	2.6×10^{-5}
10 h exposed to air	1.2×10^{-7}	4.9×10^{-6}
100 h exposed to air	5.4×10^{-8}	— [b]

[a] Underestimated mobility, due to high RC constant

[b] No estimation possible, due to low signal

Table 5.2.: Charge carrier mobility obtained from the photo-CELIV measurements for different exposure times of the sample to air and different offset voltages applied.

5.3.2. Discussion

The observed increased trap density in P3HT after oxygen exposure can be attributed to oxygen diffusion into the bulk of the diode. The oxygen diffusion constant in P3HT was determined by Lüer et al. [85] to be 1.5×10^{-7} cm^2/s. Therefore, the timescale needed for oxygen to penetrate the whole active area of the P3HT diodes is within several hours for the investigated device structures, if the oxygen enters the device only from the unprotected sides, i.e. the areas not covered by the top electrode. This is in agreement with the timescales used for the degradation measurements. However, oxygen also might enter the device via pinholes within the top electrode.

Abdou et al. [1] showed that oxygen forms a charge transfer complex with P3HT, resulting in p-doping of P3HT, which was also investigated theoretically by band-structure calculations [84]. The formation of the charge transfer complex results in an increased fluorescence quenching in P3HT [1, 85]. p-doping of P3HT due to oxygen is also reported for organic field effect transistors [1, 51, 81, 83, 92] resulting in increased source-drain currents and conductivities [1, 51, 83]. Furthermore, decreased mobilities in oxygen exposed P3HT field effect transistors are reported [1, 51], which is in agreement with the here observed mobility loss in the P3HT diodes with increasing oxygen exposure time, as revealed by photo-CELIV measurements. The decreased mobilities in the P3HT OFETs were attributed to an increase of scattering centers. However, the increased trap density due to oxygen, revealed by TSC and DLTS measurements in this work, suggests that the decreased mobility is caused by oxygen induced traps.

Increased trap densities after oxygen exposure were also observed in PPV diodes [137] and attributed to physically adsorbed oxygen, forming electron traps. However in the measurements performed here, it can not be distinguished whether the oxygen induced defects are hole or electron traps. Although the p-doping of P3HT is due to an electron transfer from the polymer to oxygen and thus oxygen acts as electron trap, the negatively charged oxygen might also influence the HOMO levels of P3HT in its vicinity due to Coulomb interaction, resulting in an increased energetic disorder. This would also enhance the trap density for holes. The influence of doping on disordered organic semiconductors was calculated analytically by Arkhipov et al. [9], showing that doping indeed leads to an increase of trap states due to Coulomb interaction of ionized dopants with charge carriers of opposite sign. Due to the activation energy of T_2 of only 105 meV and the presence of these traps also in non aged samples—although less pronounced—their origin is probably in this enhanced energetic disorder. Thus, the detected trap states T_2 can be assigned more likely to holes than to trapped electrons on oxygen.

The doping of P3HT due to oxygen is reported to be (partially) reversible after applying vacuum to the sample [1, 81, 83, 85]. However the reversibility is improved and accelerated by a thermal treatment of the devices [81, 83], which is explained by an enhanced chain motion of P3HT due to the higher temperature resulting in an improved release of oxygen. These investigations are in accordance with the here observed partial reversibility of the oxygen induced defects by applying a vacuum or thermal annealing step to the samples, with the latter being more effective. The reversibility of the oxygen induced traps is also reported for PPV [137].

Furthermore, it should be noted that the lower limit of the trap concentration in the investigated samples of 10^{22} m^{-3} is within the same range as the charge carrier densities in OLEDs and operating organic solar cells [118, 128, 135]. Therefore, an impact of the oxygen induced defect states on the luminescence efficiency of OLEDs and the performance of organic solar cells can be expected.

5.4. Conclusions

In summary, the trap distribution in P3HT was investigated by fractional thermally stimulated current measurements. Two different trap states were revealed, with activation energies of 50 meV and 105 meV and Gaussian energy distributions. The first can be assigned to the tail states of the intrinsic DOS due to their low activation energy. The second, however, is strongly influenced by exposure to oxygen. The lower limit of the total trap density yields $n_t = 1.0 \times 10^{22}$ m^{-3} for the pristine sample, which rises up to 2.6×10^{22} m^{-3} after an exposure to air for 50 h. An increased trap density due to oxygen is also found by DLTS measurements. As revealed by photo-CELIV measurements, the charge carrier mobility in P3HT decreases about two orders of magnitude after an exposure to air for 100 h due to the strong rise of the deeper traps density. Furthermore it was shown that the increased trap density due to oxygen exposure is partially reversible by thermal treatment of the devices in nitrogen atmosphere or by vacuum, with the former being more efficient.

6. Electronic Trap States in Methanofullerenes [1]

6.1. Introduction

Methanofullerenes are the most commonly used electron acceptors in organic bulk heterojunction solar cells [27]. The first use of fullerene and its derivatives in organic photovoltaics (OPV) was introduced in [121, 149]. Since that, the methanofullerenes became the main type of acceptors in OPV. Also in the current record organic solar cell with efficiency of 8.3 % [41] a methanofullerene is used as acceptor. The advantages of methanofullerenes are that they can be easily processed from solution, possess high electron affinities and form segregated phases in blends with common donor polymers. Furthermore the used methanofullerenes yield good electron mobilities. For example, space–charge limited current mobilities for electrons of 2×10^{-3} cm^2/Vs in $PC_{61}BM$ diode structures are reported [94].

To further enhance the power conversion efficiencies of organic solar cells, a recent approach is to use multiple adduct fullerene derivatives [47, 77] such as bis$PC_{61}BM$. Multiple side chains on the fullerene cage lead to an increase of the lowest unoccupied molecular orbital resulting in a raise of the open-circuit voltage.

Despite the importance of methanofullerenes, little attention was paid to thin films of the pure materials except the mobility measurements in n-type [130, 148] or ambipolar [2, 3] transistors and methanofullerene diodes [77, 94].

Recently, quantum chemical and voltammetric studies have been performed for $PC_{61}BM$ and its higher fullerene adducts [38], revealing a variety of HOMO and LUMO energies for the adducts with multiple side chains, due to the different isomers they consist of.

Lenes et al. [76] investigated electron–only devices based on fullerene derivatives and a variety of their bisadducts blended with poly(3-hexylthiophene) by current–voltage measurements. The lower currents of the devices with bisadducts were attributed to shallow trapping. This conclusion was supported by device simulations introducing a distribution of traps, which enabled to fit the current–voltage curves.

Although trap states can have a significant influence on the performance of organic solar cells, as they can act as recombination centers, lower the mobility and disturb the internal field distribution, direct identification of the trap states in methanofullerene films has not been performed so far.

In this chapter, the trap states in three commonly used fullerene derivatives, namely $PC_{61}BM$, $PC_{71}BM$ and bis$PC_{61}BM$, are investigated by thermally stimulated current measurements.

[1] The results of this Chapter are published in J. Schafferhans et al., *Electronic Trap States in Methanofullerenes*, Advanced Energy Materials (2011), doi: 10.1002/aenm.201100175.

6.2. Experimental Details

To investigate the trap states in the fullerene derivatives $PC_{61}BM$ ([6,6]-phenyl C61 butyric acid methyl ester) (purity 99.5 %), $bisPC_{61}BM$ (bis[6,6]-phenyl C61 butyric acid methyl ester) (purity 99.5 %) and $PC_{71}BM$ ([6,6]-phenyl C71 butyric acid methyl ester) (purity 99 %), planar diode structures were used, prepared on structured indium tin oxide (ITO)/glass substrates covered with PEDOT:PSS, as described in Section 4.1. The fullerene derivatives were spin coated from chloroform solution ($PC_{61}BM$: 30 mg/ml 600 rpm, $bisPC_{61}BM$ and $PC_{71}BM$: 20 mg/ml 800 rpm). The layer thicknesses were about 200 nm. LiF (1 nm)/Al (120 nm) was used as top contacts.

Initial current–voltage (IV) characteristics were measured in the nitrogen glovebox. Thermally stimulated current (TSC) measurements were performed in a closed cycle cryostat with Helium as contact gas. Via an integrated lock, the samples were transferred from the glovebox to the cryostat, avoiding potential degradation of the samples due to air exposure. Trap filling was achieved by illumination of the samples at 18 K for five minutes using a 10 W high power white light emitting diode. After a dwell time of five minutes the temperature was increased with a constant heating rate of 6.9 K/min up to 300 K.

6.3. Results and Discussion

6.3.1. Experimental Results

The current–voltage characteristics of the investigated samples are shown in Figure 6.1. The device currents in forward bias of $bisPC_{61}BM$ and $PC_{71}BM$ are lower compared to $PC_{61}BM$, with the lowest current for $bisPC_{61}BM$.

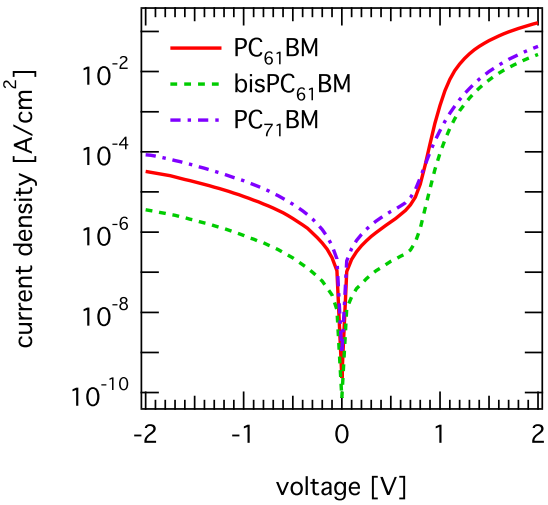

Figure 6.1.: Dark IV–curves of $PC_{61}BM$, $bisPC_{61}BM$ and $PC_{71}BM$ diodes at room temperature. The diode structures were ITO/PEDOT:PSS/PCBM/LiF/Al and the thicknesses of all methanofullerene layers were about 200 nm.

The TSC spectrum of the $PC_{61}BM$ sample is shown in Figure 6.2 (black line). TSC behavior

is observed between 18 K and 160 K with the maximum at about 55 K. No additional TSC peak can be detected at higher temperatures up to room temperature. Already at 18 K a small current of about 0.5 pA can be measured, indicating a release of trapped charge carriers. In addition to the maximum of the TSC spectrum at 55 K, small shoulders can be seen on the low temperature side (at about 25 K) as well as on the high temperature side (at about 90 K). The shape of the TSC spectrum indicates a trap distribution instead of discrete trap levels. According to Equation 3.1 a lower limit of trap density can be obtained by integrating the TSC spectrum over the time, yielding $n_t \geq 1.7 \times 10^{22}$ m^{-3}.

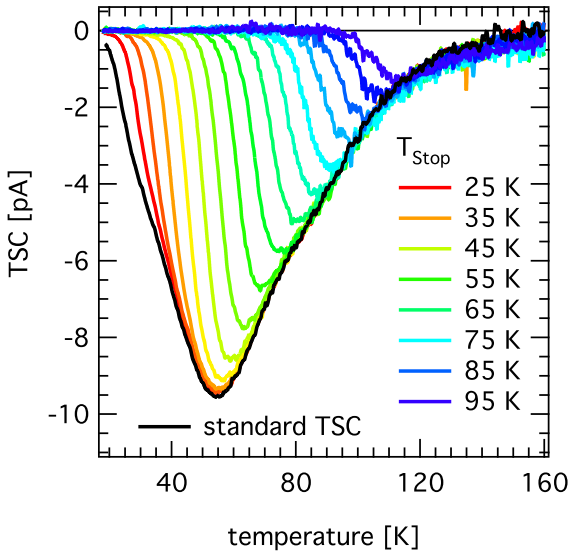

Figure 6.2.: Standard TSC spectrum of $PC_{61}BM$ (black line) as well as the main runs of the T_{Start}–T_{Stop} method for different T_{Stop}.

To get further information about the trap distribution fractional TSC measurements, the so called T_{Start}–T_{Stop} method (as described in Section 3.2.3) were applied, with T_{Stop} varied between 25 K and 120 K in steps of 5 K. Afterwards, a standard TSC spectrum was recorded again, to ensure that no degradation of the sample during the measurements occurred. This TSC spectrum (not shown) is identical to the initial measurement. Therefore, a degradation of the sample during the T_{Start}–T_{Stop} cycles can be excluded. The main runs of the fractional TSC measurements for different T_{Stop} are shown in Figure 6.2. The shoulder at low temperatures becomes less pronounced for increasing T_{Stop} due to emptying of the shallower traps during the prerelease and disappears for $T_{Stop} > 35$ K. The height and position of the main peak is unaffected by the prerelease up to 40 K. For higher T_{Stop} the peak maximum of the TSC decreases and shifts to higher temperatures. The maximum position of the TSC (T_{max}) is plotted vs T_{Stop} in Figure 6.3a (triangles), showing a linear dependence for $T_{Stop} > 40$ K of slope ~ 1. As described in Section 3.2.3 a discrete trap level, in contrast, would result in a constant maximum temperature and a series of trap levels, with well separated TSC peaks, would result in a staircase in the T_{max}–T_{Stop} plot, with a flat region in the plot for each trap level. The closer are the trap levels and the more the TSC peaks overlap, the smoother becomes the staircase. A linear dependence of T_{max} on T_{Stop}, as seen in Figure 6.3a, is due to closely overlapping or a quasi-continuous distribution of TSC peaks [89, 90] and reflects a quasi-continuous distribution of

trap states in $PC_{61}BM$. With increasing T_{Stop} the shallower traps get emptied and the influence of the deeper trap states on the TSC peak becomes stronger, resulting in a shift of the maximum to higher temperatures.

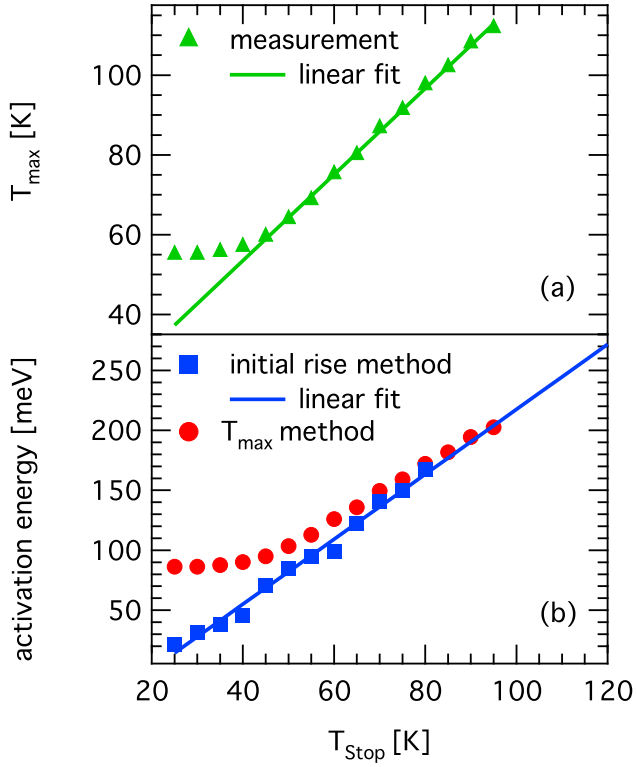

Figure 6.3.: (a) Temperature of the TSC peak maximum of $PC_{61}BM$ for different T_{Stop} in the fractional TSC (triangles). The linear dependence of T_{max} on T_{Stop} (for $T_{Stop} >$ 40 K) of slope $\sim$ 1 (line) indicates a quasi-continuous distribution of traps. (b) Activation energies of the trap states in $PC_{61}BM$ according to the initial rise method (Equation 3.8) for the different values of T_{Stop} (squares) and the linear fit of the activation energies (line). For comparison the activation energies obtained by the T_{max} method (Equation 6.1) are also shown (circles).

The activation energies E_t can be estimated from the exponential initial rise of the fractional TSC measurements for each T_{Stop} (Equation 3.8). Hence, the activation energies for $T_{Stop} \leq 80$ K were determined from the Arrhenius plot, whereas the signal-to-noise ratio was too low for the cycles with T_{Stop} above 80 K. The advantage of the initial rise method is that it can be applied without further knowledge of the kinetics of the TSC (i.e. if there is slow or fast retrapping of the charge carriers) [103]. The obtained activation energies are shown in Figure 6.3b (squares). They show a good linear dependence on T_{Stop}, therefore, the activation energies were linearly extrapolated to estimate them in the range of $T_{Stop} > 80$ K.

Applying Equation 3.1 to fractional TSC measurements, the trap densities for each T_{Stop} interval can be estimated. These can be related to the activation energies extracted from the initial rise, as shown in Figure 6.4, yielding a reconstruction of the density of occupied states (DOOS) as described in Section 3.2.3. The histogram displays a broad trap distribution ranging from 15 meV to 270 meV with the maximum at about 75 meV.

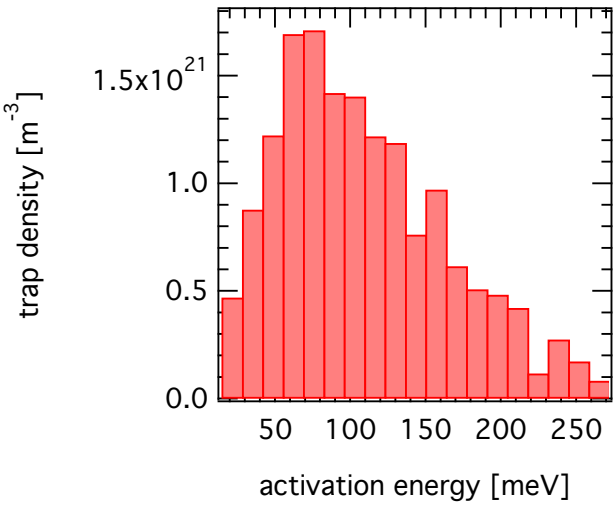

Figure 6.4.: DOOS distribution of $PC_{61}BM$, as obtained by TSC T_{Start}–T_{Stop} measurements.

The activation energy of the most prominent trap can also be approximately calculated using [34]:

$$E_t = k_B T_{max} \ln\left(\frac{T_{max}^4}{b}\right) \quad . \tag{6.1}$$

Here, b is the heating rate used in the TSC measurements. This method (in the following called T_{max} method) has also been used to estimate the activation energies of trap states in P3HT:$PC_{61}BM$ solar cells [68] and C_{60} field effect transistors [88]. The advantage of this method is that no time consuming fractional measurements are needed. However, it only gives an approximation of the dominating trap states, since otherwise distinct TSC maxima are needed. Nevertheless, to compare the trap states of different materials the information about the activation energies of the most prominent traps can be sufficient.

The T_{max} method is a further simplification of the method introduced by Hoogenstraaten [49] (Equation 3.7) for first order kinetics TSC, where a couple of different heating rates is used to obtain the activation energy of the traps. Assuming that the attempt–to–escape frequency is dependent on temperature $\propto T^2$ (as in the case of inorganic semiconductors), Equation 3.7 can be approximately written as Equation 6.1, allowing to determine the activation energy directly from the maximum of the TSC, without varying the heating rate. Because of these intense assumptions, the activation energies of $PC_{61}BM$ estimated by Equation 6.1 first of all are compared with the results of the initial rise method (Equation 3.8). As can be seen from Figure 6.3b, the activation energy obtained with the T_{max} method (circles) remains nearly constant for T_{Stop} < 40 K. This constant value of about 86 meV is caused by the fact that at low T_{Stop} the temperature of the TSC peak maximum does not change, since the dominant traps are not affected by the prerelease, as already mentioned above. Hence, the activation energies obtained by the T_{max} method are overestimated with respect to those from the initial rise method (squares), as the latter are dominated by the shallowest occupied traps. For $T_{Stop} > 40$ K, the activation energy obtained from the T_{max} method rises due to the emptying of the prominent traps and the enhanced contribution of the remaining deeper traps. The difference between both methods diminishes.

By applying Equation 6.1 to a standard (non-fractional) TSC scan one gets the activation energy of the most prominent traps. Therefore, the value of 86 meV (Figure 6.3b) has to be compared to the energy distribution maximum shown in Figure 6.4. It can be concluded that despite all assumptions the T_{max} method is based on, it is a good approximation to gain the activation energy of the dominant trap states in methanofullerenes.

In addition to the investigations of $PC_{61}BM$, TSC measurements on $bisPC_{61}BM$ and $PC_{71}BM$ were performed. The spectra are shown in Figure 6.5, with $PC_{61}BM$ for comparison. Both, $bisPC_{61}BM$ and $PC_{71}BM$, yield an even broader TSC spectrum than $PC_{61}BM$, implying a broader trap distribution and higher activation energies. For $bisPC_{61}BM$ two distinct maxima can be seen in the TSC spectrum, one at about 32 K and the dominant one at about 103 K, as well as a shoulder at about 160 K, indicating at least three different trap levels. $PC_{71}BM$ yields two maxima with almost the same height at about 60 K and 120 K.

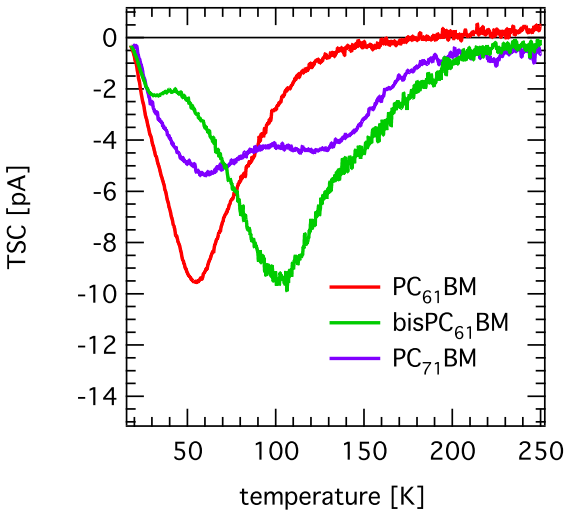

Figure 6.5.: TSC spectra of $PC_{61}BM$, $bisPC_{61}BM$ and $PC_{71}BM$.

To give an estimation of the activation energies of the traps in $bisPC_{61}BM$ and $PC_{71}BM$, the T_{max} method according to Equation 6.1 was used. The resulting activation energies of the distinct traps (the shoulder of $bisPC_{61}BM$ is neglected), the corresponding temperatures of the TSC maxima, as well as the lower limits of the total trap densities are summarized in Table 6.1.

6.3.2. Discussion

As summarized in Table 6.1, $bisPC_{61}BM$ exhibits a trap density of $n_t \geq 2.3\times10^{22}$ m^{-3} which is about 35 % higher than the value obtained for $PC_{61}BM$. Also the trap density of $PC_{71}BM$ is higher than the one for $PC_{61}BM$. However, one has to bear in mind that the estimated trap densities are only lower limits.

Furthermore, the three fullerene derivatives feature very different TSC spectra (Figure 6.5). $BisPC_{61}BM$ yields a much broader TSC spectrum than $PC_{61}BM$. The small TSC peak of $bisPC_{61}BM$ at about 32 K with corresponding activation energy of the traps of 45 meV is in good agreement with the low temperature shoulder of $PC_{61}BM$; it has therefore probably the same origin. However, the most prominent trap in $bisPC_{61}BM$ exhibits an activation energy of

sample	trap density [m^{-3}]	T_{max} [K]	E_t [meV]
$PC_{61}BM$	$\geq 1.7\times10^{22}$	54.9	86
$bisPC_{61}BM$	$\geq 2.3\times10^{22}$	32.4 103	45 184
$PC_{71}BM$	$\geq 2.0\times10^{22}$	60.1 121.4	96 223

Table 6.1.: Lower limit of the trap densities of $PC_{61}BM$, $bisPC_{61}BM$ and $PC_{71}BM$, as well as the temperatures of the TSC maxima and the corresponding activation energies estimated by the T_{max} method according to Equation 6.1. For $bisPC_{61}BM$ and $PC_{71}BM$ E_t and T_{max} values of both peaks are shown.

about 184 meV which is considerably higher than the activation energy of the dominant trap in $PC_{61}BM$ of about 86 meV. The shoulder on the high temperature side of the $bisPC_{61}BM$ TSC peak indicates the presence of a significant amount of even deeper traps. The high activation energies might originate from the mixture of isomers in $bisPC_{61}BM$. The lowest unoccupied molecular orbital energies for the different isomers ranges from -3.71 eV to -3.54 eV [38], introducing a higher energetic disorder–where the lowest lying states may act as traps. Furthermore, due to the additional side chains a close packing of the buckyballs is inhibited, which may result in a higher spatial disorder, also introducing additional traps.

$PC_{71}BM$ yields two distinct peaks in the TSC spectrum. The one at lower temperatures with an activation energy of about 95 meV is quite similar to the main trap of $PC_{61}BM$. The second one yields high trap activation energies of about 223 meV. Similar to $bisPC_{61}BM$, $PC_{71}BM$ also consists of multiple isomers (one major and two minor isomers) [14] which might be the origin of the deep traps. Furthermore, the $PC_{71}BM$ batch has a lower purity grade (>99 %) compared to $PC_{61}BM$ ($\geq$99.5 %) and therefore a higher impurity concentration which can lead to a higher trap density. Another explanation for the higher trap density and the deeper traps compared to $PC_{61}BM$ might be a higher disorder in $PC_{71}BM$ films, due to the spatial anisotropy of C_{70}.

The shapes of the TSC spectra (the shoulders in addition to the main peak) of the three investigated methanofullerenes indicate that the trap distribution of each of the fullerene derivatives consists of at least three peaks. This is affirmed by the fractional TSC measurements on $PC_{61}BM$ yielding a quasi-continuous trap distribution between 15 meV and 270 meV. The TSC peaks of $PC_{71}BM$ and $bisPC_{61}BM$ are even broader compared to $PC_{61}BM$, which is in agreement with the reported higher energetic disorder of $bisPC_{61}BM$ [38, 76].

The higher trap densities as well as the trap activation energies in $bisPC_{61}BM$ and $PC_{71}BM$ compared to $PC_{61}BM$ are consistent with the observed lower currents in forward bias of these devices (Figure 6.1). In the case of $bisPC_{61}BM$ this has also been observed before [76] and was attributed to trapping. However direct measurements of the traps were missing so far.

Due to the high trap densities in the investigated methanofullerenes in the order of 10^{22} m^{-3}, which is in the range of charge carrier densities of operating solar cells [118, 128], a strong influence on the solar cell performance can be expected. Although, $bisPC_{61}BM$ has successfully been used in P3HT:fullerene photovoltaic devices, a reduced photocurrent was observed compared to solar cells using $PC_{61}BM$ as acceptor [33, 76, 77]. Thereby, the reduced photocur-

rent is not due to a lower free polaron generation yield (as might be assumed because of the lower electron affinity of bis$PC_{61}BM$ compared to $PC_{61}BM$). Even a higher charge photogeneration efficiency in the P3HT:bis$PC_{61}BM$ blend was demonstrated by transient absorption spectroscopy [33]. Instead, the loss in short-circuit current was attributed to the significantly lower (about one order of magnitude) electron mobility in bis$PC_{61}BM$ compared to $PC_{61}BM$ [33, 77]. This increases the recombination probability during charge extraction and therefore reduces the photocurrent. The lower mobility of bis$PC_{61}BM$ is in agreement with the measurements presented here, showing a higher trap density and deeper trap states in bis$PC_{61}BM$ compared to $PC_{61}BM$. Furthermore, a slower decay of transient absorption intensity was observed in the blends with bis$PC_{61}BM$ [33]. This was attributed to trapping and detrapping events resulting in a delay in the bimolecular recombination of charges. The measurements presented here reveal the presence of deeper trap states in bis$PC_{61}BM$, leading to a slower release of trapped charges, which is in agreement with the reported reduced recombination dynamics.

As mentioned in Section 2.1, protracted charge carrier decay dynamics, with a charge carrier density dependence larger than order of two, are often reported in organic solar cells [36, 129] and are attributed to trapping of charges. Due to the high trap densities in the methanofullerenes, which are even higher than the trap density of pristine P3HT (Chapter 5), the recombination dynamics should be also significantly influenced by the acceptor, not only by the donor polymer. Because of the higher trap densities and deeper traps in bis$PC_{61}BM$ and $PC_{71}BM$ an even stronger dependence of the charge carrier decay on the charge carrier density in blends with bis$PC_{61}BM$ and $PC_{71}BM$ than in those with $PC_{61}BM$ can be expected.

6.4. Conclusions

The trap states in $PC_{61}BM$, $PC_{71}BM$ and bis$PC_{61}BM$ were investigated by thermally stimulated current measurements. The lower limit of the trap densities for each of the three methanofullerenes yield values in the order of 10^{22} m^{-3} with the highest trap density for bis$PC_{61}BM$ of $n_t \geq 2.3 \times 10^{22}$ m^{-3}. The activation energies of the most prominent traps in $PC_{71}BM$ are 96 meV and 223 meV and 184 meV for bis$PC_{61}BM$. Both reveal significantly deeper traps than $PC_{61}BM$, with an activation energy for the dominant trap of about 86 meV. These findings are consistent with the observed lower device currents in forward bias of the $PC_{71}BM$ and bis$PC_{61}BM$ diodes. Additional fractional TSC measurements on $PC_{61}BM$ revealed a broad quasi-continuous trap distribution instead of discrete trap levels with activation energies ranging from 15 meV to 270 meV.

7. Trap States in P3HT:PC_{61}BM Blends

7.1. Introduction

One of the most intensely investigated organic solar cells are made of P3HT:PC_{61}BM blends, as they were record holder in the efficiencies of organic solar cells for several years yielding values of around 4 % [15]. Furthermore, the materials are also commercially available for quite some time, since P3HT is not protected by patents [15] enabling an excellent supply situation. The first encouraging efficiencies of P3HT:PC_{61}BM solar cells were published in 2002 [123]. This paper was directly followed by reports addressing the influence of annealing on the performance of these solar cells, revealing that the efficiencies are significantly increased by thermal treatment [112]. Annealing of the P3HT:PC_{61}BM blends results in an increased crystallinity of P3HT [32, 122, 139] compared to the untreated devices, improving the optical absorption [32, 79, 139] and the hole mobility [122, 139] and thus leading to a significantly increased short-circuit current [32, 79, 112, 139].

In this chapter the trap distribution of annealed P3HT:PC_{61}BM solar cells is investigated by fractional TSC measurements. Furthermore, TSC and DLTS measurements on pristine and annealed solar cells are compared to investigate the influence of annealing and thus the morphology on the trap states in the blends.

7.2. Experimental Details

To investigate the trap states in P3HT:PC_{61}BM, the blends (weight ratio 1:0.8 and 1:1) were spincoated on PEDOT:PSS covered ITO glass substrates from chlorobenzene solution in nitrogen atmosphere as described in Section 4.1. Afterwards, the samples were either annealed for 10 min at 130 °C to improve the morphology, or left as cast (pristine samples). Al was used as top electrode with thicknesses of about 100 nm.

Initial current–voltage characteristics were measured in the nitrogen glovebox. TSC and DLTS measurements were performed in a closed cycle cryostat with Helium as contact gas, using the standard measurement parameters described in Section 4.2.

7.3. Results and Discussion

The TSC spectrum of an annealed P3HT:PC_{61}BM (ratio 1:1) solar cell is shown in Figure 7.1a (black line). Thermally stimulated current is detected between about 20 K and 160 K with the maximum at about 80 K and a small shoulder at about 25 K. To obtain the trap distribution, $T_{Start} - T_{Stop}$ measurements were performed with T_{Stop} varied between 25 K and 150 K in steps of 5 K (Figure 7.1a). The sample yielded a good stability during the fractional TSC, which was confirmed by a standard TSC measurement applied after the fractional TSC, revealing

an identical TSC peak as in the first run. The resulting density of occupied states (DOOS) distribution of the fractional TSC measurement is shown in Figure 7.1b, as well as the spectra of pure P3HT and PC$_{61}$BM for comparison. The continuous activation energies of the traps in

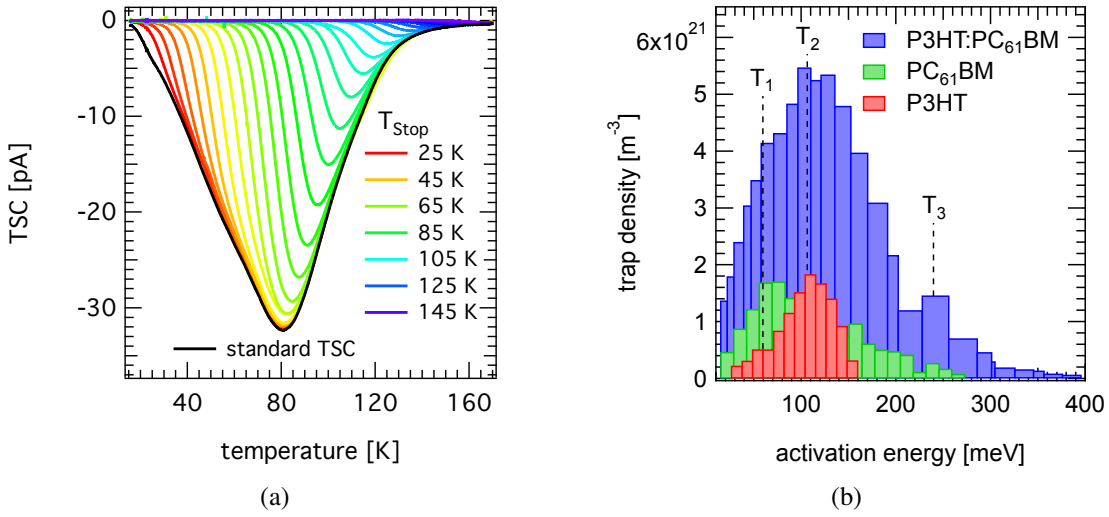

Figure 7.1.: Main runs of the different $T_{Start} - T_{Stop}$ cycles, as well as the conventional TSC spectrum of a P3HT:PC$_{61}$BM (ratio 1:1) solar cell (sample thickness about 230 nm) (a) and the resulting DOOS distribution (b). For comparison the DOOS distributions of P3HT and PC$_{61}$BM are also shown.

the P3HT:PC$_{61}$BM blend range from about 15 meV to 400 meV with the center of distribution at about 105 meV. For further interpretation of the DOOS distribution of the blend, the results for pure P3HT and PC$_{61}$BM have to be considered. For P3HT, the DOOS was related to two different overlapping traps with approximately Gaussian energy distributions (see Chapter 5), with the center of distribution of the dominant trap at about 105 meV (T$_2$) and the other at about 50 meV (T$_1$) (shoulder at the low energy side of the DOOS distribution) (Figure 7.1b). For PC$_{61}$BM a broad trap distribution between about 15 meV and 270 meV and maximum at about 75 meV was detected (Chapter 6). Since the centers of the distributions in the blend and the pure P3HT are at 105 meV, the dominant traps can be attributed to P3HT, overlapped with the traps of PC$_{61}$BM. The steep onset of the DOOS in the blend is in agreement with the onset of the PC$_{61}$BM trap distribution and the trap T$_1$ of P3HT. Additionally, the blend features further trap states with activation energies of 200 meV to 400 meV which are not present in pure P3HT, with the maximum at about 250 meV (T$_3$). Although, in PC$_{61}$BM there are deeper traps up to 270 meV, the blend exhibits significantly more of these and even deeper traps. Therefore, it can be concluded that the DOOS of the blend is an overlap of the traps observed in P3HT and PC$_{61}$BM and additional deeper traps, which can not be clearly assigned to one of the pure materials. These might originate from a higher disorder in the blend and interfaces between the polymer and methanofullerene phases.

The trap densities obtained from the TSC measurements of the investigated P3HT:PC$_{61}$BM solar cells are in the range of $(6-8) \times 10^{22}$ m^{-3} which is considerably higher than the values obtained for P3HT ($(1-1.2) \times 10^{22}$ m^{-3}) (Chapter 5) and PC$_{61}$BM (1.7×10^{22} m^{-3}) (Chapter 6). However, the trap densities received by TSC measurements are only lower limits of the

actual ones, as already pointed out in Section 3.2. The measured higher trap density in the blend might also originate from the higher exciton dissociation yield in the blend and therefore a more efficient trap filling due to a higher amount of charge carriers.

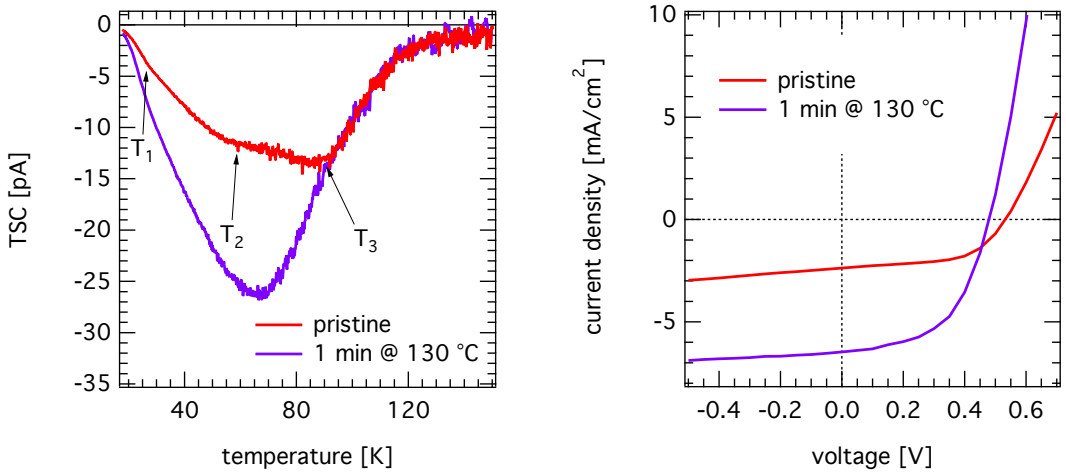

Figure 7.2.: Comparison of the TSC spectra (a) and the illuminated IV-curves (b) of a P3HT:$PC_{61}BM$ (ratio 1:0.8) solar cell (sample thickness about 130 nm) without annealing and after an annealing step of the sample of 1 min at 130 °C.

To investigate the influence of the morphology on the trap states in P3HT:$PC_{61}BM$ blends, standard TSC measurements were performed on a pristine P3HT:$PC_{61}BM$ (1:0.8) solar cell (Figure 7.2a). Afterwards, the sample was annealed at 130 °C for 1 min in nitrogen atmosphere. The TSC spectrum of the sample after the annealing step is also shown in Figure 7.2a. The TSC spectrum of the annealed sample is in agreement with the spectrum shown in Figure 7.1a, although the TSC peak is slightly shifted to lower temperatures. The shift can be attributed to the lower film thickness (130 nm) compared to the sample shown in Figure 7.1a (thickness 230 nm). Since the charge carriers are only extracted by the built-in voltage (given by the work function difference of the electrodes), the lower device thickness implies a higher internal field. This results in a decrease of the effective activation energy of the traps, due to a Poole-Frenkel like effect [37]: the tilt of the transport energy due to the electric field overlaps with the Coulomb potential of the traps resulting in a decrease of the effective energy barrier. The same behavior was also observed for TSC measurements on a PPV derivative, by applying different external voltages during the TSC measurements [141].

However, the TSC spectra of the blend before and after annealing are quite different. The TSC of the pristine sample exhibits three overlapping TSC peaks, whereas after annealing only the shoulder T_1 and the main peak T_2 can be distinguished, which were already attributed to the overlapping trap states of pure P3HT and $PC_{61}BM$. The third peak T_3 can not be directly resolved in the annealed sample, although the shape of the TSC as well as the DOOS distribution (Figure 7.1b) suggest that these traps are also present. Yet, the deep trap states T_3 are the dominant ones in the pristine sample.

As can be seen from Figure 7.2a, the TSC of the pristine sample is lower compared to the one after annealing. This is also reflected in the obtained lower limit of the trap density by integrat-

ing the TSC over time, yielding $n_t \geq 4.6 \times 10^{22}$ m^{-3} for the pristine and $n_t \geq 7.6 \times 10^{22}$ m^{-3} for the annealed sample. However, the lower value for the pristine sample does not imply that the actual trap density is lower, since only the extracted charge carriers contribute to the TSC. The pristine sample yields a higher intermixing of the polymer and fullerene phases, leading to less percolation paths and a higher recombination probability of the charge carriers. This is also revealed in the illuminated IV-curves, shown in Figure 7.2b. The pristine sample exhibits a significantly lower short-circuit current compared to the sample after annealing, due to less extracted charges. Already after annealing the sample for 1 min at 130 °C, the short-circuit current is increased to about 250 % of the initial value. The open-circuit voltage instead slightly decreases, whereas the fill factor remains almost constant. These findings are in accordance with the results of Li et al. [79], who studied the effect of annealing on P3HT:PC_{61}BM solar cells, revealing an increase of the short-circuit current and a slight decrease of the open-circuit voltage upon annealing.

Although it is not possible to draw conclusions about the absolute quantity of the traps in the pristine compared to the annealed sample, it can be concluded that the ratio of the deep traps T_3 to the shallower traps T_1 and T_2 is higher in the case of the pristine sample. This assists the above stated conclusion that the deep traps T_3 are due to the higher disorder in the blend and P3HT/PC_{61}BM interfaces, since in the not annealed device the phases are more intermixed than in the annealed sample.

A further annealing step of the solar cells of 10 min at 130 °C does not result in further changes, neither in the IV-characteristics nor in the TSC spectrum.

The same behavior concerning the influence of annealing on the trap states in the blend is observed in Q-DLTS measurements. In Figure 7.3 exemplary emission rate spectra of a pristine and an annealed (10 min at 130 °C) P3HT:PC_{61}BM (1:0.8) blend is shown (the samples were exposed to synthetic air for 30 h). The DLTS measurements were performed using the standard parameters given in Section 4.2.2 and the emission rates were obtained by analyzing the current transients with FTIKREG. Four emission rate bands (marked with α, β, γ and δ) are detected in both samples in the temperature range between 125 K and 306 K. The trap densities contributing to the respective emission rate intervals are in the order of $10^{21} - 10^{23}$ m^{-3}. The emission rate bands with the stronger temperature dependence (α and β), signifying higher activation

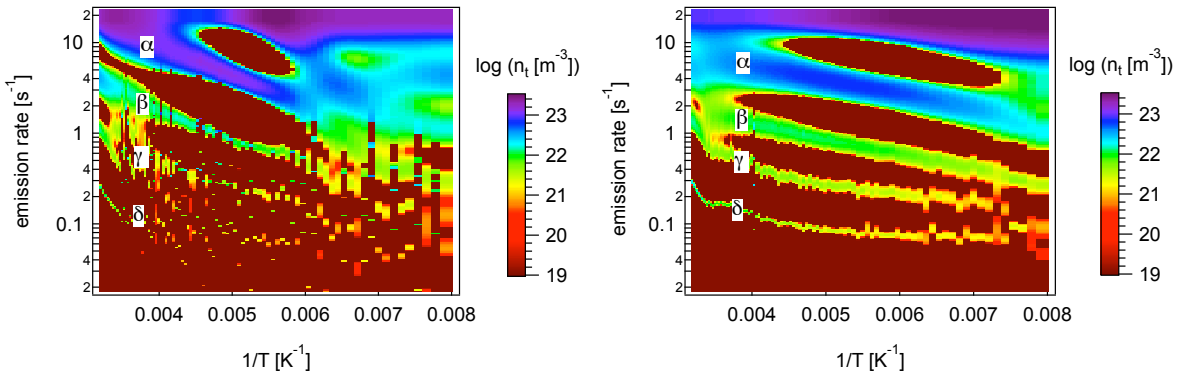

(a) pristine (b) annealed (10 min at 130 °C)

Figure 7.3.: Exemplary emission rate spectra obtained by analyzing the DLTS measurements of a pristine (a) and an annealed (b) P3HT:PC_{61}BM (1:0.8) solar cell with FTIKREG.

energies than γ and δ, are well resolved for the pristine as well as the annealed sample. However, shallower traps contributing to the emission rate bands γ and δ, are less resolved in the pristine sample, yielding significantly lower amplitudes.

Thus, the observations are in accordance to the TSC measurements, exhibiting a higher ratio of the deep to shallow traps in the pristine sample, compared to the annealed one.

The presence of a higher amount of deep traps in the pristine blends will have a significant influence on the charge carrier mobility as well as the recombination dynamics. Indeed, Vanlaeke et al. [139] investigated the influence of annealing on the hole mobility in P3HT:$PC_{61}BM$ blends, showing that the hole mobility is increased by annealing the sample, due to a higher ordering of P3HT. An enhanced hole mobility after annealing was also observed by Savenije et al. [122], by performing time-resolved microwave conductivity measurements. Furthermore, Clarke et al. [22] compared the bimolecular recombination dynamics of pristine and annealed P3HT:$PC_{61}BM$ blends by transient absorption measurements, revealing a slower transient absorption decay for pristine samples. This was attributed to deeper traps in the pristine sample, compared to the annealed one and the authors suggested that these deeper traps originate from structural/conformational defects. However, direct measurements of the trap states were not performed until now.

All these reports are in agreement with the results presented here, showing a higher ratio of the deeper traps in the pristine blend and the attribution of these traps to an enhanced disorder in the blend and more P3HT/$PC_{61}BM$ interfaces. Furthermore, this attribution is also in accordance with the observation that these traps are also present—but less pronounced—in the annealed sample.

7.4. Conclusions

The trap distribution in an annealed P3HT:$PC_{61}BM$ solar cell was investigated by fractional TSC measurements, revealing a broad trap distribution between about 15 meV and 400 meV with the maximum at about 105 meV. Comparing the trap distribution of the blend with those of pure P3HT and $PC_{61}BM$ showed a good agreement of the DOOS maximum with that of P3HT. The steep onset of the distribution in the blend at lower activation energies coincides with the trap distribution in $PC_{61}BM$ overlapped with the shallow traps in P3HT. However, in the blend there are additional deeper traps of about 250 meV to 400 meV which can not be related to the pure materials and were attributed to a higher disorder in the blend and P3HT/$PC_{61}BM$ interfaces introducing these deep defects. This assignment is supported by standard TSC and DLTS measurements, exhibiting a higher ratio of deep traps in pristine solar cells compared to annealed ones. The findings are in accordance to reported lower hole mobilities and slower bimolecular recombination dynamics in pristine solar cells, which were attributed to deep traps.

Furthermore, the lower limit of the trap densities obtained by TSC measurements of annealed P3HT:$PC_{61}BM$ solar cells is in the range of $n_t \geq (6-8) \times 10^{22}$ m^{-3}, which is considerably higher than the values found for the pure materials.

8. Oxygen Induced Degradation of P3HT:PC_{61}BM Blends [1]

8.1. Introduction

So far, the main issue in the research on organic photovoltaics was in enhancing the efficiency, with great success. Power conversion efficiencies of 8.3 % for organic BHJ solar cells have already been achieved, with growing tendency [41]. However, towards commercialization another critical task has to be addressed: the lifetime of these devices. To gain a detailed understanding of the device stability, as well as the underlying degradation mechanism and their impact on the solar cell performance is an important prerequisite for lifetime enhancements.

Organic solar cells undergo many degradation pathways during their lifetime. Efficiency losses due to light [119], oxygen [100, 125] and water [108] are reported. The details of the degradation processes, however, are still not completely understood. Other studies, on the contrary, are only focused on the degradation of a single active material instead of the blend. For example for P3HT oxygen is known to form a charge transfer complex [1] resulting in p-doping of P3HT [81, 92], which is also investigated theoretically by band-structure calculations [84]. Furthermore, oxygen induced degradation of P3HT is reported to result in decreased mobilities [1] and increased trap densities (Chapter 5). In the case of C_{60}, oxygen also causes decreased electron mobilities [69, 136] and increased trap densities [88], as demonstrated by investigations of C_{60} based field effect transistors.

This chapter addresses the oxygen induced degradation of P3HT:PC_{61}BM solar cells in the dark, as well as under simultaneous illumination. Detailed investigations including charge carrier mobility, charge carrier density and defect spectroscopic measurements are performed to get an insight of the degradation mechanism due to oxygen in P3HT:PC_{61}BM solar cells. The experimental findings are supplemented by macroscopic simulations, based on solving the differential equation system of Poisson, continuity and drift–diffusion equations in one dimension.

8.2. Experimental Details

The investigated bulk heterojunction solar cells were prepared by spin coating P3HT:PC_{61}BM (ratio 1:0.8) blends made from solutions of 30 mg/ml in chlorobenzene on PEDOT:PSS covered indium tin oxide/glass substrates. The active layers were about 240 nm thick. After an annealing step of 10 min at 130 °C, Ca (1.5 nm)/Al (60 nm) contacts were evaporated thermally. The effective areas of the solar cells were 3 mm^2 and 9 mm^2.

[1] The results of this Chapter are published in J. Schafferhans et al., *Oxygen doping of P3HT:PCBM blends: Influence on trap states, charge carrier mobility and solar cell performance*, Organic Electronics 11 (2010), 1693.

Initial current–voltage (IV) characteristics of the solar cells were measured in the nitrogen glovebox. For the illumination of the cells an Oriel 81160 AM1.5G solar simulator was used. The power conversion efficiencies of the investigated samples were 3 % – 3.5 %.

Degradation studies of the unprotected solar cells were performed in a closed cycle cryostat. During the thermally stimulated current (TSC), charge carrier extraction by linearly increasing voltage (CELIV) [26, 59] and IV–measurements the cryostat was filled with helium as contact gas. To investigate the influence of oxygen on the solar cells, the helium was replaced with synthetic air (80 % N_2, 20 % O_2, $<$ 1 ppm H_2O) for different degradation times. Thus, the effect of humidity was excluded. This exposure was always done at a constant temperature of 300 K. Two different degradation conditions were investigated: in synthetic air either in the dark or under illumination. For the latter a 10 W high power white light emitting diode (Seoul) was used. The light intensity was adjusted to match the short-circuit current of the non degraded cells obtained under the solar simulator. The LED was also used for the illuminated IV-curves in the cryostat.

For TSC measurements the trap filling was achieved by illumination of the samples at 18 K for five minutes using the 10 W LED. After a dwell time of five minutes the temperature was increased with a constant heating rate of 7 K/min up to 300 K.

CELIV measurements were performed at 300 K. To extract the equilibrium charge carriers, a triangular bias pulse in reverse direction with peak voltage V_a = 2 V was applied on the Ca/Al electrode. A voltage pulse width of 50 μs was chosen.

8.3. Results and Discussion

8.3.1. Experimental Results

The IV-curves for different degradation times between 0 h and 120 h in synthetic air in the dark are shown in Figure 8.1a. The obtained values for the power conversion efficiency (PCE), fill factor (FF), open-circuit voltage (V_{oc}) and short-circuit current (J_{sc}), normalized to the initial values are presented in Figure 8.1b. The observed efficiency loss with dark degradation time is only due to J_{sc}, which decreases about 60 % within 120 h, whereas V_{oc} and FF remain almost constant. Since the exposure of the samples to synthetic air in the dark results only in a loss in J_{sc}, a degradation of the electrodes being the origin of these findings can be excluded. Degradation (oxidation) of the Ca/Al electrode would result in the occurrence of a s-shaped IV-curve [143], at least in a strong loss in FF or a change in V_{oc}. Neither of these effects was observed within the timescale of degradation considered here. Furthermore, it should be noted that the same degradation effects were observed for P3HT:PC$_{61}$BM solar cells without Ca interlayer.

In contrast to degradation in synthetic air in the dark, the efficiency loss after exposure of the solar cells to synthetic air and simultaneous illumination (Figure 8.2a, b) occurs on a faster time scale—about 30 % efficiency loss within 180 min. This is caused by a decrease of J_{sc}, as well as FF and V_{oc}, which all decrease about 10 % within this time scale. Since, in the case of dark degradation, FF and V_{oc} are unaffected, the decrease of both during photodegradation is due to light in the presence of oxygen, indicating an additional degradation path via photooxidation in addition to doping.

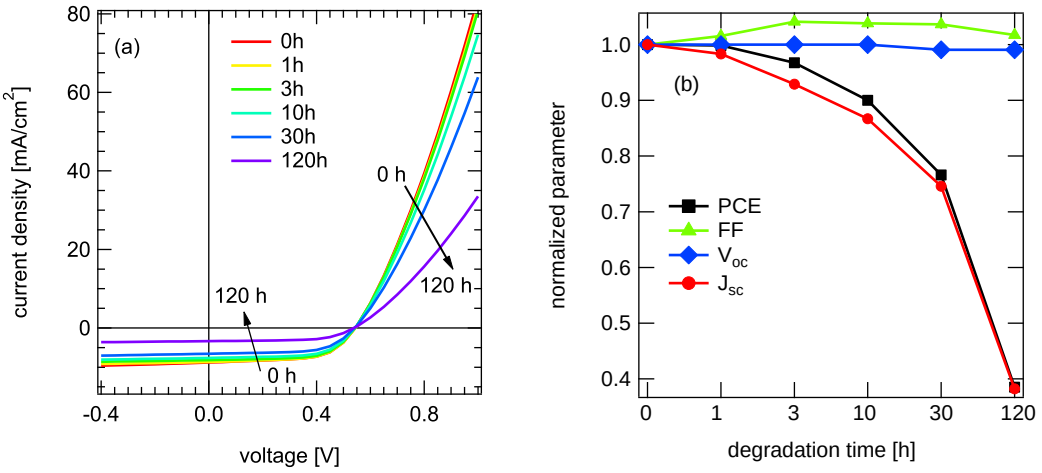

Figure 8.1.: Illuminated IV-curves of a P3HT:$PC_{61}BM$ solar cell for different dark degradation times in synthetic air (a) and the normalized values of the PCE, fill factor, open-circuit voltage and short-circuit current (b). The efficiency loss is due to the decrease of the short-circuit current.

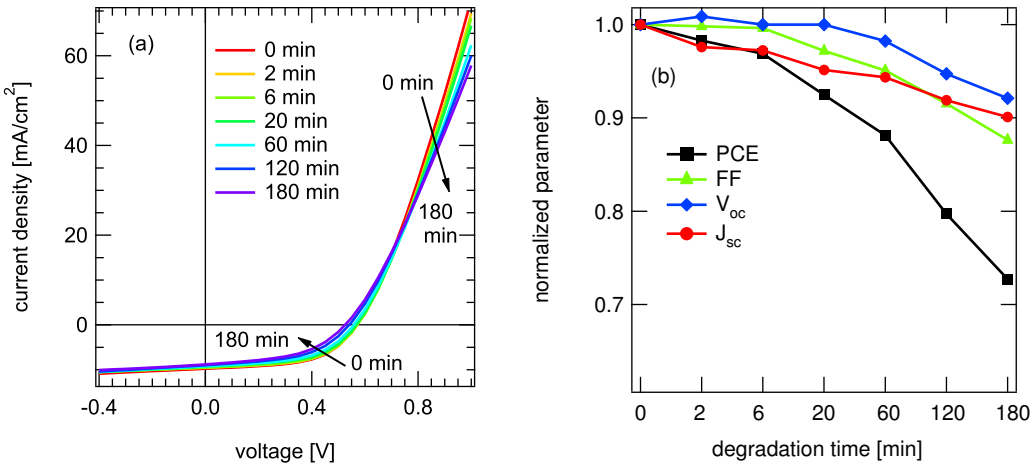

Figure 8.2.: Illuminated IV-curves of a P3HT:$PC_{61}BM$ solar cell for different degradation times in synthetic air under simultaneous illumination (a) and the normalized values of the PCE, fill factor, open-circuit voltage and short-circuit current (b). In contrast to dark degradation in synthetic air all parameters decrease.

To gain a deeper understanding of the underlying degradation mechanisms, TSC measurements were performed to obtain information about the electronic trap states of P3HT:$PC_{61}BM$ solar cells for dark as well as photodegradation. The TSC spectra of a P3HT:$PC_{61}BM$ solar cell for different dark degradation times in synthetic air are shown in Figure 8.3a. Thermally stimulated current is detected between 18 K and 160 K. At higher temperatures no additional TSC peaks can be observed up to 300 K. With exposure to synthetic air, a shoulder at about 100 K appears, increasing with degradation time, within the investigated time scale up to 100 h. The appearance of the shoulder indicates an increase in density of the deeper traps or even the

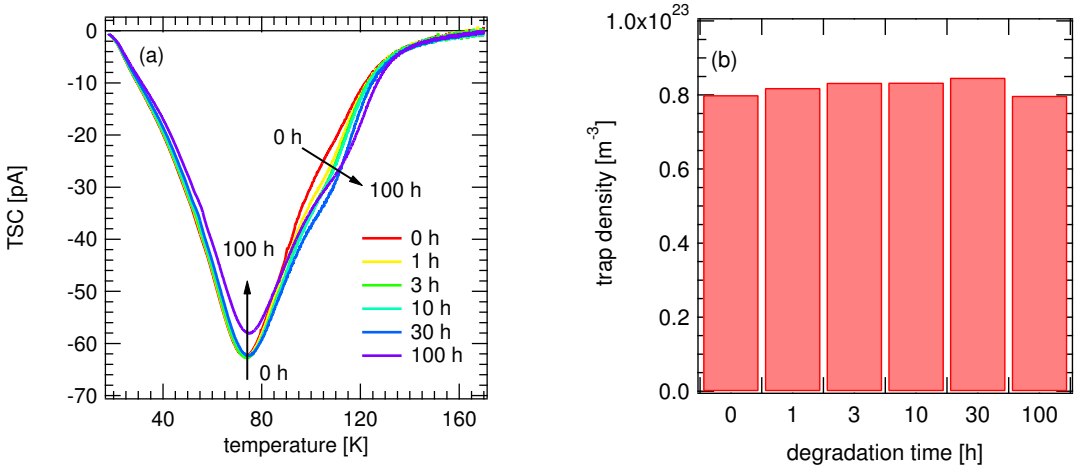

Figure 8.3.: TSC spectra of a P3HT:PC$_{61}$BM solar cell for different dark degradation times in synthetic air (a) and the obtained trap densities (b). The trap density remains almost constant. The slight decrease of the trap density for 100 h degradation time is possibly due to an enhanced recombination of the detrapped charge carriers.

formation of additional traps. The main peak however decreases slightly. As a result the overall trap density of the blend obtained by the TSC measurements remains almost constant for the different degradation times (Figure 8.3b). In this context it has to be mentioned once more that the determined trap density from the TSC spectra is only a lower limit of the actual trap density [63]. One reason is a possible recombination between electrons and holes after one of them got detrapped due to thermal activation. For degradation on synthetic air and simultaneous illumination almost the same behavior of TSC spectra was monitored, but on a faster timescale than during dark degradation.

To get further information about the influence of oxygen on the mobility and also the charge carrier concentration of the blend, the CELIV technique was used, which enables the simultaneous investigation of equilibrium charge carrier density and mobility by recording transient currents . The CELIV measurements for different degradation times in synthetic air in the dark are shown in Figure 8.4a. The CELIV curves exhibit a high asymmetry, especially for longer degradation times, which might result from trapped charge carriers being extracted as the higher voltages at longer times promote emission from traps. This is in accordance with the increase of the deeper traps density as revealed by the TSC measurements. The mobility for different degradation times was calculated from the position of the current peak maximum according to reference [26]. Only a slight decrease of the mobility with degradation time can be observed (Figure 8.4b), resulting in a decrease of about 50 % after 120 h in synthetic air. The equilibrium charge carrier density, extracted by the CELIV measurements, however, increases about a factor of two within a degradation time of 120 h in the dark (Figure 8.4c). These additional charge carriers can be attributed to oxygen doping of P3HT, which was also reported for P3HT field effect transistors [81, 92]. It has to be noted that the concentration of charges measured by CELIV provides only a lower limit of the actual charge carrier density, since only charge carriers extracted within the time scale of the experiment (voltage pulse width typically 50 μs) are observed. Thus, the experimental number includes charges from comparably shallow traps which can be emitted from them and then be extracted; charges in deeper traps as well as the

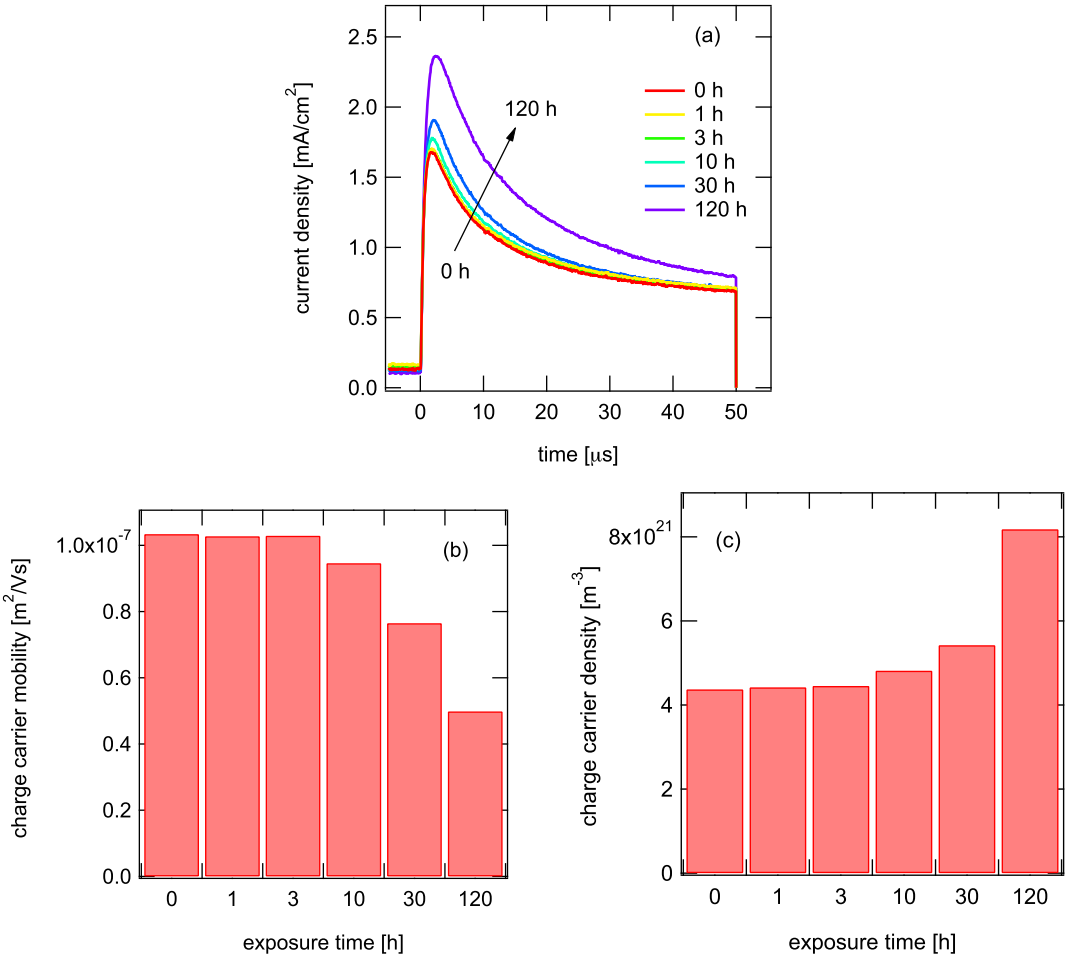

Figure 8.4.: CELIV measurements of a P3HT:$PC_{61}BM$ solar cell for different dark degradation times in synthetic air for offset bias of -0.3 V applied at the Ca/Al electrode (a) and the obtained mobilities (b) as well as the charge carrier densities (c). The charge carrier mobility slightly decreases with degradation time, whereas the charge carrier density shows an increase due to oxygen doping.

ones lost within the sample (by recombination) are disregarded. The degradation on synthetic air and simultaneous illumination shows similar results for the changes in mobility and charge carrier concentration, but again the degradation is accelerated to a timescale of minutes instead of hours.

8.3.2. Simulation

In order to understand the influence of a decreased mobility as well as charge carrier doping on the solar cell parameters, macroscopic simulations based on solving the differential equation system of the Poisson, the continuity and the drift–diffusion equations in one dimension [30, 31] were performed. In the simulation a bimolecular non-geminate recombination rate according to Langevin (Equations 2.3 and 2.4) was accounted. The charge carrier generation by light was assumed to create free polarons, neglecting any influence of electric field driven polaron pair

dissociation. Furthermore, the charge carrier mobilities of electrons and holes were set equal in the simulations. The used parameters are listed in Table 8.1. Using this approach the effect of

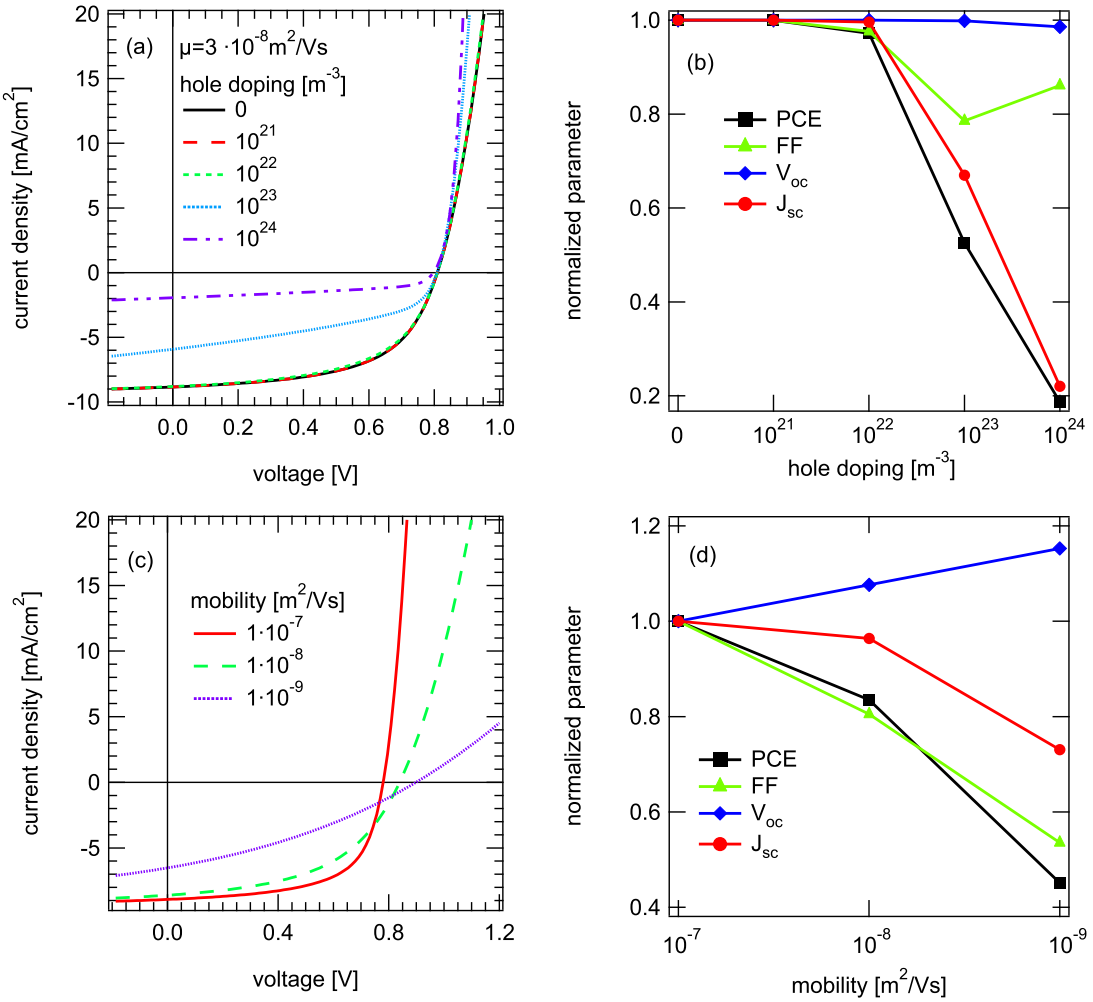

Figure 8.5.: Simulated IV-curves for different levels of hole doping (a) and the normalized values of the PCE, fill factor, open-circuit voltage and short-circuit current (b). An increased doping level results in a decrease of J_{sc}. A lowered charge carrier mobility (c) instead leads to a decrease of J_{sc} and FF (d).

charge carrier doping by oxygen on the solar cell parameters was investigated.

The simulated IV-curves for different hole doping levels are shown in Figure 8.5a and the corresponding normalized solar cell parameters in Figure 8.5b. For the given parameter set, doping concentration up to 10^{22} m^{-3} does not change the PCE, whereas for higher concentrations the PCE strongly decreases due to a decrease of J_{sc}. FF and V_{oc}, however, remain almost unaffected. This behavior is almost independent of the mobility (within changes of one order of magnitude) used for the simulations. The decreased J_{sc} due to doping can be explained by an increased bimolecular recombination probability. Since doping implies additional charges within the device, it leads to less band bending and therefore a reduced electrical field within the solar cell. As a consequence the extraction time for the charge carriers increases leading to a higher recombination probability and thus to a lower short-circuit current.

parameter	symbol	value	unit
temperature	T	300	K
effective band gap	E_g	1.30	eV
relative dielectric constant	ε_r	3.6	
active layer thickness	L	100	nm
effective density of states	N_c, N_v	8.0×10^{25}	$1/m^3$
generation rate	G	6.0×10^{27}	$1/m^3s$
injection barriers	Φ_a, Φ_c	0.1	eV

Table 8.1.: Parameters used for the simulations.

The influence of the mobility on the solar cell performance is shown in Figure 8.5c,d, revealing a loss of J_{sc} and FF and a small increase of V_{oc} for decreased mobilities. A lower mobility leads to a higher extraction time for the charge carriers and therefore to an enhanced bimolecular recombination probability, which results in the decreased FF. At the same time, the charge extraction becomes less efficient. The slightly increasing open-circuit voltage is due to a lower Langevin recombination rate due to decreased mobilities. The higher charge carrier densities and their more balanced distribution reduce the internal electric field and therefore increase the open-circuit voltage [20, 70]. If the field dependent polaron pair dissociation was also taken into account, it would mostly influence the FF and J_{sc} resulting in an even stronger decrease with lower mobilities.

8.3.3. Discussion

The influence of oxygen on P3HT:PC_{61}BM solar cells results in the case of dark degradation in a loss in J_{sc}, whereas photodegradation results in a decrease of all solar cell parameters. Further, the degradation due to oxygen is accelerated by light. A similar behavior was recently reported for inverted P3HT:PC_{61}BM solar cells [125], where the efficiency yielded almost no change for dark degradation within the investigated timescale of 1 h, whereas a strong loss for photodegradation within 120 min was observed.

The loss in J_{sc} can be explained by charge carrier doping, as demonstrated by using macroscopic simulations. This interpretation is in accordance with the CELIV measurements, which show an increasing charge carrier concentration with degradation time. The increased charge carrier concentration can be attributed to oxygen doping of P3HT [81, 92]. The difference between the doping levels in the simulations and these determined by CELIV can be explained by the fact that the extracted charge carrier density by CELIV is only a lower limit of the actual charge carrier concentration, as mentioned before. The actual charge carrier density can be significantly higher. Furthermore, the accelerated increase of the charge carrier density in the case of photodegradation compared to the dark degradation is in good agreement with results on P3HT transistors, which also showed an expedited oxygen doping with light [81].

In addition to an increased charge carrier concentration, CELIV measurements reveal a decrease of the charge carrier mobility for the P3HT:PC_{61}BM blends due to oxygen. A decreasing mobility with degradation time is also seen for pure P3HT (Chapter 5), but in contrast to pure

P3HT, where the mobility decreases about two orders of magnitude within 100 h, only a slight decrease in the blend—by about 50 %—can be observed. This difference could be due to a stabilization effect of $PC_{61}BM$ for P3HT in analogy to findings for MDMO-PPV (poly(2-methoxy-5-(3',7'- dimethyloctyloxy)-1,4-phenylene-vinylene)):$PC_{61}BM$ solar cells [100]. However, the decreased mobility could also result from a degradation of $PC_{61}BM$ due to oxygen. Decreased electron mobilities for C_{60} based field effect transistors after oxygen exposure have already been reported [69, 136]. Since electron and hole mobilities can not be discriminated by CELIV, it is not possible to resolve which carrier mobility decreases.

A lower mobility leads to a decrease of FF and J_{sc}, as revealed by macroscopic simulations. Although the CELIV measurements show a slight decrease in mobility with degradation time, there are some facts indicating that the decreased mobility is probably not the origin of the FF loss in the case of photodegradation. First of all the experimentally observed mobility reduction is too limited to have a strong impact on the FF. Furthermore, the mobility decreases in the same range for both dark and illuminated degradation, although the degradation in the illuminated case occurs on a faster timescale. In contrast, the loss in FF is only observed for photodegradation. Additionally, a decrease of V_{oc} is experimentally observed for photodegradation. A significant decrease in mobility, however, should result in an increase of V_{oc} as exhibited by the simulation (Figure 8.5d). Therefore, the slightly decreased mobility is probably not the reason for the FF loss.

Another important factor which can negatively influence the solar cell performance are electronic trap states, since they lower the mobility, disturb the internal field distribution and can act as recombination centers. Exposure of P3HT:$PC_{61}BM$ solar cells to oxygen results in a raise of the density of deeper traps for both dark and illuminated degradation. On the other hand, the main peak of the TSC slightly decreases due to oxygen exposure, which is in contrast to the observed increase of the main TSC peak of pure P3HT (Section 5). For comparison, the trap density in pure P3HT increases more than a factor of two within 50 h in air. Yet, the determined trap density from the TSC spectra is only a lower limit of the actual trap density and the slight decrease of the main peak in the blend might be due to an enhanced recombination of detrapped charge carriers of opposite sign.

The formation of the deeper traps due to oxygen exposure could also be the reason for the observed loss in fill factor, since they can disturb the internal field distribution and act as recombination centers, as mentioned before. Further investigations concerning the influence of deep traps on the solar cell performance should be addressed in future, like the implementation within the macroscopic simulation. Other crucial factors concerning FF and V_{oc}, are e.g. imbalanced electron–hole mobilities (resulting in the formation of space charges) and a field dependent photogeneration. These two factors have not been accounted so far and might be also addressed in future to completely clarify the origin of the loss in FF and V_{oc} in the case of oxygen induced degradation under simultaneous illumination.

8.4. Conclusions

The influence of oxygen on unprotected P3HT:PC_{61}BM solar cells was investigated by controlled exposure to synthetic air. Two different degradation conditions were used: in the dark and under simultaneous illumination. Exposure of the solar cells to synthetic air in the dark results in a loss of J_{sc} of about 60 % within 120 h. In contrast, simultaneous illumination during oxygen degradation results in a loss of all solar cell parameters, yielding an efficiency loss of about 30 % within only 3 hours. Thus, the degradation of the P3HT:PC_{61}BM solar cells is strongly accelerated by light.

CELIV measurements revealed an increased charge carrier concentration after oxygen exposure for dark, as well as photodegradation. These additional charge carriers were attributed to oxygen doping, which is also known for pure P3HT. With the aid of macroscopic simulations it was shown that doping of the solar cells is the origin of the loss in J_{sc} for both degradation conditions.

In addition to an enhanced charge carrier concentration, oxygen induced degradation results in an increase of the density of deeper traps, as was revealed by TSC measurements.

Another impact of oxygen exposure on P3HT:PC_{61}BM solar cells is a slight decrease of the charge carrier mobility. Although a decreased mobility may result in a loss of the fill factor, as shown by macroscopic simulations, the experimentally observed mobility decrease is too small to be the origin of the FF drop in the case of photodegradation.

Even though the loss in J_{sc} could be attributed to doping, the origin of the loss in FF and V_{oc} during photodegradation ist still not completely understood. Approaches to clarify this might be the implementation of deep traps in the simulation as well as investigations concerning imbalanced mobilities and field dependent photogeneration.

9. Summary

In this work, the trap states in the conjugated polymer P3HT, often used as electron donor in organic bulk heterojunction solar cells, three commonly used fullerene based electron acceptors and P3HT:$PC_{61}BM$ blends were investigated. Furthermore, the trap states in the blend were compared with these of the pure materials. Concerning the lifetime of organic solar cells the influence of oxygen on P3HT and P3HT:$PC_{61}BM$ blends was studied. The experimental techniques used to investigate the trap states in the organic semiconductors, their densities as well as activation energies were (fractional) thermally stimulated current (TSC) and current based deep level transient spectroscopy (Q-DLTS).

The charge transport in disordered organic semiconductors is generally described as hopping within a Gaussian density of localized states (DOS). With the aid of the transport energy a distinction between trap states and regular transport states is possible, despite all states are localized: States below the transport energy act as traps, since the release of charges from these states to the transport level are the rate limiting hops. Thus, the tail states of the Gaussian density of states act as traps. Furthermore, there can be states which are in addition to the Gaussian DOS. If these states are below the transport level, they also act as traps. Such additional trap states can be for example impurities, grain boundaries in polycrystalline layers or interface states between two materials.

Fractional TSC measurements on P3HT diodes revealed a quasi-continuous trap distribution between 25 meV and 160 meV. The distribution suggested two different traps in P3HT with approximately Gaussian energy distributions and maxima at about 50 meV and 105 meV. Thereby, the former was attributed to the tail states within the regular Gaussian density of states due to the low activation energy. The latter, deeper traps, however, exhibited a strong dependence on oxygen. Exposure of the P3HT diodes to oxygen, ambient air and synthetic (dry) air all revealed an increase of the deeper traps density with exposure time in the same manner. While the lower limit of the trap density in non aged P3HT samples was in the range of $(1.0-1.2)\times 10^{22}$ m^{-3}, it was more than doubled after an exposure of 50 h to air. An increase of the trap density with oxygen exposure time was also seen in the Q-DLTS measurements accompanied with an increase of the temperature dependence of the emission rates, indicating an enhanced formation of deeper traps. Due to the raise in density of the deeper traps, the charge carrier mobility in P3HT significantly decreased, as revealed by photo-CELIV measurements, resulting in a loss in mobility of about two orders of magnitude after 100 h exposure to synthetic air. The increased trap density was attributed to p-doping of P3HT by the transfer of an electron to adsorbed oxygen. The negatively charged O_2^- can Coulombically interact with the holes in P3HT, resulting in a higher energetic disorder in the HOMO levels of P3HT and thus introducing a higher density of trap states for holes. This effect was partially reversible by applying vacuum to the sample for several hours or, more significantly, by a thermal treatment of the devices in nitrogen atmosphere.

The trap states in the methanofullerenes $PC_{61}BM$, bis$PC_{61}BM$ and $PC_{71}BM$ were inves-

tigated by TSC measurements. $PC_{61}BM$ yielded a broad quasi-continuous trap distribution between 15 meV and 270 meV and the maximum of the distribution at about 75 meV. The comparison of the TSC spectra of the three methanofullerenes exhibited significant differences in the trap states. $PC_{71}BM$ yielded two maxima corresponding to activation energies of 96 meV and 223 meV. Also in bis$PC_{61}BM$ two maxima could be revealed in the TSC spectrum with activation energies of 45 meV and 184 meV, however, an additional shoulder in the high temperature range of the TSC spectrum proposed a significant amount of even deeper traps. The higher activation energies of the most prominent traps in bis$PC_{61}BM$ and $PC_{71}BM$ compared to $PC_{61}BM$ probably originate from the different isomers, these two fullerene derivatives consist of. Each of the isomers yields different LUMO energies, where the lower ones can act as traps. The lower limit of the trap density of all of the three investigated fullerene derivatives exhibited values in the order of 10^{22} m^{-3}, with the highest for bis$PC_{61}BM$ and the lowest for $PC_{61}BM$.

By applying fractional TSC measurements on P3HT:$PC_{61}BM$ solar cells, it was shown that the trap distribution in the blend is a superposition of the traps in pure P3HT and $PC_{61}BM$ and additional deeper traps in the range of about 250 meV to 400 meV. The origin of these additional traps, which can not be related to the pure materials, was attributed to a higher disorder in the blend and P3HT/$PC_{61}BM$ interfaces. This conclusion was supported by standard TSC and Q-DLTS measurements performed on pristine and annealed P3HT:$PC_{61}BM$ blends, exhibiting a higher ratio of the deep traps in the pristine samples. The lower limit of the trap density of the investigated annealed solar cells was in the range of $(6-8)\times 10^{22}$ m^{-3}, which was considerably higher than in the pure materials.

The influence of oxygen on P3HT:$PC_{61}BM$ solar cells was investigated by exposure of the devices to synthetic air under specific conditions. Exposure of the solar cells to oxygen in the dark resulted in a strong decrease in the power conversion efficiency of 60 % within 120 h, which was only caused by a loss in short-circuit current. Simultaneous illumination of the solar cells during oxygen exposure strongly accelerated the degradation, resulting in an efficiency loss of 30 % within only 3 h. Thereby, short-circuit current, open-circuit voltage and fill factor all decreased in the same manner. TSC measurements revealed an increase of the density of deeper traps for both degradation conditions, which resulted in a decrease of the mobility, as investigated by CELIV measurements. However, these effects were less pronounced than in pure P3HT. Furthermore, an increase of the equilibrium charge carrier density with degradation time was observed, which was attributed to oxygen doping of P3HT. With the aid of macroscopic simulations, it was shown that the doping of the solar cells is the origin of the loss in short-circuit current for both degradation conditions.

10. Zusammenfassung

In der vorliegenden Arbeit wurden die elektronischen Störstellen in dem konjugierten Polymer P3HT, welches häufig als Elektronendonator in organischen Mischabsorbersolarzellen verwendet wird, in drei üblichen, auf Fullerenen basierenden, Elektronenakzeptoren und im P3HT:PC_{61}BM Gemisch untersucht. Des Weiteren wurden die Störstellen im Gemisch mit denen der reinen Materialien verglichen. Im Hinblick auf die Lebensdauer organischer Solarzellen wurde der Einfluss von Sauerstoff auf P3HT und das P3HT:PC_{61}BM Gemisch untersucht. Die verwendeten Methoden um die Störstellen, deren Dichten und Aktivierungsenergien, in den organischen Halbleitern zu untersuchen, waren (fraktionierte) thermisch stimu-lierte Ströme (TSC) und strombasierte transiente Störstellenspektroskopie (Q-DLTS).

Der Ladungstransport in ungeordneten organischen Halbleitern wird gemeinhin als Hüpfprozess innerhalb einer gaußverteilten Zustandsdichte (DOS) lokalisierter Zustände beschrieben. Mit Hilfe der Transportenergie ist eine Unterscheidung zwischen elektronischen Störstellen und regulären Transportzuständen dennoch möglich, auch wenn alle Zustände lokalisiert sind: Zustände unterhalb der Transportenergie fungieren als Störstellen, da die Befreiung der Ladungsträger aus diesen Zuständen zu der Transportenergie die limitierenden Sprünge darstellt. Somit werden die Ausläufer der gaußförmigen Zustandsdichte als Störstellen betrachtet. Des Weiteren können im organischen Halbleiter energetische Zustände zusätzlich zur gaußförmigen DOS vorliegen. Falls sich diese Zustände unterhalb der Transportenergie befinden, agieren sie ebenfalls als Ladungsträgerfallen. Solche zusätzlichen Störstellen können zum Beispiel Verunreinigungen, Korngrenzen innerhalb einer polykristallinen Schicht, oder Grenzflächenzustände zwischen zwei Materialien sein.

Fraktionierte TSC Messungen an P3HT Dioden ergaben eine quasi-kontinuierliche Störstellenverteilung zwischen 25 meV und 160 meV. Die Verteilung lies darauf schließen, dass in P3HT zwei verschiedene Störstellen mit jeweils annähernd gaußförmiger energetischer Verteilung vorliegen, deren Maxima Aktivierungsenergien von 50 meV und 105 meV besitzen. Dabei konnte, aufgrund ihrer geringen Aktivierungsenergie, erstere den Ausläufern der regulären gaußförmigen DOS zugewiesen werden. Die tiefere Störstelle jedoch wies eine starke Abhängigkeit von Sauerstoffexposition auf. Das gezielte Aussetzten von P3HT Dioden an Sauerstoff, Umgebungsluft und synthetischer (trockener) Luft, ergab in gleicher Weise eine Zunahme in der Dichte der tieferen Störstellen mit zunehmender Expositionszeit. Während die untere Abschätzung der Störstellendichte für ungealterte P3HT Proben im Bereich von $(1.0-1.2)\times 10^{22}$ m^{-3} lag, hat sich diese nach 50 Std. an Luft mehr als verdoppelt. Eine Zunahme der Störstellendichte durch Sauerstoffexposition wurde ebenfalls mit Q-DLTS Messungen beobachtet. Dies ging mit einer Zunahme der Temperaturabhängigkeit der Emissionsraten einher, was auf ein vermehrtes Auftreten tieferer Störstellen schließen lies. Die Zunahme in der Dichte der tieferen Störstellen führte zu einer signifikanten Abnahme der Ladungsträgerbeweglichkeit, wie mittels photo-CELIV Messungen gezeigt wurde. Die Beweglichkeitsabnahme betrug dabei etwa zwei Größenordnungen nach 100 Std. Exposition an synthetischer Luft. Die

erhöhte Störstellendichte wurde der p-Dotierung des Polymers zugeschrieben, welche durch Elektronentransfer von P3HT auf angelagerten Sauerstoff hervorgerufen wird. Das negativ geladene O_2^- führt durch Coulombwechselwirkung mit den sich auf dem P3HT befindenden Löchern zu einer Erhöhung der energetischen Unordnung der HOMO Niveaus von P3HT, was in einer Zunahme der Störstellenkonzentration für Löcher resultiert. Dieser Effekt war teilweise reversibel, zum einen durch Aussetzen der Proben an Vakuum für mehrere Stunden, oder noch effektiver, durch Tempern der Proben in Stickstoffatmosphäre.

Die Störstellen in den Methanofullerenen $PC_{61}BM$, bis$PC_{61}BM$ und $PC_{71}BM$ wurden mittels TSC Messungen untersucht. $PC_{61}BM$ wies eine breite quasi-kontinuierliche Störstellenverteilung zwischen 15 meV und 270 meV mit dem Maximum der Verteilung bei etwa 75 meV auf. Der Vergleich der TSC Spektren der drei Methanofullerene zeigte wesentliche Unterschiede in den Störstellen. In $PC_{71}BM$ ergaben sich zwei Maxima mit zugehörigen Aktivierungsenergien von 96 meV und 223 meV. Auch in bis$PC_{61}BM$ konnten zwei Maxima mit Aktivierungsenergien von 45 meV und 184 meV im TSC Spektrum beobachtet werden. Eine zusätzliche Schulter an der Hochtemperaturflanke des TSC Spektrums lies hier jedoch auf eine erhebliche Anzahl an noch tieferen Störstellen schließen. Die hohen Aktivierungsenergien der ausgeprägtesten Störstellen in bis$PC_{61}BM$ und $PC_{71}BM$ verglichen mit $PC_{61}BM$ sind auf die verschiedenen Isomere, aus denen die beiden Fullerenderivate bestehen, zurückzuführen. Jedes der Isomere besitzt verschiedene LUMO Niveaus, wobei die tiefer liegenden als Störstellen fungieren können. Die untere Abschätzung der Störstellendichte aller drei untersuchten Methanofullerene ergab Werte in der Größenordnung von 10^{22} m^{-3}, mit der höchsten Störstellenkonzentration für bis$PC_{61}BM$ und der niedrigsten für $PC_{61}BM$.

Mittels fraktionierter TSC Messungen an P3HT:$PC_{61}BM$ Solarzellen wurde gezeigt, dass die Störstellenverteilung im Gemisch eine Überlagerung der Störstellen der Einzelmaterialien und zusätzlicher tiefer gelegener Ladungsträgerfallen mit Aktivierungsenergien von etwa 250 meV bis 400 meV ist. Diese zusätzlichen, nicht auf die Einzelmaterialien zurückführbaren Störstellen wurden der höheren Unordnung im Gemisch und P3HT/$PC_{61}BM$ Grenzflächen zugeschrieben. Diese Folgerung wurde durch TSC und DLTS Messungen gestützt, welche an ungetemperten und getemperten P3HT/$PC_{61}BM$ Gemischen durchgeführt wurden und einen erhöhten Anteil tiefer Störstellen in der ungetemperten Solarzelle darlegten. Die untere Abschätzung der Störstellendichte lag für die untersuchten getemperten Solarzellen im Bereich von $(6-8)\times 10^{22}$ m^{-3} und somit deutlich höher als in den Einzelmaterialien.

Der Einfluss von Sauerstoff auf P3HT:$PC_{61}BM$ Solarzellen wurde durch gezielte Exposition der Proben an synthetischer Luft untersucht. Die Exposition der Solarzellen an synthetischer Luft im Dunklen resultierte in einer starken Abnahme der Solarzelleneffizienz von 60 % innerhalb von 120 Std., was alleine von der Abnahme des Kurzschlussstroms herrührte. Gleichzeitige Beleuchtung der Solarzellen während der Sauerstoffexposition führte zu einer starken Beschleunigung des Effizienzverlustes von 30 % innerhalb von nur 3 Std. Hierbei nahmen Kurzschlussstrom, Leerlaufspannung und Füllfaktor gleichsam ab. TSC Messungen zeigten eine Zunahme in der Konzentration der tieferen Störstellen für beide Degradationsbedingungen, was zu einer Abnahme der Ladungsträgerbeweglichkeit führte, wie mittels CELIV Messungen gezeigt wurde. Jedoch waren diese beiden Effekte weniger ausgeprägt als in reinem P3HT. Des Weiteren wurde eine Zunahme der Gleichgewichtsladungsträgerkonzentration mit zunehmender Degradationszeit beobachtet, was auf Sauerstoffdotierung des P3HT zurückgeführt wurde. Unter Zuhilfenahme makroskopischer Simulationen konnte gezeigt werden, dass

die Dotierung der Solarzellen die Ursache für die Abnahme des Kurzschlussstroms für beide Degradationsbedingungen ist.

Bibliography

[1] M. S. A. Abdou, F. P. Orfino, Y. Son, and S. Holdcroft. Interaction of oxygen with conjugated polymers: Charge transfer complex formation with poly(3-alkythiophenes). *J. Am. Chem. Soc.*, 119:4518, 1997.

[2] T. D. Anthopoulos, D. M. de Leeuw, E. Cantatore, S. Setayesh, E. J. Meijer, C. Tanase, J. C. Hummelen, and P. W. M. Blom. Organic complementary-like inverters employing methanofullerene-based ambipolar field-effect transistors. *Appl. Phys. Lett.*, 85:4205, 2004.

[3] T. D. Anthopoulos, D. M. de Leeuw, E. Cantatore, P. van 't Hof, J. Alma, and J. C. Hummelen. Solution processible organic transistors and circuits based on a C_{70} methanofullerene. *J. Appl. Phys.*, 98:054503, 2005.

[4] V. I. Arkhipov and G. J. Adriaenssens. Low-temperature relaxations of charge carriers in disordered hopping systems. *J. Phys.: Condens. Matter*, 8:7909, 1996.

[5] V. I. Arkhipov, E. V. Emelianova, and G. J. Adriaenssens. Effective transport energy versus the energy of most probable jumps in disordered hopping systems. *Phys. Rev. B*, 64:125125, 2001.

[6] V. I. Arkhipov, E. V. Emelianova, A. Kadashchuk, I. Blonsky, S. Nĕspůrek, D. S. Weiss, and H. Bässler. Polaron effects on thermally stimulated photoluminescence in disordered organic systems. *Phys. Rev. B*, 65:165218, 2002.

[7] V. I. Arkhipov, E. V. Emelianova, R. Schmechel, and H. von Seggern. Thermally stimulated luminescence versus thermally stimulated current in organic semiconductors. *Journal of Non-Crystalline Solids*, 338:626, 2004.

[8] V. I. Arkhipov, P. Heremans, E. V. Emelianova, G. J. Adriaenssens, and H. Bässler. Charge carrier mobility in doped semiconducting polymers. *Appl. Phys. Lett.*, 82:3245, 2003.

[9] V. I. Arkhipov, P. Heremans, E. V. Emelianova, and H. Bässler. Effect of doping on the density-of-states distribution and carrier hopping in disordered organic semiconductors. *Phys. Rev. B*, 71:045214, 2005.

[10] L. W. Barbour, R. D. Pensack, M. Hegadorn, S. Arzhantsev, and J. B. Asbury. Excitation transport and charge separation in an organic photovoltaic material: Watching excitations diffuse to interfaces. *J. Phys. Chem. C*, 112:3926, 2008.

[11] H. Bässler. Charge transport in disordered organic photoconductors — A Monte Carlo simulation study. *Phys. Stat. Sol. B*, 175:15, 1993.

[12] P. Blood and J. Orton. *The electrical characterization of semiconductors: Mahority carriers and electron states*. Academic Press Limited, 1992.

[13] N. Blouin, A. Michaud, and M. Leclerc. A low-bandgap poly(2,7-carbazole) derivative for use in high-performance solar cells. *Adv. Mater.*, 19:2295, 2007.

[14] C. Brabec, V. Dyakonov, and U. Scherf, editors. *Organic Photovoltaics*. Wiley-VCH, 2008.

[15] C. J. Brabec, S. Gowrisanker, J. J. M. Halls, D. Laird, S. Jia, and S. P. Williams. Polymer-fullerne bulk heterojunction solar cells. *Adv. Mater.*, 22:3839, 2010.

[16] C. J. Brabec, J. A. Hauch, P. Schilinsky, and C. Waldauf. Production aspects of organic photovoltaics and their impact on the commercialization of devices. *MRS Bulletin*, 30:50, 2005.

[17] C. L. Braun. Electric field assisted dissociation of charge transfer states as a mechanism of photocarrier production. *J. Chem. Phys.*, 80:4157, 1984.

[18] BSW-Solar/www.solarwirtschaft.de. last accessed February 2011.

[19] G. A. Buxton and N. Clarke. Predicting structure and property relations in polymeric photovoltaic devices. *Phys. Rev. B*, 74:085207, 2006.

[20] D. Cheyns, J. Poortmans, P. Heremans, C. Deibel, S. Verlaak, B. P. Rand, and J. Genoe. Analytic model for the open-circuit voltage and its associated resistance in organic planar heterojunction solar cells. *Phys. Rev. B*, 77:165332, 2008.

[21] T. M. Clarke and J. R. Durrant. Charge photogeneration in organic solar cells. *Chem. Rev.*, 110:6736, 2010.

[22] T. M. Clarke, F. C. Jamieson, and J. R. Durrant. Transient absorption studies of bimolecular recombination dynamics in polythiophene/fullerene blend films. *J. Phys. Chem. C*, 113:20934, 2009.

[23] E. Collini and G. D. Scholes. Coherent intrachain energy migration in a conjugated polymer at room temperature. *Science*, 323:369, 2009.

[24] V. Coropceanu, J. Cornil, D. A. da Silva Filho, Y. Olivier, R. Silbey, and J.-L. Brédas. Charge transport in organic semiconductors. *Chem. Rev.*, 107:926, 2007.

[25] T. A. T. Cowell and J. Woods. The evaluation of thermally stimulated current curves. *Brit. J. Appl. Phys.*, 18:1045, 1967.

[26] C. Deibel. Charge carrier dissociation and recombination in polymer solar cells. *Phys. Stat. Sol. A*, 206:2731, 2009.

[27] C. Deibel and V. Dyakonov. Polymer-fullerene bulk heterojunction solar cells. *Rep. Prog. Phys.*, 73:096401, 2010.

[28] C. Deibel, D. Mack, J. Gorenflot, A. Schöll, S. Krause, F. Reinert, D. Rauh, and V. Dyakonov. Energetics of excited states in the conjugated polymer poly(3-hexylthiophene). *Phys. Rev. B*, 81:085202, 2010.

[29] C. Deibel, T. Strobel, and V. Dyakonov. Origin of the efficient polaron-pair dissociation in polymer-fullerene blends. *Phys. Rev. Lett.*, 103:036402, 2009.

[30] C. Deibel, A. Wagenpfahl, and V. Dyakonov. Influence of charge carrier mobility on the performance of organic solar cells. *Phys. Stat. Sol. (RRL)*, 2:175, 2008.

[31] C. Deibel, A. Wagenpfahl, and V. Dyakonov. Origin of reduced polaron recombination in organic semiconductor devices. *Phys. Rev. B*, 80:075203, 2009.

[32] T. Erb, U. Zhokhavets, G. Gobsch, S. Raleva, B. Stühn, P. Schilinsky, C. Waldauf, and C. J. Brabec. Correlation between structural and optical properties of composite polymer/fullerne films for organic solar cells. *Adv. Funct. Mater.*, 15:1193, 2005.

[33] M. A. Faist, P. E. Keivanidis, S. Foster, P. H. Wöbkenberg, T. D. Anthopoulos, D. D. C. Bradley, J. R. Durrant, and J. Nelson. Effect of multiple adduct fullerenes on charge generation and transport in photovoltaic blends with poly(3-hexylthiophene-2,5-diyl). *Journal of Polymer Science: Part B: Polymer Physics*, 49:45, 2011.

[34] Z. Fang, L. Shan, T. E. Schlesinger, and A. G. Milnes. Study of defects in LEC-grown undoped Si-GaAs by thermally stimulated current spectroscopy. *Material Science and Engineering*, B5:397, 1990.

[35] I. I. Fishchuk, V. I. Arkhipov, A. Kadashchuk, P. Heremans, and H. Bässler. Analytic model of hopping mobility at large charge carrier concentrations in disordered organic semiconductors: Polarons versus bare charge carriers. *Phys. Rev. B*, 76:045210, 2007.

[36] A. Foertig, A. Baumann, D. Rauh, V. Dyakonov, and C. Deibel. Charge carrier concentration and temperature dependent recombination in polymer-fullerene solar cells. *Appl. Phys. Lett.*, 95:052104, 2009.

[37] J. Frenkel. On pre-breakdown phenomena in insulators and electronic semi-conductors. *Phys. Rev.*, 54:647, 1938.

[38] J. M. Frost, M. A. Faist, and J. Nelson. Energetic disorder in higher fullerene adducts: A quantum chemical and voltammetric study. *Adv. Mater.*, 22:4881, 2010.

[39] G. F. J. Garlick and A. F. Gibson. The electron trap mechanism of luminescence in sulphide and silicate phosphors. *Proc. Phys. Soc.*, 60:574, 1948.

[40] O. Gaudin, R. B. Jackman, T.-P. Nguyen, and P. L. Rendu. Determination of traps in poly(p-phenylene vinylene) light emitting diodes by charge-based deep level transient spectroscopy. *J. Appl. Phys.*, 90:4196, 2001.

[41] M. A. Green, K. Emery, Y. Hishikawa, and W. Warta. Solar cell efficiency tables (version 37). *Prog. Photovolt: Res. Appl.*, 19:84, 2011.

[42] R. R. Haering and E. N. Adams. Theory and application of thermally stimulated curents in photoconductors. *Phys. Rev.*, 117:451, 1960.

[43] A. W. Hains, J. Liu, A. B. F. Martinson, M. D. Irwin, and T. J. Marks. Anode interfacial tuning via electron-blocking/hole-transport layers and indium tin oxide surface treatment in bulk-heterojunction organic photovoltaic cells. *Adv. Funct. Mater.*, 20:595, 2010.

[44] J. J. M. Halls, J. Cornil, D. A. dos Santos, R. Silbey, D.-H. Hwang, A. B. Holmes, J. L. Brédas, and R. H. Friend. Charge-and energy-transfer processes at polymer/polymer interfaces: A joint experimental and theoretical study. *Phys. Rev. B*, 60:5721, 1999.

[45] A. Halperin and A. A. Braner. Evaluation of thermal activation energies from glow curves. *Phys. Rev.*, 117:408, 1960.

[46] B. Hartenstein, H. Bässler, A. Jakobs, and K. W. Kehr. Comparison between multiple trapping and multiple hopping transport in a random medium. *Phys. Rev. B*, 54:8574, 1996.

[47] Y. He, H.-Y. Chen, J. Hou, and Y. Li. Indene–C_{60} bisadduct: A new acceptor for high-performance polymer solar cells. *J. Am. Chem. Soc.*, 132:1377, 2010.

[48] D. Hertel and H. Bässler. Photoconduction in amorphous organic solids. *ChemPhysChem*, 9:666, 2008.

[49] W. Hoogenstraaten. Electron traps in ZnS phosphors. *Philips Res. Rep.*, 13:515, 1958.

[50] H. Hoppe, N. Arnold, N. S. Sariciftci, and D. Meissner. Modeling the optical absorption within conjugated polymer/fullerene-based bulk-heterojunction organic solar cells. *Sol. Ener. Mat. Sol. Cells*, 80:105, 2003.

[51] S. Hoshino, M. Yoshida, S. Uemura, T. Kodzasa, N. Takada, T. Kamata, and K. Yase. Influence of moisture on device characteristics of polythiophene-based field-effect transistors. *J. Appl. Phys.*, 95:5088, 2004.

[52] http://www.conrad.de/ce/de/product/110487/PP-120-ORGANISCHES-MODUL. last accessed March 2011.

[53] http://www.neubers.de/component/. last accessed March 2011.

[54] http://www.solennebv.com/content/section/2/15/. last accessed March 2011.

[55] Y.-S. Huang, S. Westenhoff, I. Avilov, P. Sreearunothai, J. M. Hodgkiss, C. Deleener, R. H. Friend, and D. Beljonne. Electronic structures of interfacial states formed at polymeric semiconductor heterojunctions. *Nature Mater.*, 7:483, 2008.

[56] I.-W. Hwang, D. Moses, and A. J. Heeger. Photoinduced carrier generation in P3HT/PCBM bulk heterojunction materials. *J. Phys. Chem. C*, 112:4350, 2008.

[57] A. A. Istratov and O. F. Vyvenko. Exponential analysis in physical phenomena. *Rev. Sci. Instrum.*, 70:1233, 1999.

[58] G. W. Jones, D. M. Taylor, and H. L. Gomes. DLTS investigation of acceptor states in P3MeT schottky barrier diodes. *Synth. Met.*, 85:1341, 1997.

[59] G. Juška, K. Arlauskas, M. Viliūnas, and J. Kočka. Extraction current transients: New method of study of charge transport in microcrystalline silicon. *Phys. Rev. Lett.*, 84:4946, 2000.

[60] G. Juška, K. Genevičius, N. Nekrašas, G. Sliaužys, and G. Dennler. Trimolecular recombination in polythiophene:fullerene bulk heterojunction solar cells. *Appl. Phys. Lett.*, 93:143303, 2008.

[61] G. Juška, K. Genevičius, R. Österbacka, K. Arlauskas, T. Kreouzis, D. D. C. Bradley, and H. Stubb. Initial transport of photogenerated charge carriers in π-conjugated polymers. *Phys. Rev. B*, 67:081201, 2003.

[62] A. Kadashchuk, N. Ostapenko, V. Zaika, and S. Něspůrek. Low-temperature thermoluminescence in poly(methyl-phenylsilylene). *Chemical Physics*, 234:285, 1998.

[63] A. Kadashchuk, R. Schmechel, H. von Seggern, U. Scherf, and A. Vakhnin. Charge-carrier trapping in polyfluorene-type conjugated polymers. *J. Appl. Phys.*, 98:024101, 2005.

[64] A. Kadashchuk, Y. Skryshevski, Y. Piryatinski, A. Vakhnin, E. V. Emelianova, V. I. Arkhipov, H. Bässler, and J. Shinar. Thermally stimulated photoluminescence in poly(2,5-dioctoxy p-phenylene vinylene). *J. Appl. Phys.*, 91:5016, 2002.

[65] A. Kadashchuk, Y. Skryshevskii, A. Vakhnin, N. Ostapenko, V. I. Arkhipov, E. V. Emelianova, and H. Bässler. Thermally stimulated photoluminescence in disordered organic materials. *Phys. Rev. B*, 63:115205, 2001.

[66] A. Kadashchuk, A. Vakhnin, Y. Skryshevski, V. I. Arkhipov, E. V. Emelianova, and H. Bässler. Thermally stimulated luminescence in π-conjugated polymers containing fluorene and spirobifluorene units. *Chemical Physics*, 291:243, 2003.

[67] A. Kadashchuk, D. S. Weiss, P. M. Borsenberger, S. Něspùrek, N. Ostapenko, and V. Zaika. The origin of thermally stimulated luminescence in neat and molecularly doped charge transport polymer systems. *Chemical Physics*, 247:307, 1999.

[68] K. Kawano and C. Adachi. Evaluating carrier accumulation in degraded bulk heterojunction organic solar cells by a thermally stimulated current technique. *Adv. Funct. Mater.*, 19:3934, 2009.

[69] R. Könenkamp, G. Priebe, and B. Pietzak. Carrier mobilities and influence of oxygen in C_{60} films. *Phys. Rev. B*, 60:11804, 1999.

[70] L. J. A. Koster, V. D. Mihailetchi, R. Ramaker, and P. W. M. Blom. Light intensity dependence of open-circuit voltage of polymer:fullerene solar cells. *Appl. Phys. Lett.*, 86:123509, 2005.

[71] L. J. A. Koster, E. C. P. Smits, V. D. Mihailetchi, and P. W. M. Blom. Device model for the operation of polymer/fullerene bulk heterojunction solar cells. *Phys. Rev. B*, 72:085205, 2005.

[72] D. V. Lang. Deep-level transient spectroscopy: A new method to characterize traps in semiconductors. *J. Appl. Phys.*, 45:3023, 1974.

[73] P. Langevin. Recombinaison et mobilites des ions dans les gaz. *Ann. Chim. Phys.*, 28:433, 1903.

[74] J. H. Lee, S. Cho, A. Roy, H.-T. Jung, and A. J. Heeger. Enhanced diode characteristics of organic solar cells using titanium suboxide electron transport layer. *Appl. Phys. Lett.*, 96:163303, 2010.

[75] J. K. Lee, W. L. Ma, C. J. Brabec, J. Yuen, J. S. Moon, J. Y. Kim, K. Lee, G. C. Bazan, and A. J. Heeger. Processing additives for improved efficiency from bulk heterojunction solar cells. *J. Am. Chem. Soc.*, 130:3619, 2008.

[76] M. Lenes, S. W. Shelton, A. B. Sieval, D. F. Kronholm, J. C. Hummelen, and P. W. Blom. Electron trapping in higher adduct fullerene-based solar cells. *Adv. Funct. Mater.*, 19:3002, 2009.

[77] M. Lenes, G.-J. A. H. Wetzelaer, F. B. Kooistra, S. C. Veenstra, J. C. Hummelen, and P. W. M. Blom. Fullerene bisaducts for enhanced open-circuit voltages and efficiencies in polymer solar cells. *Adv. Funct. Mater.*, 20:2116, 2008.

[78] A. C. Lewandowski and S. W. S. McKeever. Generalized description of thermally stimulated processes without the quasiequilibrium approximation. *Phys. Rev. B*, 43:8163, 1991.

[79] G. Li, V. Shortriya, Y. Yao, and Y. Yang. Investigation of annealing effects and film thickness dependence of polymer solar cells based on poly(3-hexylthiophene). *J. Appl. Phys.*, 98:043704, 2005.

[80] G. Li, V. Shrotriya, J. Huang, Y. Yao, T. Moriarty, K. Emery, and Y. Yang. High-efficiency solution processable polymer photovoltaic cells by self-organization of polymer blends. *Nature Mater.*, 4:864, 2005.

[81] H.-H. Liao, C.-M. Yang, C.-C. Liu, S.-F. Horng, H.-F. Meng, and J.-T. Shy. Dynamics and reversibility of oxygen doping and de-doping for conjugated polymer. *J. Appl. Phys.*, 103:104506, 2008.

[82] E. Lioudakis, A. Othons, I. Alexandrou, and Y. Hayashi. Optical properties of conjugated poly(3-hexylthiophene)/[6,6]-phenylC_{61}-butyric acid methyl ester composites. *J. Appl. Phys.*, 102:083104, 2007.

[83] C.-C. Liu, C.-M. Yang, W.-H. Liu, H.-H. Liao, S.-F. Horng, and H.-F. Meng. Interface effect of oxygen doping in polythiophene. *Synth. Met.*, 159:1131, 2009.

[84] C.-K. Lu and H.-F. Meng. Hole doping by molecular oxygen in organic semiconductors: Band-structure calculations. *Phys. Rev. B*, 75:235206, 2007.

[85] L. Lüer, H.-J. Egelhaaf, D. Oelkrug, G. Cerullo, G. Lanzani, B.-H. Huisman, and D. de Leeuw. Oxygen-induced quenching of photoexcited states in polythiophene films. *Organic Electronics*, 5:83, 2004.

[86] J. M. Marshall. Carrier diffusion in amorphous semiconductors. *Rep. Prog. Phys.*, 46:1235, 1983.

[87] S. J. Martin, D. D. C. Bradley, P. A. Lane, H. Mellor, and P. L. Burn. Linear and non-linear optical properties of the conjugated polymers PPV and MEH-PPV. *Phys. Rev. B*, 59:15133, 1999.

[88] T. Matsushima, M. Yahiro, and C. Adachi. Estimation of electron traps in carbon-60 field-effect transistors by a thermally stimulated current technique. *Appl. Phys. Lett.*, 91:103505, 2007.

[89] S. W. S. McKeever. On the analysis of complex thermoluminescence glow-curves: Resolution into individual peaks. *Phys. Stat. Sol. A*, 62:331, 1980.

[90] S. W. S. McKeever. *Thermoluminescence of solids*. Cambridge University Press, 1985.

[91] C. R. McNeill, J. J. M. Halls, R. Wilson, G. L. Whiting, S. Berkebile, M. G. Ramsey, R. H. Friend, and N. C. Greenham. Efficient polythiophene/polyfluorene copolymer bulk heterojunction photovoltaic devices: Device physics and annealing effects. *Adv. Funct. Mater.*, 18:2309, 2008.

[92] E. J. Meijer, C. Detcheverry, P. J. Baesjou, E. van Veenendaal, D. M. de Leeuw, and T. M. Klapwijk. Dopant density determination in disordered organic field-effect transistors. *J. Appl. Phys.*, 93:4831, 2003.

[93] V. D. Mihailetchi, L. J. A. Koster, J. C. Hummelen, and P. W. M. Blom. Photocurrent generation in polymer-fullerene bulk heterojunctions. *Phys. Rev. Lett.*, 93:216601, 2004.

[94] V. D. Mihailetchi, J. K. J. van Duren, P. W. M. Blom, J. C. Hummelen, R. A. J. Janssen, J. M. Kroon, M. T. Rispens, W. J. H. Verhees, and M. M. Wienk. Electron transport in a methanofullerene. *Adv. Funct. Mater.*, 13:43, 2003.

[95] V. D. Mihailetchi, J. Wildeman, and P. W. M. Blom. Space-charge limited photocurrent. *Phys. Rev. Lett.*, 94:126602, 2005.

[96] A. Miller and E. Abrahams. Impurity conduction at low concentrations. *Phys. Rev.*, 120:745, 1960.

[97] A. J. Mozer and N. S. Sariciftci. Negative electric field dependence of charge carrier drift mobility in conjugated, semiconducting polymers. *Chem. Phys. Lett.*, 389:438, 2004.

[98] D. Mühlbacher, M. Scharber, M. Morana, Z. Zhu, D. Waller, R. Gaudiana, and C. Brabec. High photovoltaic performance of a low-bandgap polymer. *Adv. Mater.*, 18:2884, 2006.

[99] J. Nelson, J. Kirkpatrick, and P. Ravirajan. Factors limiting the efficiency of molecular photovoltaic devices. *Phys. Rev. B*, 69:035337, 2004.

[100] H. Neugebauer, C. Brabec, J. C. Hummelen, and N. S. Sariciftci. Stability and photodegradation mechanisms of conjugated polymer/fullerene plastic solar cells. *Solar Energy Materials and Solar Cells*, 61:35, 2000.

[101] S. Neugebauer. *Langzeitstabile Materialien für die organische Photovoltaik: Untersuchung elektronischer Störstellen mittels transienter Störstellenspektroskopie*. Diploma thesis, Julius-Maximilians University of Würzburg, 2011.

[102] T. Nguyen, P. L. Rendu, O. Gaudin, A. Lee, R. Jackman, and C. Huang. Defect states investigation in poly(2-methoxy,5-(2'ethyl-hexyloxy)-1,4-phenylene vinylene) (MEH-PPV). *Thin Solid Films*, 511:338, 2006.

[103] K. H. Nicholas and J. Woods. The evaluation of electron trapping parameters from conductivity glow curves in cadmium sulphide. *Brit. J. Appl. Phys.*, 15:783, 1964.

[104] V. R. Nikitenko, H. Heil, and H. von Seggern. Space-charge limited current in regioregular poly-3-hexyl-thiophenerge. *J. Appl. Phys.*, 94:2480, 2003.

[105] V. R. Nikitenko, H. von Seggern, and H. Bässler. Non-equilibrium transport of charge carriers in disordered organic materials. *J. Phys.: Condens. Matter*, 19:136210, 2007.

[106] J. Noolandi. Equivalence of multiple-trapping and time-dependent random walk. *Phys. Rev. B*, 16:4474, 1977.

[107] J. Noolandi. Multiple-trapping model of anomalous transit-time dispersion in α -Se. *Phys. Rev. B*, 16:4466, 1977.

[108] K. Norrman, S. A. Gevorgyan, and F. C. Krebs. Water-induced degradation of polymer solar cells studied by $H_2{}^{18}O$ labeling. *Applied Materials and Interfaces*, 1:102, 2009.

[109] S. V. Novikov, D. H. Dunlap, V. M. Kenkre, P. E. Parris, and A. V. Vannikov. Essential role of correlations in governing charge transport in disordered organic materials. *Phys. Rev. Lett.*, 81:4472, 1998.

[110] H. Ohkita, S. Cook, Y. Astuti, W. Duffy, S. Tierney, W. Zhang, M. Heeney, I. McCulloch, J. Nelson, D. D. C. Bradley, and J. R. Durrant. Charge carrier formation in polythiophene/fullerene blend films studied by transient absorption spectroscopy. *J. Am. Chem. Soc.*, 130:3030, 2008.

[111] L. Onsager. Initial recombination of ions. *Phys. Rev.*, 54:554, 1938.

[112] F. Padinger, R. S. Rittberger, and N. S. Sariciftci. Effects of postproduction treatment on plastic solar cells. *Adv. Funct. Mater.*, 13:85, 2003.

[113] S. H. Park, A. Roy, S. Beaupré, S. Cho, N. Coates, J. S. Moon, D. Moses, M. Leclerc, K. Lee, and A. J. Heeger. Bulk heterojunction solar cells with internal quantum efficiency approaching 100 %. *Nature Photonics*, 3:297, 2009.

[114] J. Peet, J. Y. Kim, N. E. Coates, W. L. Ma, D. Moses, A. J. Heeger, and G. C. Bazan. Efficiency enhancement in low-bandgap polymer solar cells by processing with alkane dithiols. *Nature Mater.*, 6:497, 2007.

[115] M. Pope and C. E. Swenberg. *Electronic Processes in Organic Crystals and Polymers*. Oxford University Press, USA, 2nd edition, 1999.

[116] T. J. Prosa, M. J. Winokur, J. Moulton, P. Smith, and A. J. Heeger. X-ray structural studies of poly(3-alkylthiophenes): An example of an inverse comb. *Macromolecules*, 25:4364, 1992.

[117] J. T. Randall and M. H. F. Wilkins. Phosphorescence and electron traps. i.the study of trap distributions. *Proc. Roy. Soc. A*, 184:366, 1945.

[118] D. Rauh, A. Wagenpfahl, C. Deibel, and V. Dyakonov. Relation of open circuit voltage to charge carrier density in organic bulk heterojunction solar cells. *Appl. Phys. Lett.*, 98:133301, 2011.

[119] M. O. Reese, A. J. Morfa, M. S. White, N. Kopidakis, S. E. Shaheen, G. Rumbles, and D. S. Ginley. Pathways for the dagradation of organic photovoltaic P3HT:PCBM based devices. *Sol. Ener. Mat. Sol. Cells*, 92:746, 2008.

[120] G. Rudlof, J. Becher, and H. Glaefeke. Behaviour of the fractional glow technique with first-order detrapping processes, traps distributed in energy or frequency factor. *Phys. Stat. Sol. A*, 49:K121, 1978.

[121] N. S. Sariciftci, L. Smilowitz, A. J. Heeger, and F. Wudl. Photoinduced electron transfer from a conducting polymer to buckminsterfullerene. *Science*, 258:1474, 1992.

[122] T. J. Savenije, J. E. Kroeze, X. Yang, and J. Loos. The effect of thermal treatment on the morphology and charge carrier dynamics in a polythiophene-fullerene bulk heterojunction. *Adv. Funct. Mater.*, 15:1260, 2005.

[123] P. Schilinsky, C. Waldauf, and C. J. Brabec. Recombination and loss analysis in polythiophene based bulk heterojunction photodetectors. *Appl. Phys. Lett.*, 81:3885, 2002.

[124] R. Schmechel and H. von Seggern. Electronic traps in organic transport layers. *Phys. Stat. Sol. A*, 201:1215, 2004.

[125] A. Seemann, H.-J. Egelhaaf, C. J. Brabec, and J. A. Hauch. Influence of oxygen on semi-transparent organic solar cells with gas permeable electrodes. *Organic Electronics*, 10:1424, 2009.

[126] P. E. Shaw, A. Ruseckas, and I. D. W. Samuel. Exciton diffusion measurements in poly(3-hexylthiophene). *Adv. Mater.*, 20:3516, 2008.

[127] V. Shortriya, G. Li, Y. Yao, T. Moriarty, K. Emery, and Y. Yang. Accurate measurement and characterization of organic solar cells. *Adv. Funct. Mater.*, 16:2016, 2006.

[128] C. G. Shuttle, A. Maurano, R. Hamilton, B. O'Regan, J. C. de Mello, and J. R. Durrant. Charge extraction analysis of charge carrier densities in a polythiophene/fullerene solar cell: Analysis of the origin of the device dark current. *Appl. Phys. Lett.*, 93:183501, 2008.

[129] C. G. Shuttle, B. O'Regan, A. M. Ballantyne, J. Nelson, D. D. C. Bradley, J. de Mello, and J. R. Durrant. Experimental determination of the rate law for charge carrier decay in a polythiophene:fullerne solar cell. *Appl. Phys. Lett.*, 92:093311, 2008.

[130] T. B. Singh, N. Marjanovic, P. Stadler, M. Auinger, G. J. Matt, S. Günes, and N. S. Sariciftci. Fabrication and characterization of solution-processed methanofullerene-based organic field-effect transistors. *J. Appl. Phys.*, 97:083714, 2005.

[131] H. Sirringhaus, P. J. Brown, R. H. Friend, M. M. Nielsen, K. Bechgaard, B. M. W. Langeveld-Voss, A. J. H. Spiering, R. A. J. Janssen, E. W. Meijer, P. Herwig, and D. M. de Leeuw. Two-dimensional charge transport in self-organized, high-mobility conjugated polymers. *Nature*, 401:685, 1999.

[132] T. Strobel, C. Deibel, and V. Dyakonov. Role of polaron pair diffusion and surface losses in organic semiconductor devices. *Phys. Rev. Lett.*, 105:266602, 2010.

[133] T. Stübinger and W. Brütting. Exciton diffusion and optical interference in organic donor–acceptor photovoltaic cells. *J. Appl. Phys.*, 90:3632, 2001.

[134] J. Subbiah, D. Y. Kim, M. Hartel, and F. So. MoO_3/poly(9,9-dioctylfluorene-co-N-[4-(3-methylpropyl)]-diphenylamine) double-interlayer effect on polymer solar cells. *Appl. Phys. Lett.*, 96:063303, 2010.

[135] C. Tanase, E. J. Meijer, P. W. M. Blom, and D. M. de Leeuw. Unification of the hole transport in polymeric field-effect transistors and light-emitting diodes. *Phys. Rev. Lett.*, 91:216601, 2003.

[136] A. Tapponnier, I. Biaggio, and P. Günter. Ultrapure C_{60} field-effect transistors and the effects of oxygen exposure. *Appl. Phys. Lett.*, 86:112114, 2005.

[137] H.-E. Tseng, C.-Y. Liu, and S.-A. Chen. Determination of trap polarity in conjugated electroluminescent polymer by photoexcitation thermally stimulated current method. *Appl. Phys. Lett.*, 88:042112, 2006.

[138] S. M. Tuladhar, M. Sims, J. Kirkpatrick, R. C. Maher, A. J. Chatten, D. D. C. Bradley, and J. Nelson. Influence of alkyl chain length on charge transport in symmetrically substituted poly(2,5-dialkoxy-p-phenylenevinylene) polymers. *Phys. Rev. B*, 79:035201, 2009.

[139] P. Vanlaeke, A. Swinnen, I. Haeldermans, G. Vanhoyland, T. Aernouts, D. Cheyns, C. Deibel, J. D'Haen, P. Heremans, J. Poortmans, and J. V. Manca. P3HT/PCBM bulk heterojunction solar cells: Relation between morphology and electro-optical characteristics. *Sol. Ener. Mat. Sol. Cells*, 90:2150, 2006.

[140] D. Veldman, S. C. J. Meskers, and R. A. J. Janssen. The energy of charge-transfer states in electron donor–acceptor blends: Insight into the energy losses in organic solar cells. *Adv. Funct. Mater.*, 19:1939, 2009.

[141] N. von Malm. *Ladungsträgerfallen in amorphen organischen Halbleitern*. PhD thesis, Technische Universität Darmstadt, 2003.

[142] N. von Malm, J. Steiger, H. Heil, R. Schmechel, and H. von Seggern. Electronic traps and percolation paths in electroluminescent polymers. *J. Appl. Phys.*, 92:7564, 2002.

[143] A. Wagenpfahl, D. Rauh, M. Binder, C. Deibel, and V. Dyakonov. S-shape current-voltage characteristics of organic solar devices. *Phys. Rev. B*, 82:115306, 2010.

[144] C. Waldauf, M. Morana, P. Denk, P. Schilinsky, K. Coakley, S. A. Choulis, and C. J. Brabec. Highly efficient inverted organic photovoltaics using solution based titanium oxide as electron selective contact. *Appl. Phys. Lett.*, 89:233517, 2006.

[145] J. Weese. A reliable and fast method for the solution of Fredholm integral equations of the first kind on Tikhonov regularization. *Computer Physics Communications*, 69:99, 1992.

[146] J. Weese. A regularization method for nonlinear ill-posed problems. *Computer Physics Communications*, 77:429, 1993.

[147] M. M. Wienk, J. M. Kroon, W. J. H. Verhees, J. Knol, J. C. Hummelen, P. A. van Hal, and R. A. J. Janssen. Efficient methano[70]fullerne/MDMO-PPV bulk heterojunction photovoltaic cells. *Angew. Chem. Int. Ed.*, 42:3371, 2003.

[148] P. H. Wöbkenberg, D. D. C. Bradley, D. Kronholm, J. C. Hummelen, D. M. de Leeuw, M. Cölle, and T. D. Anthopoulos. High mobility n-channel organic field-effect transistors based on soluble C_{60} and C_{70} fullerene derivatives. *Synth. Met.*, 158:468, 2008.

[149] G. Yu, J. Gao, J. C. Hummelen, F. Wudl, and A. J. Heeger. Polymer photovoltaic cells: Enhanced efficiencies via a network of internal doner-acceptor heterojunctions. *Science*, 270:1789, 1995.

[150] A. Zaban, M. Greenshtein, and J. Bisquert. Determination of the electron life-time in nonocrystalline dye solar cells by open-circuit voltage decay measurements. *ChemPhysChem*, 4:859, 2003.

[151] Y. Zhou, J. Pei, Q. Dong, X. Sun, Y. Liu, and W. Tian. Donor–acceptor molecule as the acceptor for polymer-based bulk heterojunction solar cells. *J. Phys. Chem. C*, 113:7882, 2009.

A. List of Abbreviations

Abbreviation	Description
BHJ	bulk heterojunction solar cell
bis$PC_{61}BM$	bis[6,6]-phenyl C61 butyric acid methyl ester
C-DLTS	capacitance based deep level transient spectroscopy
CB	conduction band
CELIV	charge extraction by linearly increasing voltage
CDM	correlated disorder model
CTS	charge transfer state
DLTS	deep level transient spectroscopy
DOOS	density of occupied states
DOS	density of states
ETL	electron transport layer
GDM	Gaussian disorder model
HOMO	highest occupied molecular orbital
HTL	hole transport layer
ITO	indium tin oxide
IV	current–voltage
LED	light emitting diode
LUMO	lowest unoccupied molecular orbital
MDMO-PPV	poly(2-methoxy-5-(3',7'-dimethyloctyloxy)-1,4-phenylene-vinylene)
mpp	maximum power point
MTR	multiple trapping and release
OFET	organic field effect transistor
OLED	organic light emitting diode
OPV	organic photovoltaics
P3HT	poly(3-hexylthiophene)
$PC_{61}BM$	[6,6]-phenyl C61 butyric acid methyl ester
$PC_{71}BM$	[6,6]-phenyl C71 butyric acid methyl ester
PCE	power conversion efficiency
PEDOT:PSS	poly(3,4-ethylenedioxythiophene):(polystyrenesulfonate)

Abbreviation	Description
photo-CELIV	photo generated charge extraction by linearly increasing voltage
PPV	poly(p-phenylenevinylene)
Q-DLTS	current based deep level transient spectroscopy
TSC	thermally stimulated current
TSL	thermally stimulated luminescence
VB	valence band
VRH	variable range hopping

B. List of Symbols

Symbol	Description	Unit
A	active sample area	m^2
α	regularization parameter (Tikhonov regularization)	
b	heating rate	K/s
c	real constant (Laplace transform)	
C	scaling factor (GDM)	$m^{1/2}V^{-1/2}$
γ	inverse localization radius (Miller–Abrahams Equation)	m^{-1}
γ_L	Langevin recombination prefactor	m^3/s
d	sample thickness	m
e	emission rate from the traps (trap distribution)	s^{-1}
e_t	emission rate from the traps (monoenergetic trap)	s^{-1}
E	energy	eV
E_i	energy of initially occupied localized state	eV
E_j	energy of localized target state	eV
E_t	trap activation energy	eV
E_{tr}	transport energy	eV
ε_0	dielectric constant in free space	F/m
ε_r	relative dielectric constant	
$f(e)$	$dAqg(e)e$, emission rate distribution (DLTS)	m^3Cs^{-2}
F	electric field	V/m
FF	fill factor	
$g(e)$	emission rate distribution	s^{-1}
$g(E)$	Gaussian distribution of localized states	$m^{-3}\ eV^{-1}$
η	solar cell efficiency	
I	current	A
ΔI	Boxcar signal	A
I_{TSC}	thermally stimulated current	A
J_{sc}	short-circuit current	A
j_{sc}	short-circuit current density	A/m^2

Symbol	Description	Unit
k_B	Boltzmann constant	eV/K
k_d	polaron pair dissociation rate	s^{-1}
k_f	polaron pair recombination rate	s^{-1}
k_r	recombination rate of free charges to polaron pairs	s^{-1}
$K(t,e)$	Kernel (Tikhonov regularization)	
$M_\alpha[f(e)]$	Tikhonov regularization	
μ	mobility	m^2/Vs
μ_∞	mobility for $T \to \infty$ (GDM)	m^2/Vs
μ_e	electron mobility	m^2/Vs
μ_{GDM}	mobility according to GDM	m^2/Vs
μ_h	hole mobility	m^2/Vs
n	electron density	m^{-3}
n_c	electron density in the conduction band	m^{-3}
n_i	intrinsic charge carrier concentration	m^{-3}
n_t	density of trapped electrons / lower limit of trap density (TSC)	m^{-3}
n_{t0}	density of initially occupied traps	m^{-3}
N	density of localized states	m^{-3}
N_c	density of states in the conduction band	m^{-3}
N_t	trap density	m^{-3}
ν_0	attempt-to-escape frequency	s^{-1}
ν_{ij}	Miller–Abrahams hopping rate	s^{-1}
p	hole density	m^{-3}
P	polaron pair dissociation probability	
P_L	radiant power of incident light	W
P_{mpp}	maximum power of the solar cell	W
$\rho_0(E)$	density of initially occupied states	$m^{-3}\ eV^{-1}$
q	elementary charge	C
R	Langevin recombination rate	$m^{-3}s^{-1}$
R_{ij}	spatial distance between initial and target state	m
S	capture cross section of the traps	m^2
σ	width of Gaussian distribution	eV
Σ	spatial disorder factor (GDM)	
t	time	s
t_p	bias pulse width (CELIV)	s
T	temperature	K
T_0	temperature of trap filling	K
T_{max}	temperature of TSC maximum	K
T_{Start}	start temperature of the heating (fractional TSC)	K
T_{Stop}	stop temperature of the heating (fractional TSC)	K

Symbol	Description	Unit
τ	charge carrier lifetime / time constant of exponential decay (DLTS)	s
τ_{pp}	polaron pair lifetime	s
τ_{set}	Boxcar time window	s
v_d	drift velocity	m/s
v_{th}	thermal velocity of charge carriers	m/s
V	sample volume	m^3
V_a	peak voltage (CELIV)	V
V_{oc}	open-circuit voltage	V
V_{off}	offset bias (CELIV)	V
Φ_L	radiant power density of incident light	W/m^2
$\Omega[f(e)]$	regularization functional (Tikhonov regularization)	

Danksagung

Ich möchte mich herzlich bei Allen bedanken, die mich in den letzten Jahren während der Anfertigung dieser Arbeit begleitet und zum Gelingen dieser Arbeit beigetragen haben.

Mein erster Dank gebührt natürlich Prof. Dr. Vladimir Dyakonov, der mir die Anfertigung dieser Dissertation an seinem Lehrstuhl mit wirklich exzellenter Ausstattung ermöglich hat. Des Weiteren möchte ich mich bei ihm auch für die Diskussionen meiner Publikationen und das gekonnte Briefing vor Tagungen bedanken, sowie für die Ermöglichung der Teilnahme an nationalen und internationalen Konferenzen. Darüber hinaus hat er mich immer unterstütz und auch er war es, der mich für die Verleihung des ZONTA Preises vorgeschlagen hat.

Prof. Dr. Jean Geurts möchte ich herzlich für das positive Gutachten für meinen Stipendiumsantrag, sowie für die Begutachtung dieser Arbeit danken.

Mein ganz besonderer Dank gilt Dr. Carsten Deibel, dafür dass mir seine Bürotür stets für Diskussionen und Gespräche offen stand, obwohl ich bei Weitem nicht die einzige war, die seine Kompetenz gerne in Anspruch genommen hat. Ich danke ihm aber auch dafür, dass er mir viel Freiraum in meiner wissenschaftlichen Arbeit gewährt hat und mich dennoch stets wissen lies, dass ich mich bei Fragen und Problemen jederzeit an ihn wenden kann.

Diep Phan, unserer guten Seele, gebührt ein riesiger Blumenstrauß. Stets hilfsbereit und gut gelaunt, hilft sie jedem nicht nur bei dem Papierkram der ständig zu bewältigen ist. Ohne sie würden wir hier im Chaos versinken.

Natürlich hatte ich auch viele liebe Kollegen, die das Arbeiten hier sehr angenehm gemacht haben. Für die gute Atmosphäre gilt mein Dank der gesamten EP VI.

Für viele interessante Diskussionen—während der Gruppentreffen und auch dazwischen—möchte ich mich vor allem bei allen der Transport- und Solarzellengruppe angehörenden EP VIlern bedanken. Besonders sind hier Dipl.-Ing. Andreas Baumann und Dipl.-Phys. Alexander Wagenpfahl für die gute Zusammenarbeit hervorzuheben. Andreas ist der Mann der CELIV Messungen und Alex, unser "Simulant", hat mit seinen Simulationen entscheidenden Beitrag zu dem Verständnis des Kurzschlussstromverlusts beigetragen. Es war mir eine Freude mit euch zusammenzuarbeiten, auch wenn Alex seinen Simulationen gerne mehr Vertrauen schenkt als unseren Messungen :-)

Meiner Kollegin Dipl.-Ing. Maria Hammer danke ich für viele fachliche Diskussionen, weibliche Unterstützung und oberpfälzer Heimatgefühle im Frankenland.

Während meiner Promotion durfte ich auch zwei Diplomanden betreuen: Roland Marx und Stefan Neugebauer. Euch danke ich für die Unterstützung beim Aufbau des DLTS Setups und besonders Stefan für die Implementierung von FTIKREG. Ihr habt einen tollen Job gemacht.

Auf keinen Fall vergessen möchte ich unsere technischen Assistenten André Thiem-Riebe und Valentin Baianov. Danke André, dass du unsere Glovebox am Leben hältst. Ohne dich wären viele Messungen gar nicht durchführbar gewesen. Valentin, deine optischen Schemata sind großartig!

Dank verdienen auch Dipl.-Phys. Andreas Sperlich und Dipl.-Phys. Hannes Kraus, für

ihre Unterstützung bei Hard- und Softwareproblemen, sowie die Wartung unseres Austausch Servers. Dank euch musste ich mir nie Sorgen machen, dass mein Datenberg verloren geht.

Bedanken möchte ich mich auch bei den Chemikern aus Wuppertal, rund um Prof. Ullrich Scherf für eine gute Zusammenarbeit. Besonders bedanke ich mich bei Dr. Sybille Allard, Dipl.-Chem. Kristina Schottler und Dipl.-Chem. Ines Dumsch, für die interessanten Materialien die sie uns zur Verfügung gestellt haben und dafür, dass sie meinen chemischen Horizont deutlich erweitert haben.

Mein Dank gilt auch Dr. Rüdiger Berger und Anna Domanski vom MPIP Mainz für eine gute Zusammenarbeit und wunderschöne Querschnitts-TEM Messungen an unseren Solarzellen.

Des Weiteren bedanke ich mich herzlich bei der Universität Bayern e.V., sowie dem ZONTA Club Würzburg für ihre Unterstützung.

Von ganzem Herzen möchte ich meiner Familie danken: meinen Eltern Hannelore und Horst und meinen beiden Brüdern Michael und Stephan. Danke, dass ihr all die Zeit hinter mir gestanden seid und immer an mich geglaubt habt.

Zuletzt möchte ich mich bei Dipl.-Phys. Daniel Rauh bedanken. Auch wenn du nebenbei mein liebster Kollege bist, gehörst du doch an diese Stelle. Durch deine moralische Unterstützung, deine unendliche Geduld beim Zuhören, besonders wenn (mal wieder) etwas nicht geklappt hat, durch deinen Glauben an mich, dein Verständnis und deine Unterstützung, wenn ich Nachts an die Uni bin, hast du einen riesigen Teil zum Gelingen dieser Arbeit beigetragen. Danke, für die wirklich hilfreichen Diskussionen, das Korrekturlesen dieser Arbeit und dass du alles hinterfragst!

List of Publications

Refereed Articles

- J. Schafferhans, A. Baumann, C. Deibel and V. Dyakonov, *Trap distribution and the impact of oxygen-induced traps on the charge transport in poly(3-hexylthiophene)*, Applied Physics Letters, 93 (2008), 093303

- J. Schafferhans, A. Baumann, A. Wagenpfahl, C. Deibel and V. Dyakonov, *Oxygen doping of P3HT:PCBM blends: Influence on trap states, charge carrier mobility and solar cell performance*, Organic Electronics 11 (2010), 1693.

- J. Schafferhans, C. Deibel and V. Dyakonov, *Electronic Trap States in Methanofullerenes*, Advanced Energy Materials (2011), doi: 10.1002/aenm.201100175.

- A. Baumann, A. Förtig, J. Schafferhans, C. Deibel and V. Dyakonov, *Enhanced charge carrier lifetime in oxygen exposed bulk heterojunction solar cells*, submitted

Contributed Talks

- Deutschen Physikerinnentagung 2008, Münster: J. Schafferhans, A. Baumann, C. Deibel and V. Dyakonov, *Investigation of oxygen-induced defects on the charge transport in conjugated polymers*

- DPG Frühjahrstagung 2009, Dresden: J. Schafferhans, R. Marx, C. Deibel and V. Dyakonov, *The impact of oxygen on trap states in P3HT:PCBM blends*

- DPG Frühjahrstagung 2010, Regensburg: J. Schafferhans, S. Neugebauer, A. Baumann, A. Wagenpfahl, C. Deibel and V. Dyakonov, *Oxygen induced degradation of P3HT:PCBM solar cells*

- DPG Frühjahrstagung 2011, Dresden: J. Schafferhans, C. Deibel and V. Dyakonov, *Electronic trap states in methanofullerenes and their influence on organic solar cells*

Poster Presentations

- DPG Frühjahrstagung 2007, Regensburg: J. Schafferhans, C. Deibel and V. Dyakonov, *Investigation of electronic traps in organic transport layers via thermally stimulated current measurements*

- DPG Frühjahrstagung 2008, Berlin: J. Schafferhans, C. Deibel and V. Dyakonov, *Investigation of electronic traps in disordered organic semiconductors via thermally stimulated current measurements*

- E-MRS Spring Meeting 2008, Strasbourg: J. Schafferhans, A. Baumann, C. Deibel and V. Dyakonov, *Impact of oxygen-induced traps on the charge transport in conjugated polymers*

- MRS Fall Meeting 2009, Boston: J. Schafferhans, A. Baumann, A. Wagenpfahl, C. Deibel and V. Dyakonov, *The impact of oxygen on trap states in P3HT:PCBM solar cells*, Best Poster Award Nominee

Ehrenwörtliche Erklärung

gemäß § 5 Abs. 2 Ziff. 2 und 5
der Promotionsordnung der
Fakultät für Physik und Astronomie
der Julius-Maximilians-Universität Würzburg

Hiermit erkläre ich ehrenwörtlich, dass ich die Dissertation selbstständig und ohne Hilfe eines Promotionsberaters angefertigt und keine weiteren als die angegebenen Quellen und Hilfsmittel benutzt habe.

Die Dissertation wurde bisher weder vollständig noch teilweise einer anderen Hochschule mit dem Ziel einen akademischen Grad zu erwerben vorgelegt.

Am 22. November 2007 wurde mir von der Julius-Maximilians-Universität Würzburg der akademische Grad "Diplom-Physikerin Univ." verliehen. Weitere akademische Grade habe ich weder erworben noch versucht zu erwerben.

Die Dissertation wurde von Prof. Dr. Vladimir Dyakonov betreut.

Würzburg, den 31.03.2011

Julia Schafferhans